Removal of Organic Pollutants by Modified Zeolite/Clay Based Adsorbents/Photocatalysts

A thesis

submitted in fulfillment of the requirements for the degree of

Doctor of Philosophy

In

Chemistry

By

Aanchal

(Reg. No. 901709001)

Under the supervision of

Dr. Soumen Basu
Associate Professor
School of Chemistry and Biochemistry

Dr. Sanghamitra Barman
Associate Professor
Department of Chemical Engineering

School of Chemistry and Biochemistry

Thapar Institute of Engineering & Technology

(Deemed to be University)

Patiala, Punjab

INDIA

August, 2021

Dedicated

To

My Parents

Mr. Randhir Singh Rathi & Mrs. Bimla Devi

My Brother and Sisters

Mr. Abhinav Singh & Ms. Archna Rathi

My grandmother

Late Khajani Devi

CERTIFICATE

This is to certify that thesis entitled "**Removal of Organic Pollutants by Modified Zeolite/Clay Based Adsorbents/Photocatalysts**", being submitted by Ms. Aanchal in fulfillment of the requirement for the award of the Degree of Doctor of Philosophy in the School of Chemistry and Biochemistry, Thapar Institute of Engineering and Technology, Patiala, is a record of candidate's own independent and original research work carried out by her under my supervision and guidance. The matter presented in the thesis has not been submitted in part or full for the award of any degree in any other University or Institute.

(Supervisor)
Dr. Soumen Basu
Associate Professor
School of Chemistry and Biochemistry
Thapar Institute of Engineering and
Technology (Deemed to be University)
Patiala- 147004, Punjab (India)

(Supervisor)
Dr. Sanghamitra Barman
Associate Professor
Department of Chemical Engineering
Thapar Institute of Engineering and
Technology (Deemed to be University)
Patiala- 147004, Punjab (India)

(Head)
Dr. Susheel Mittal
Senior Professor
School of Chemistry and Biochemistry
Thapar Institute of Engineering and Technology
(Deemed to be University)
Patiala- 147004, Punjab (India)

CANDIDATE'S DECLARATION

I, hereby declare that the work presented in the thesis entitled "**Removal of Organic Pollutants by Modified Zeolite/Clay Based Adsorbents/Photocatalysts**", in fulfillment of the requirement for the award of the Degree of **Doctor of Philosophy**, School of Chemistry and Biochemistry, Thapar Institute of Engineering and Technology, Patiala, is an authentic record of my own work carried out under the supervisions of Dr. Soumen Basu, Associate Professor, School of Chemistry and Biochemistry, Thapar Institute of Engineering and Technology, Patiala, India and Dr. Sanghamitra Barman, Associate Professor, Department of Chemical Engineering, Thapar Institute of Engineering and Technology, Patiala, India. The matter embodied in this thesis has not been submitted in part or full to any other university or institute for the award of any degree in India or Abroad.

Aanchal

Aanchal

ACKNOWLEDGMENT

Through this section of the thesis, I would like to express my heartiest thankfulness to all those who encouraged and supported me in many ways for the accomplishment of this study and made it an unforgettable journey for me.

This work was carried out in the Advanced Nanomaterials Laboratory and Chemical Engineering Laboratory (Thapar Institute of Engineering and Technology) from 2017 to 2021. I would like to express my sincere thanks to my supervisors Dr. Soumen Basu, School of Chemistry and Biochemistry, Thapar Institute of Engineering and Technology, Patiala and Dr. Sanghamitra Barman, Department of Chemical Engineering, Thapar Institute of Engineering and Technology, Patiala for providing me a valuable research opportunity to work and countless guidance, knowledge, and motivation throughout my research. I learned a lot from them during my Ph.D. work. Their daily practice of following up on recent scientific literature is something that I also tried to adopt and greatly benefitted. I really appreciate their unconditional support and encouragement towards doing high-caliber research. It's been a great honor to work under their guidance.

I am extremely thankful to ***Prof. Prakash Gopalan****, Director, Thapar Institute of Engineering& Technology,* ***Prof. Rafat Siddique****, Dean of Research & Sponsored Projects, Thapar Institute of Engineering & Technology and to* ***Dr. Susheel Mittal****, Head of School of Chemistry and Biochemistry Thapar Institute of Engineering and Technology, Patiala. I would also like to express my special regards to the members of my doctoral committee, Dr. Bonamali Pal, Dr. Satnam Singh, Dr. Anoop Verma for their perceptive comments, advice, and scientific discussions. Special thanks to all the Teaching Faculty of the department for their cooperation and guidance. Also, special thanks to office staff Mr. Mayank Sharma and Mr. Chander Thakur, Mr. Hemant, Mr. Vishwanath, Mr. Shekhar and for their cooperation and timely support. I sincerely acknowledge Dr. Rafat Siddique Dean R & SP for finical support. The help from different laborites like SAI labs, CeNS Bengaluru, and Sprint Testing Solutions is highly acknowledged.*

different laborites like SAI labs, CeNS Bengaluru, and Sprint Testing Solutions is highly acknowledged.

I warmly thank all my friends and lab mates Ms. Neeraj Sohal, Dr. Shagun Kainth, Ms. Divya Monga, Ms. Shelly Singla, Ms. Aayushi Kundu, Ms. Aashna Nagar, Ms. Mansi Kapoor, Ms. Anushka, Mr. Ranjeet Kumar Jha, Mr. Zaid, Ms. Ridhima Sharma, Mr. Ashutosh, Ms. Geetika, Dr. Amit mishra and Mr. Parminder Singh for a great time and moral support. I would like to acknowledge my friend Ms. Surbhi Sharma for moral support and motivation every time, which drives me to give my best. I will forever cherish the warmth shown by them, whose smiling faces always inspired me. Special thanks to Sandeep, Chahat, Ripanshu, Yaddi, and Mandeep for guidance, support, and precious friendship.

The words are insufficient to convey my heartfelt gratitude to my father Mr. Randhir Singh Rathi and my mother Mrs. Bimla Devi for their encouragement and inspiration throughout my research work. I owe everything to them. My special thanks to my younger brother Mr. Abhinav Singh and my lovely sister Ms. Archna Rathi, my grandmother, and the whole Rathi family for unconditional love and support from childhood.

Besides this, I am thankful to the persons who knowingly and unknowingly helped me during the successful completion of this work.

Aanchal

Aanchal

TABLE OF CONTENT

Chapter-2
Literature review and zeolite framework

Chapter-3
Experimental methods, kinetics and isotherm models

Chapter-4
Adsorptive removal of fipronil by cerium modified zeolite ZSM-5: Equilibrium, kinetic and thermodynamic studies

Chapter-5

Photoactive porous g-C_3N_4/H-ZSM-5 nano-composite for endocrine disrupting compound and toxic dye degradation

Chapter-6

Adsorptive removal of fipronil by CeO_2 modified zeolites, and their structural properties

Chapter-7
C-dots@zeolite composite for antibiotic degradation and degraded products analysis

Chapter-8
Conclusions and future perspective

LIST OF FIGURES

Chapter-6

LIST OF SCHEMES

LIST OF TABLES

LIST OF SYMBOLS & ABBREVIATIONS

$\Delta G°$	Gibbs free energy (kJ/mol)
$\Delta S°$	entropy change (kJ/mol.K)
$\Delta H°$	enthalpy change (kJ/mol)
1/n	Adsorption intensity
k	Rate constant
B_T	Temkin constant
C_e	Equilibrium concentration of adsorbate in solution (mg/L)
C_f	Final concentration of adsorbate in liquid phase (mg/L)
C_i	Initial concentration of adsorbate in liquid phase (mg/L)
h	hour
k_1	Pseudo first order rate constant (min^{-1})
k_2	Pseudo second order rate constant (g/mg.min)
K_d	Equilibrium constant
K_F	Freundlich constant ($[(mg/g.(L/mg)]^{1/n}$)
k_I	Intra-particle diffusion constant ($mg/g.min^{0.5}$)
K_L	Langmuir constant (L/mg)
K_T	Maximum binding energy (L/mg)
R_L	Separation factor
q_e	Adsorption capacity (mg/g)
q_t	Adsorption capacity at time t (mg/g)
Q_m	Maximum adsorption capacity (mg/g)
Q_R	Maximum multilayer adsorption capacity (mg/g)
Q_s	Theoretical saturation capacity (mg/g)
E	Mean adsorption energy
K_d	Distribution coefficient
R	Universal gas constant (J/mol.K)
R^2	Correlation coefficient
ε	Polanyi Potential
w/v%	Weight/volume%
β	Maximum bond energy

µM	Micro-molar
nm	nanometer
µg/L	Micro-gram per litre
mg/ml	Milligram per millilitre
mg/L	Milligram per litre
ng/L	Nanogram per litre
µl	Microlitre
ml	Mllitre
eV	Electron volts
g	Gram
λ	Wavelength
°	Degree
%	Percentage
µm	Micrometer
ppm	Parts per million
mV	Millivolts

XRD	X-ray diffraction analysis
UV-vis	Ultraviolet-visible
SEM	Scanning electron microscopy
BET	Brunauer–Emmett–Teller
BJH	Barrett–Joyner–Halenda
HRTEM	High-Resolution Transmission electron microscopy
EDX	Energy-dispersive X-ray spectroscopy
XPS	X-ray photoelectron spectroscopy
GC–MS	Gas Chromatography Mass Spectrometry
C-dots	carbon dots
PL	Photoluminescence
EDC	Endocrine disrupting compounds
PPCPs	pharmaceuticals and personal care products
FIP	Fipronil
MB	Methylene blue
MET	Metronidazole
RhB	Rhodamine B
D-R	Dubbin-Radushkevich
B.E.	Binding energy
ppm	Parts per million
ZSM-5	Zeolite socony Mobil-5
MOR	Mordenite
BETA	Beta
USEPA	United States Environmental Protection Agency
AOPs	Advanced oxidation processes
MF	Microfiltration
UF	Ultrafiltration
NF	Nanofiltration
RO	Reverse osmosis

LIST OF PUBLICATIONS

In Peer-Reviewed (SCI) Journals

I. **A. Rathi**, S. Basu, S. Barman, Adsorptive removal of fipronil from its aqueous solution by modified zeolite HZSM-5: equilibrium, kinetic and thermodynamic study. *Journal of Molecular Liquids*, *283*, 2019, 867-878. (IF=6.165)

II. **Aanchal**, S. Barman, S. Basu, Complete removal of the endocrine-disrupting compound and toxic dye by visible light active porous g-C_3N_4/H-ZSM-5 nanocomposite. *Chemosphere*, *241*, 2020, 124981. (IF=7.086)

III. **A. Rathi**, S. Basu, S. Barman, Structural Framework Effect of Various CeO_2-loaded Zeolites on the Adsorptive Removal of Fipronil. *Journal of Environmental Chemical Engineering* (2021), 105167. (IF=5.909)

IV. **A. Rathi**, S. Basu, S. Barman, Antibiotic and dye eradication by one step synthesized C-dots@zeolite photocatalyst: performance evaluation, and degraded products analysis. (communicated)

V. **A. Rathi**, S. Basu, S. Barman, R. K. Arya, Post-fabrication structural changes and enhanced photodegradation activity of semiconductors@zeolite composites towards noxious contaminants. *Chemosphere*, 2021, 132609. (IF=7.086)

VI. J. Singh, S. Sharma, **Aanchal**, S. Basu, Synthesis of Fe_2O_3/TiO_2 monoliths for the enhanced degradation of industrial dye and pesticide via photo-Fenton catalysis, *Journal of Photochemistry and Photobiology A: Chemistry*, 376, 2019, 32-42. (IF=4.291)

VII. T. Mehta, **A. Rathi**, A. Verma, S. Barman, G. Halder, Elimination of Fipronil insecticide by adsorption technique from aqueous solution by Cu-13X zeolite composite: isotherms, kinetic and thermodynamic studies. *International Journal of Environmental Analytical Chemistry*, 2020, 1-17. (IF=2.826)

VIII. L. Dashairya[§], S. Sharma[§], **A. Rathi**[§], P. Saha, S. Basu, Solar-light-driven photocatalysis by Sb_2S_3/carbon based composites towards degradation of noxious organic pollutants, *Materials Chemistry and Physics*, (Impact Factor: 4.094)
([§] - *equal contribution*)

Book chapter

I. G. S. Sarkar, **A. Rathi**, S. Basu, R. K. Arya, G. Halder, S. Barman, Removal of endocrine-disrupting compounds by wastewater treatment. In "Advanced Industrial Wastewater Treatment and Reclamation of Water", (Springer Nature). ISBN: 978-3-030-83811-9.

Conferences/Workshops attended

i. Poster presentation on the topic "**Adsorption of Fipronil (Endocrine Disrupting Chemical) over modified H-ZSM5 zeolite: Equilibrium, kinetic and Thermodynamic study**" at International conference, CHEMCON – 2018 held at NIT, Jalandhar from December 27-30, 2018.

ii. Presented poster at a national conference, RTCES-2019 on the topic "**Efficient Photocatalytic Degradation of Toxic Dye by Visible Light Active Porous g-C_3N_4/H-ZSM-5 Composite**" held at Punjabi University, Patiala on February 07-08, 2019.

iii. Powerpoint presentation on the topic "**Elimination of phenylpyrazole insecticide by cerium modified zeolites via adsorption process: Equilibrium and kinetic analysis**" in **ACS SPRING-2021, (MACROMOLECULAR CHEMISTRY: THE SECOND CENTURY)** held virtually from April 05-16, 2021.

iv. International virtual conference conducted by U-SERC on the topic, "**Modern Instrumental and Characterization Techniques in Applied Sciences-2020**" (MICTAS-2020), attended at online mode on 5-6 July 2020.

v. National virtual conference conducted by U-SERC on the topic, "**Recent Advances in Analytical Techniques-2020**" (RAAT-2020), attended at online mode on 16-17 August 2020.

vi. Attended the **DST & ACS VIRTUAL WORKSHOP** on **"MASTERING THE PUBLISHING PROCESS"** JULY 28, 2020.

vii. Attended online national workshop on, **RECENT TRENDS IN INSTRUMENTAL TECHNIQUES OF CHEMICAL ANALYSIS**, organized by Department of Chemistry, Government Shyam Sundar Agrawal PG College, Sihora, Jabalpur (M.P.) attended at online mode on 8-13 February 2021.

viii. Attended e-conference on "**Materials of the Future: Smart Applications in Science and Engineering**" organized by Qatar university from 29-31 March 2021.

ix. Attended online national workshop on, **RECENT TRENDS IN INSTRUMENTAL TECHNIQUES OF CHEMICAL ANALYSIS**, organized by Department of Chemistry, Government Shyam Sundar Agrawal PG College, Sihora, Jabalpur (M.P.) attended at online mode on 8-13 February, 2021.

Webinars attended

i. International Webinar on **RECENT ADVANCES IN SCIENCE AND TECHNOLOGY,** organized by Maharani Kishori Jat Kanya Mahavidyalaya, Rohtak, attended online on 18-19 February, 2021.

ii. National Webinar series on **Practicing Chemdraw, Origin and Mendeley Tools in Research** (attended from 08th -10st August 2020), organized by Department of Chemistry, Laxman Singh Mahar Government Post Graduate College, Pithoragarh (A Constituent Unit of Kumaun University, Nainital).

iii. International Webinar on **RECENT ADVANCES IN SCIENCE AND TECHNOLOGY,** organized by Maharani Kishori Jat Kanya Mahavidyalaya, Rohtak, attended online on 18-19 February, 2021.

iv. National level technical meet on Micro and Nano Fabrication and characterization Techniques, actively participated on 9, November 2020; organized by Department of Physics (SF), Kamraj College, Thoothukudi-628003, Tamil Nadu.

ABSTRACT

The thesis entitled "**Removal of Organic Pollutants by Modified Zeolite/Clay Based Adsorbents/Photocatalysts"** is divided into eight chapters.

Chapter 1: This chapter portrays the introduction of noxious organic pollutants and their removal techniques. The impact of organic pollutants on living beings was elaborated. The effect of toxic organic pollutants on human beings and the environment was discussed along with their sources, health effects, and their removal methods. The noxious organic pollutants such as methylene blue (MB), fipronil (FIP), rhodamine B dye (RhB), and metronidazole (MET) were briefly introduced along with their structures and harmful effects. The different types of removal techniques for treating wastewater were compared to know the best technique. The adsorption and photodegradation processes for EDCs, dyes, or other pollutants were summarized.

Chapter 2: It deals with the literature survey of the different noxious contaminants (EDCs, pharmaceuticals, or dyes) which were removed by zeolite-based composites with adsorption or photocatalysis techniques. The % removal of various zeolites has been compared with other noxious contaminants. The pros and cons of various materials such as carbonaceous materials, metal-organic frameworks, zeolites, carbon nanotubes, adsorbents, activated carbon materials were briefly discussed. The structural properties of zeolite frameworks along with their significance in adsorption and photocatalytic degradation were explored. The properties of photoactive materials were also discussed. In comparison to other support materials zeolites were found to be an appropriate substance for the hybrid adsorption and photocatalysis process, because it has a huge surface area for adsorption, tunable surface properties, porosity, ion-exchange capability, and the abundance of acidic-basic sites which can be able to decrease the chances of electron/hole pairs recombination.

Chapter 3: In this chapter, the chemicals used for the synthesis and modification of zeolite framework were discussed, along with the characterization methods of prepared composites. The various characterization like N_2 adsorption-desorption analysis, X-ray diffraction analysis (XRD), Scanning electron microscopy (SEM), High-Resolution Transmission electron microscopy (HRTEM), Energy-dispersive X-ray spectroscopy analysis (EDX), X-ray photoelectron spectroscopy (XPS) were performed to evaluate the structural properties of the material in detail. The procedure for adsorption or photocatalytic degradation processes

and formulas adopted to calculate the adsorption capacities, rate constants, and other parameters were elaborated. The experimental data of adsorption were further verified with adsorption isotherms. The adsorption mechanism describing adsorbate and adsorbent interactions was evaluated by fitting the data in the Langmuir, Freundlich, Harkins-Jura, Dubbin-Radushkevich (D-R), and Halsey adsorption isotherm models. Different kinetic models such as Pseudo-first order, Pseudo-second order, Elovich model, and intra-particle diffusion were also investigated. Based on R^2 (Pearson correlation coefficient) values their accuracies were estimated. A thermodynamic study was carried out to know the enthalpy, entropy, and heat of the reaction.

Chapter 4: It covers the adsorptive removal of FIP, an endocrine disrupter insecticide from its aqueous solution by cerium-modified ZSM-5 zeolite adsorbent. A series of cerium modified H-ZSM-5 zeolite adsorbents such as Ce_5ZSM-5, Ce_{10}ZSM-5, Ce_{15}ZSM-5, Ce_{20}ZSM-5, Ce_{25}ZSM-5, and Ce_{30}ZSM-5 were prepared from the cerium salt of concentration (w/v%) 5%, 10%, 15%, 20%, 25%, and 30% respectively by simple refluxing treatment. The adsorptive performance of all of these prepared adsorbents was compared and Ce_{25}ZSM-5 was found to be the best adsorbent for FIP removal and characterized with XRD, N_2-adsorption, HRTEM, FESEM, EDS, and XPS techniques to study the porosity, crystallinity, and surface properties in detail. The batch adsorption experiments were performed to know the maximum adsorption capacity and % removal and found to be 598.80 mg/g and ~93% at optimum conditions (t: 120 min, pH 3, temperature: 25 °C, dose: 3.5 g/L, speed: 250 rpm, pollutant conc.: 600 mg/L). There was monolayer adsorption as the data fitted well in the Langmuir adsorption isotherm model and in kinetics, the pseudo-second-order model was followed with a high rate constant. The thermodynamic studies were carried out and $\Delta G°$, $\Delta H°$, and $\Delta S°$ parameters were calculated which confirms that the adsorption process is feasible, spontaneous, and exothermic.

Chapter 5: It deals with the metal-free catalyst g-C_3N_4 which is a visible light active material with a bandgap value of 2.7 eV. It can act as an efficient photocatalyst but its less surface area may hinder the photocatalysis process, therefore zeolite material with a huge surface area has been used to build an effective photocatalyst. The synthesized g-C_3N_4/H-ZSM-5 nanocomposite has sufficient surface area (~172 m^2/g) for the adsorption of pollutants with effective photodegradation activity. The composite was synthesized by mixing followed by facile calcination at 550 °C and properties of synthesized photocatalyst were explored with, BET, HRTEM, FESEM, EDS, and XPS characterization techniques. The photoactivity

of as-prepared g-C_3N_4/H-ZSM-5 nanocomposite was tested against the model MB dye and FIP insecticide. From the scavengers study $^{\bullet}OH$ and $O_2^{\bullet-}$ were found to be the responsible species for MB and FIP degradation. The maximum %degradation calculated were ~93% and ~89% for MB and FIP photocatalytic degradation. From these results, it has been discovered that this visible light-active photocatalyst is an effective composite for the degradation of harmful pollutants, and it's also easy to prepare.

Chapter 6: The adsorptive performance of cerium-modified different categories of zeolites was compared for the removal of FIP from its aqueous solution. The Ce-BETA, Ce-Mordenite, and Ce-13X adsorbents were prepared by a simple ion exchange method. The as-prepared different zeolites were characterized by XRD, BET, SEM, and EDS analysis for crystallinity, surface properties, and elemental compositions. The average crystallite size 'D' of cerium oxide is 6.67 nm for Ce-beta zeolite and 6.42 nm for Ce-Mordenite and 4.48 nm for Ce-13X zeolite, calculated with the Debye-Scherrer formula. The XPS data suggests that the cerium is present in two oxidation states i.e. Ce(IV) and Ce(III) with % amount of 71.10% and 28.29%, respectively, indicating that the Ce(IV) is more prominently. The d-spacing of cerium oxide was calculated from HRTEM analysis and their corresponding planes were matched with XRD following the JCPDS No. 34-0394. The various parameters of adsorption were investigated for FIP removal like pollutant concentration, adsorbent dose, pH, contact time, stirring speed, and temperature. The equilibrium data were fitted in various adsorption isotherms to know the type of adsorption. The best-fitted kinetic model signifies a higher adsorption rate. Thermodynamic parameters of adsorption revealed the spontaneous and exothermic adsorption processes. The structural comparison was also made between the 13X, Mordenite, and Beta zeolite frameworks.

Chapter 7: It deals with MET, a recalcitrant antibiotic from the nitro-imidazole family which contributes majorly to water pollution. The one-pot synthesis of Cdots@zeolite (CDZ) nano-composite by a hydrothermal treatment was carried out to photo-degrade MET molecules. The different ratios of CDZ composites (1:1, 1:3, 1:5, 5:1, and 1:7) were prepared by mentioned method and characterized by XRD, BET, EDS, and XPS for their crystallinity, surface area, elemental compositions, and surface chemical states respectively which confirms crystalline nature, incorporation of Cdots into zeolite frameworks with sufficient surface area. The morphology was analyzed by SEM analysis, d-spacing along with planes were characterized by HR-TEM and SAED analysis. The PZC (point of zero charges) value for the CDZ composite was determined to be at pH, 3.4. The maximum photocatalytic

degradation of ~79% was achieved at an optimum dose of 0.2 g/L and pH 4 for MET and that of RhB was ~90% at a catalyst dose of 0.4 g/L. The comparison of sunlight, Visible, and UV sources was performed with rate constants 'k' 0.0081, 0.0041, and 0.0101 min^{-1}respectively. The scavengers experiment was carried and found that electrons were the responsible active species for degradation of MET pollutant. The plausible photocatalytic degradation mechanism was explored and the intermediates or degradation pathway was drawn with the help of the m/z value obtained from GC-MS analysis.

Chapter 8: This chapter presents the conclusions and the future perspective of the present work. In the end, the references cited in the thesis have been listed. The modification of zeolite with cerium oxide was done with refluxing by ion exchange method. The increased cerium content in zeolite increases the active sites in zeolite which favours adsorption process. The Ce_{25}ZSM-5 adsorbent was found to have maximum removal because after that the saturation of active sites of zeolite occurs and the % removal remains almost constant. The cerium modified beta zeolite was found to possess maximum % removal of ~94% due to its huge surface area, porosity, and high Si/Al ratio. The efficient photocatalysts g-C_3N_4/H-ZSM-5 and Cdots@zeolite nano-composites were also prepared to degrade MB/FIP and MET/RhB pollutants effectively. The GC-MS analysis for MET was also carried out to determine the intermediates during the photocatalysis process.

Chapter 1: Introduction

1.1 Introduction

All over the world industrialization has been increased with such intensity that it causes severe environmental pollution. The toxic organic contaminants of wastewater are very harmful which deteriorate the earth's environment and natural resources. Emerging contaminants such as pharmaceuticals, industrial dyes, insecticides, cosmetics, and hygiene products are comprised of mainly organic moieties which have fascinated much interest of the researchers due to their huge usage and abolition into the environment.[1–3] The huge consumption of these noxious compounds results in an environmental crash all over the world due to their toxicity and persistence in the atmosphere.[4,5] It has been reported that insecticides have been widely used for pest control of vegetables, paddy fields, cereals, fruits, etc.[6] Nearly 60-98% of applied insecticides are retained in the topsoil or air dust which further gets adhered to the water resources making it contaminated.[6] The majorly used insecticides and pesticides such as fipronil, chlorpyrifos, DDT, thiamethoxam, and endosulfan come under the broad category of endocrine disrupting compounds (EDCs).[7–9] On the other hand, dyes are colored compounds that have huge usage in textile industries, UV protective clothes, as pH indicators, dye-sensitized solar cells, paper, cosmetics, leather, and food industries.[10] In 2015 a report suggested that above 20% of the reported level of polluted water was caused by these textile industrial wastes especially in Turkey, Indonesia, and China countries.[11] Such levels of these colored dye compounds not only harm the living beings but also deteriorating the quality of the water bodies. The pharmaceutical contaminants also causes water contamination as the use of antibiotics and other drugs has increased drastically.[12–14] So, there is a need to treat this polluted water with appropriate removal techniques. Therefore, an efficient and economically feasible treatment is needed to remove the micro-pollutants from water bodies in order to make an eco-friendly environment, so that the discharged effluent should not affect our natural resources, biosphere and human health. Different noxious organic contaminants which have been thoroughly studied for appropriate removal are elaborated in this chapter.

1.1.1 Organic pollutants

1.1.1.1 Endocrine disrupting compounds

EDCs harm human health by directly affecting the function of the endocrine system and became the core substance in environmental chemistry issues because of their presence in the environment. They are anthropogenic chemicals that cause disturbance and negative effects on the endocrine system to make an unwanted response and are also capable to hinder the hormonal system, which ultimately affects human and wildlife health.[15] The endocrine system includes a group of glands that secrete hormones and regulates the body functions of humans. Emerging contaminants such as micro-pollutants include wide and increasing numbers of anthropogenic and natural substances. These are mainly found in trace amounts, ranging from ng/L to μg/L in water, and can vary from pollutant to pollutant. The main effect of EDCs is either mimicking or hindering the functions of hormones like testosterone, estrogens, or thyroid. On the aspect of endocrine disruption, these are androgenic, estrogenic, and thyroidal substances.[16–18] EDCs are broadly classified into industrial chemical effluents, hormones (synthetic or natural steroids), pharmaceuticals and personal care products (PPCPs), surfactants, side products after combustion, and pesticides,[19,20] etc. Pharmaceuticals and Personal Care Products (PPCPs) include another group of EDCs that is also harming the ecological environment. In addition to other EDCs, they are comparatively well defined as they are found everywhere especially in wastewater discharge. The EDCs have one aromatic ring in their structure, which implies the hydrophobic property of micro-pollutants in a restricted and normal environment.

The United States Environmental Protection Agency (USEPA) described EDCs as the externally originated compounds or substances which perturbed the normal functioning of the natural hormones (like secretion, synthesis, transportation, elimination) present in the body.[21] The abnormal functioning of hormones is due to the blockage of hormone receptors by the similar structured EDCs which rooted severe problems such as (i) interruption in homeostasis process, (ii) reduction of sperm count and increasing chances of breast/prostate cancer, endometriosis,[22] (iii) create birth defects and developmental disorders,[7] (iv) egg rupturing of birds, fishes, and turtles get reduced, (v) converting male fishes feminized, (vi) disruption in the immunological system of mammals, reptiles and birds.[23,24]

1.1.1.1.1 Fipronil (FIP)

FIP is a broad-spectrum insecticide that comes under the phenylpyrazole family. It is not explosive, non-flammable, and doesn't oxidize very easily.[25] FIP is an efficient pest controller due to its efficacy at lower field application rates towards the pests which became resistant to the carbamates, pyrethroids, and organophosphate insecticides. Therefore its presence can be expected in the environment due to its properties and wide applications. FIP is also extensively used in preserving woods, sanitization, veterinary purposes, and also as a termite controller.[5,26] It can actively affect the CNS (Central nervous system) of pests by chloride channels which are under the control of GABA (gamma-aminobutyric acid) receptors. The LD50 (lethal dose, 50%) value is less than 0.5 µg/L and such a small concentration is enough to affect the invertebrates of aquatic water.[1,5] FIP has been identified in various water bodies of Florida such as man-made ponds, lakes, canals with concentration values in the range of 0.54 to 207.3 ng/L,[26] while in California its range was 11-280 ng/L for surface water of urban areas.[27] FIP has been found with an average concentration in the range of 0.026-0.737 µg/L and a higher concentration between 0.058-3.45 µg/L.[28] Therefore, it is crucial to examine the elimination techniques for the removal of such kinds of insecticides from the water bodies. The structure of fipronil is depicted in **Figure 1.1.**

1.1.1.2 Dyes

Dyes are colored organic compounds having a toxic effect on living beings and are extensively used in food, paper, leather, and textile industries. These textile industries enhance pollution by draining these harmful dyes in the natural water bodies. By deteriorating the water quality it creates an impact on the environment and human beings.[29] The inappropriate discard of the industrial effluent can induce cancer and mutations in living organisms. So, necessary steps should be taken for treating these noxious organic compounds to eliminate or completely mineralize CO_2 and H_2O.

1.1.1.2.1 Methylene blue (MB)

MB is a thiazine dye, intensely colored, cationic, and widely used in dyeing, printing, and silk colors.[30] It causes a neurotoxic effect on CNS (central nervous system) which could be detrimental, and long exposure to these can cause anemia, hypertension, and nausea. MB can't

be easily degraded via traditional wastewater treatment plants because of its complex ring structure, water-loving character, and huge stability towards chemicals, temperature, etc.[31] Therefore, it must be effectively degraded by an appropriate technique to avoid environmental pollution.

1.1.1.2.2 Rhodamine B (RhB)

RhB dye belongs to the triphenylmethane family, having 4 *N*-ethyl groups at the sides of the xanthene cyclic structure as shown in **Figure 1.1**. This industrial dye is well known for its stability and wide applicability in the textile industries for coloring cotton, silk wool, and jute leather.[32–34] It causes harmful effects on aquatic life when discarded directly into the environmental resources. This discharge also affects human beings and wildlife animals by producing carcinogenic and mutagenic activities in the living bodies.[32,35]

1.1.1.3 Pharmaceutical compound

1.1.1.3.1 Metronidazole drug (MET)

MET is a drug molecule that has antibiotic properties and is used for treating a variety of infections like abdominal, parasitic or anaerobic, etc. It is a white or creamy white colored crystalline powdery compound having a slight odour and salty taste.[36] It has a high solubility in water. It is non-biodegradable in nature and available in trace amounts in surface and groundwater. It is a kind of EDCs and its concentration varied from 1-10 ng/L in the water media.[12,37] MET accumulation in water bodies causes severe effects in mammals (like mutagenicity and carcinogenicity) and also to the water resources by food cycle and accumulation in the aquatic environment.[12,38] The literature survey of the above-mentioned and other EDCs has been compared and discussed in **Chapter 2**. The chemical structures of treated noxious contaminants are shown (MB, FIP, MET, and RhB) in **Figure 1.1**.

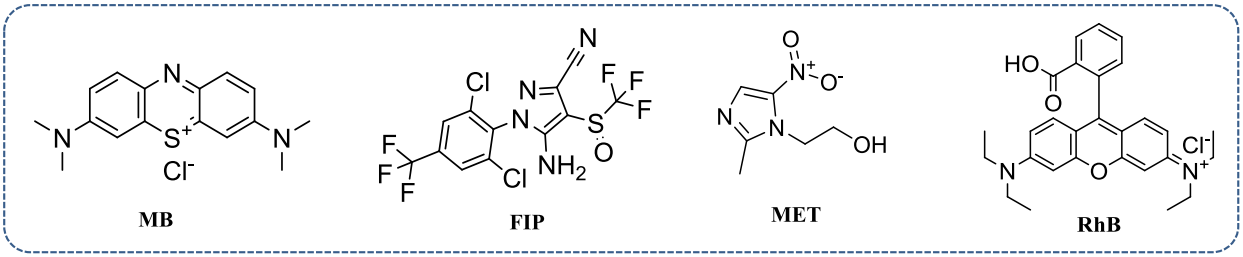

Figure 1.1: The chemical structures of MB, FIP, MET, and RhB pollutants.

These organic pollutants cause many serious effects on living organisms which can be fatal if not treated properly and on time. Some of the hazardous effects are tabulated below in **Table 1.1**.

Table 1.1: Hazardous effects of organic pollutants.

Organic pollutants	Harmful effects
MB	Consumption causes dizziness, mental delusion in the CNS, high blood pressure, fever, skin irritation, precordial pain in the heart, fecal discoloration, anemia in blood, and can also damage eyes if comes in direct contact[39]
RhB	Carcinogenic, mutagenic, eye and skin irritant, nausea, itchiness, nasal burning, gastrointestinal disorders, neuro, and reproductive toxicity[40]
FIP	Neurotoxic, sweating, headache, vomiting, weakness, cough, drowsiness, conjunctivitis, oropharyngeal pain, abdominal pain, gastrointestinal, dermal, and respiratory disorders[25,41,42]
MET	Mutagenic, carcinogenic, and genetic toxicity effects[43]

1.1.2 Approaches implied for water remediation

The noxious contaminants cause a serious threat to the ecosystem, especially to the air sources and water bodies. The destructive nature of the pollutants attracts the researcher's attention to overcome their extensive effects on the world.[44] So far many methods have been utilized for treating the wastewater like coagulation-flocculation, electrocoagulation, membrane filtration, ozonation, sedimentation, advanced oxidation processes (AOPs), photodegradation, chemical oxidation, chlorination, and adsorption.[5,34,45–47] Some of these methods like membrane filtration, coagulation-flocculation, and sedimentation were not able to give more than 25% efficiency; and persistence of these noxious contaminants into the water resources can cause danger to living beings. The electrocoagulation process involves the removal of contaminants by flowing current from the water and electrolytic oxidation at the anode. The amorphous immiscible metal oxides and hydroxides were formed that promote the adsorption of pollutants followed by precipitation and eases separation. The electrodes of Al and ferric salts were used because of their cost-effectiveness and efficiency for a variety of pollutants.[48] On the other hand, the chemical coagulation involves polymers and Al salts treatment for the wastewater, and PACl

flocculant (PACl: Polyaluminium Chloride) was utilized for the coagulation of finer particles into aggregated flocs that promotes the separation process by filtration or sedimentation techniques.[49]

The membrane separation process was also applied to eliminate the pollutants in wastewater treatment. According to the literature, the membrane separation technique includes electrostatic attractions, adsorption over the membranes, and steric hindrances whereas these mechanisms were varied for different types of membrane separations like microfiltration (MF), ultrafiltration (UF), nanofiltration (NF), and reverse osmosis (RO). The effectiveness of these techniques for the removal of pollutants was dependant on the membrane type, morphology, structures of pores, maintenance of concentration and electric potential, operational parameters, or physicochemical characteristics of noxious contaminants.[50,51] The different mechanisms are illustrated below and depicted in **Figure1.2**.

The MF and UF processes generally take place at low pressure (5-10 bar) and the pore size of the membranes varies from 0.025-5µm and 1-100 nm respectively. However, the filtration is not sufficient and requires further cleaning, relatively large solid particles were filtered through MF membranes. For NF (pore size: 0.5-10 nm) and RO (pore size <1 nm) working high pressures of 10-50 bar and 35-170 bar respectively, were required.[50,52,53] While ozonation and chlorination also have some drawbacks like ozonation can lead to the formation of some residual intermediates. The filtration technique can eliminate the suspended particles from the wastewater by crossing them through the filtration membrane/granular media. However, the cleansing of these membranes is relatively costly.[54,55] The other processes like coagulation and flocculation are generally executed by the use of potash alum, lime, iron salts, or polymers. These chemicals can bind or precipitate the contaminants and form colloids, which are consequently settled in the treatment reactor. This settling leads to the formation of sludge that is a solid waste that constitutes noxious contaminants. The membrane filtrations have a limitation of fouling of membranes which requires huge maintenance costs.[51] While the chemical oxidation process is not an eco-friendly technique as it includes the storage or transportation of harmful chemical compounds. The use of expensive and hazardous chemicals, coagulants, membranes, inadequacy to eliminate dissolved organic contaminants, and formation of secondary hazardous species are the main limitations of the wastewater treatment methods.[56–58] Therefore, some

reliable methods should be considered for water remediation such as adsorption and photocatalytic degradation.

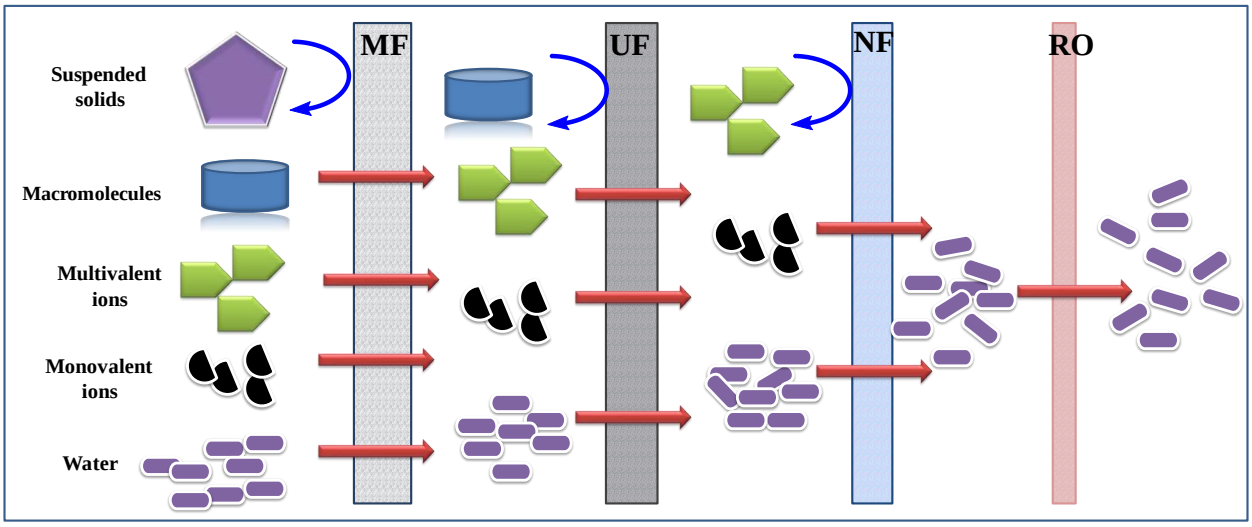

Figure 1.2: Representation for membrane separation by MF, UF, NF, and RO.

The photocatalytic degradation process is an efficient technology for treating wastewater as it can eliminate these harmful pollutants or mineralize these into simpler molecules. The suitability of the photocatalysts in natural sunlight makes photocatalytic degradation a fascinating and less energy-consuming technique for pollutants removal. On the other hand, the adsorption process is also a well-known method for contaminants elimination because of its simplicity, high efficiency, ease of operation, cost-friendly, less energy consumption, and the used adsorbents can be easily regenerable.[59–63] Consequently, adsorption and photocatalytic degradation methods are getting much attention from researchers and are elaborated on below.

1.1.2.1 Adsorption

The adsorption process is a physicochemical attraction among the adsorbate molecules and the adsorbent surface. This process is mainly dependant on different parameters like forces of attraction between adsorbent-adsorbate, pH of the solution, temperature, pressure, concentration, etc. The adsorbent material must possess a high surface area and porosity with appropriate morphology, high chemical, thermal and mechanical stability for easy, rapid, and effective removal of the noxious contaminants from the water bodies.[64,65] The pollutant molecules act as an adsorbate in the adsorption process and these molecules get adsorbed on the adsorbent surface to establish the equilibrium between the pollutants and the adsorbent surface.

To understand the type of adsorption mechanism (chemisorptions, physisorption), different adsorption isotherms have been investigated, these adsorption mechanisms were shown in **Figure 1.3**.[66] In chemisorptions (chemical adsorption), there is a chemical reaction between the pollutants and the adsorbent, and is an irreversible process. While the physisorption (physical adsorption) type of adsorption deals with the physical interactions forces like Vander Waals forces of attraction, dipole-dipole interactions, hydrogen bonding, etc; and this is a reversible and prominent type of adsorption process.[64,67,68] Consequently, these adsorbents can be easily regenerable after their subsequent batch reactions. The natural resources of adsorbents, inexpensive nature, high adsorption capacity, less maintenance cost, rapid and simultaneous removal of different contaminants, ease of operability, makes adsorption a flexible process for the treatment of wastewater.

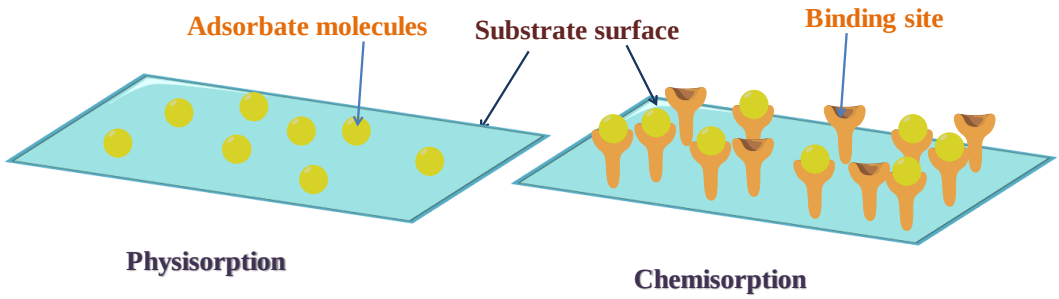

Figure 1.3: Pictorial representation of physisorption and chemisorptions.

1.1.2.2 Photocatalytic degradation

The photocatalytic degradation was tracked so vastly by the wastewater treatment researchers as it was proved to be the proficient and effective technique for the elimination of the noxious contaminants from the wastewater for the cleanliness rationales. This wastewater quantity has been increased bit by bit due to the industrialization and modernization of society.[69,70] As already mentioned in the above section, natural sunlight can also be used for the degradation experiments because it is an eco-friendly energy source and satiates the energy necessity without harming our environment, so this technique fits in the cost-effective, and safer category. For the photocatalytic degradation mechanism, these key points are followed: (a) movement of pollutant molecules present in reaction solution to the surface of the catalyst, (b) pollutant's adsorption, (c) photocatalysis in the adsorbed state, (d) desorption of the degraded products; and (f) detachment

of the final products from the border.[71,72] The mechanism for photocatalytic degradation is elaborated in **Chapter 3**.

1.2 Research gap

In this study, the target organic pollutants were from the class of dyes, endocrine-disrupting compounds, or pharmaceuticals which raises more and more concern due to the increasing evidence of their adverse harmful or estrogenic effect on aquatic organisms and human beings. Currently used wastewater processes remove less than 80% of organic pollutants (EDCs or estrogens) on average. However, due to its significant biological potency little quantity is still able to cause an adverse estrogenic effect on the aquatic organism. As a result, adsorption and advanced treatment technology have to be explored in the hope of success of higher removal efficiency. So, the removal of organic pollutants by various adsorbents like metal modified zeolite and zeolite-based photocatalysts are the potential new alternative. Some research gaps are outlined and given below.

- Removal of organic pollutants which are in the category of endocrine disruptors (e.g. fipronil, bisphenol S, atrazine, etc) with modified zeolite/clay like H-ZSM-5, BETA, and mordenite zeolite has not been thoroughly studied in the literature.
- There is very scarce literature available on the modification of adsorbents/photocatalyst (e.g H-ZSM-5, mordenite, BETA, etc.) by rare earth metals, or non-metals or metal-free materials (e.g carbon nitride).
- No literature has been reported for the application of cerium oxide as a potential adsorbent for the removal of EDCs.

1.3 Objectives

The main purpose of this work is to prepare various adsorbents/photocatalysts for the effective removal of toxic organic pollutants from their aqueous solution. The specific objectives are as follows:

- Surface modification of various adsorbents/photocatalysts (e.g. zeolites, clays, etc.) by metal oxides/nitrides.
- Study of adsorption and photocatalytic properties of synthesized materials for the removal of organic pollutants.

- Study and characterization of the photodegradation products.
- Study of equilibrium, kinetics, and thermodynamics for the adsorption/photocatalysis of pollutants.

1.4 Thesis overview

The present thesis has been divided into **eight chapters**. The different zeolite materials were modified with metal oxide (CeO_2) to investigate their adsorptive removal against fipronil insecticide. The adsorption isotherms, kinetics, and thermodynamics were studied along with the structures of different types of zeolites. The modified zeolites were characterized by N_2 adsorption-desorption, X-ray diffraction analysis (XRD), scanning electron microscopy (SEM), high-resolution transmission electron microscopy (HRTEM), energy-dispersive X-ray spectroscopy analysis (EDX), X-ray photoelectron spectroscopy (XPS) to analyze the surface area, crystallinity, elemental composition, morphologies, surface chemical bonding states, and detailed study about structure, porosity, phase, planes or d-spacing. Furthermore, the zeolite was modified with photoactive materials (g-C_3N_4 and Carbon-dots) to test its photoactivity towards dyes (methylene blue and rhodamine B), insecticides (fipronil), or pharmaceutical drugs (metronidazole). Kinetics analysis was explored to determine the rate constants and analysis of degraded products was done by GC-MS.

Novelty statement: This PhD work deals with the removal of fipronil insecticide with rare earth metal (Cerium) modified zeolite. According to our knowledge, rare earth metal modified zeolite (RMZ) was rarely used as an adsorbents for effective removal of the contaminants. The RMZ have been used widely as catalysts in the petrochemical industries for the production of commercially important petrochemicals such as cumene, cymene, ethylbenzene etc., CO_2 capturing[73–76] but not exploited very much for adsorptive removal of pollutants (e.g. insecticides).

References

(1) Rathi, A.; Basu, S.; Barman, S. Adsorptive Removal of Fipronil from Its Aqueous Solution by Modified Zeolite HZSM-5: Equilibrium, Kinetic and Thermodynamic Study. *J. Mol. Liq.* **2019**, *283*, 867–878. https://doi.org/10.1016/j.molliq.2019.02.140.

(2) Petrie, B.; Barden, R.; Kasprzyk-Hordern, B. A Review on Emerging Contaminants in Wastewaters and the Environment: Current Knowledge, Understudied Areas and Recommendations for Future Monitoring. *Water Res.* **2015**, *72* (0), 3–27.

https://doi.org/10.1016/j.watres.2014.08.053.

(3) Fu, J.; Zhao, C.; Luo, Y.; Liu, C.; Kyzas, G. Z.; Luo, Y.; Zhao, D.; An, S.; Zhu, H. Heavy Metals in Surface Sediments of the Jialu River, China: Their Relations to Environmental Factors. *J. Hazard. Mater.* **2014**, *270*, 102–109. https://doi.org/10.1016/j.jhazmat.2014.01.044.

(4) Lao, W.; Tsukada, D.; Greenstein, D. J.; Bay, S. M.; Maruya, K. A. Analysis, Occurrence, and Toxic Potential of Pyrethroids, and Fipronil in Sediments from an Urban Estuary. *Environ. Toxicol. Chem.* **2010**, *29* (4), 843–851. https://doi.org/10.1002/etc.116.

(5) Rathi, A.; Basu, S.; Barman, S. Structural Framework Effect of Various CeO_2-Loaded Zeolites on the Adsorptive Removal of Fipronil. *J. Environ. Chem. Eng.* **2021**, *9* (2), 105167. https://doi.org/10.1016/j.jece.2021.105167.

(6) Bonmatin, J. M.; Giorio, C.; Girolami, V.; Goulson, D.; Kreutzweiser, D. P.; Krupke, C.; Liess, M.; Long, E.; Marzaro, M.; Mitchell, E. A.; Noome, D. A.; Simon-Delso, N.; Tapparo, A. Environmental Fate and Exposure; Neonicotinoids and Fipronil. *Environ. Sci. Pollut. Res.* **2015**, *22* (1), 35–67. https://doi.org/10.1007/s11356-014-3332-7.

(7) Esplugas, S.; Bila, D. M.; Krause, L. G. T.; Dezotti, M. Ozonation and Advanced Oxidation Technologies to Remove Endocrine Disrupting Chemicals (EDCs) and Pharmaceuticals and Personal Care Products (PPCPs) in Water Effluents. *J. Hazard. Mater.* **2007**, *149* (3), 631–642. https://doi.org/10.1016/j.jhazmat.2007.07.073.

(8) Darbre, P. D. What Are Endocrine Disrupters and Where Are They Found? In *Endocrine Disruption and Human Health*; Elsevier, 2015; pp 3–26. https://doi.org/10.1016/B978-0-12-801139-3.00001-6.

(9) Sharma, S.; Basu, S. Fabrication of Centimeter-Sized Sb_2S_3/SiO_2 Monolithic Mimosa Pudica Nanoflowers for Remediation of Hazardous Pollutants from Industrial Wastewater. *J. Clean. Prod.* **2021**, *280*, 124525. https://doi.org/10.1016/j.jclepro.2020.124525.

(10) Al Amery, N.; Abid, H. R.; Wang, S.; Liu, S. Removal of Methylene Blue (MB) by Bimetallic- Metal Organic Framework. *J. Appl. Mater. Technol.* **2020**, *2* (1), 36–49. https://doi.org/10.31258/jamt.2.1.36-49.

(11) Sharma, S.; Basu, S. Highly Reusable Visible Light Active Hierarchical Porous WO_3/SiO_2 Monolith in Centimeter Length Scale for Enhanced Photocatalytic Degradation of Toxic Pollutants. *Sep. Purif. Technol.* **2020**, *231*, 115916. https://doi.org/10.1016/j.seppur.2019.115916.

(12) Bashiri, F.; Khezri, S. M.; Kalantary, R. R.; Kakavandi, B. Enhanced Photocatalytic Degradation of Metronidazole by TiO_2 Decorated on Magnetic Reduced Graphene Oxide: Characterization, Optimization and Reaction Mechanism Studies. *J. Mol. Liq.* **2020**, *314*, 113608. https://doi.org/10.1016/j.molliq.2020.113608.

(13) Kang, J.; Zhou, L.; Duan, X.; Sun, H.; Wang, S. Catalytic Degradation of Antibiotics by Metal-Free Catalysis over Nitrogen-Doped Graphene. *Catal. Today* **2020**, *357*, 341–349.

https://doi.org/10.1016/j.cattod.2018.12.002.

(14) Malesic-Eleftheriadou, N.; Evgenidou, E.; Lazaridou, M.; Bikiaris, D. N.; Yang, X.; Kyzas, G. Z.; Lambropoulou, D. A. Simultaneous Removal of Anti-Inflammatory Pharmaceutical Compounds from an Aqueous Mixture with Adsorption onto Chitosan Zwitterionic Derivative. *Colloids Surfaces A Physicochem. Eng. Asp.* **2021**, *619*, 126498. https://doi.org/10.1016/j.colsurfa.2021.126498.

(15) Park, E. Y.; Hasan, Z.; Khan, N. A.; Jhung, S. H. Adsorptive Removal of Bisphenol-a from Water with a Metal-Organic Framework, a Porous Chromium-Benzenedicarboxylate. *J. Nanosci. Nanotechnol.* **2013**, *13* (4), 2789–2794. https://doi.org/10.1166/jnn.2013.7411.

(16) Orton, F.; Lutz, I.; Kloas, W.; Routledge, E. J. Endocrine Disrupting Effects of Herbicides and Pentachlorophenol: In Vitro and in Vivo Evidence. *Environ. Sci. Technol.* **2009**, *43* (6), 2144–2150. https://doi.org/10.1021/es8028928.

(17) Zaccaroni, A.; Gamberoni, M.; Mandrioli, L.; Sirri, R.; Mordenti, O.; Scaravelli, D.; Sarli, G.; Parmeggiani, A. Thyroid Hormones as a Potential Early Biomarker of Exposure to 4-Nonylphenol in Adult Male Shubunkins (Carassius Auratus). *Sci. Total Environ.* **2009**, *407* (10), 3301–3306. https://doi.org/10.1016/j.scitotenv.2009.01.036.

(18) Campbell, C. G.; Borglin, S. E.; Green, F. B.; Grayson, A.; Wozei, E.; Stringfellow, W. T. Biologically Directed Environmental Monitoring, Fate, and Transport of Estrogenic Endocrine Disrupting Compounds in Water: A Review. *Chemosphere* **2006**, *65* (8), 1265–1280. https://doi.org/10.1016/j.chemosphere.2006.08.003.

(19) Giesy, J. P.; Hilscherova, K.; Jones, P. D.; Kannan, K.; Machala, M. Cell Bioassays for Detection of Aryl Hydrocarbon (AhR) and Estrogen Receptor (ER) Mediated Activity in Environmental Samples. *Mar. Pollut. Bull.* **2002**, *45* (1–12), 3–16. https://doi.org/10.1016/S0025-326X(02)00097-8.

(20) Kim, S. D.; Cho, J.; Kim, I. S.; Vanderford, B. J.; Snyder, S. A. Occurrence and Removal of Pharmaceuticals and Endocrine Disruptors in South Korean Surface, Drinking, and Waste Waters. *Water Res.* **2007**, *41* (5), 1013–1021. https://doi.org/10.1016/j.watres.2006.06.034.

(21) EPA. Executive Summary: Neonatal Encephalopathy and Neurologic Outcome, Second Edition. Report of the American College of Obstetricians and Gynecologists' Task Force on Neonatal Encephalopathy. *Obstet. Gynecol.* **2014**, *123* (4), 896–901. https://doi.org/10.1097/01.AOG.0000445580.65983.d2.

(22) Snyder, S. A.; Westerhoff, P.; Yoon, Y.; Sedlak, D. L. Pharmaceuticals, Personal Care Products, and Endocrine Disruptors in Water: Implications for the Water Industry. *Environ. Eng. Sci.* **2003**, *20* (5), 449–469. https://doi.org/10.1089/109287503768335931.

(23) Vasylieva, N.; Barnych, B.; Wan, D.; El-Sheikh, E. S. A.; Nguyen, H. M.; Wulff, H.; McMahen, R.; Strynar, M.; Gee, S. J.; Hammock, B. D. Hydroxy-Fipronil Is a New Urinary Biomarker of Exposure to Fipronil. *Environ. Int.* **2017**, *103*, 91–98.

https://doi.org/10.1016/j.envint.2017.03.012.

(24) Zhang, Q.; Zhang, L.; Li, Z.; Zhang, L.; Li, D. Enhancement of Fipronil Degradation with Eliminating Its Toxicity in a Microbial Fuel Cell and the Catabolic Versatility of Anodic Biofilm. *Bioresour. Technol.* **2019**, *290*, 121723. https://doi.org/10.1016/j.biortech.2019.121723.

(25) National Pesticide Information Center. Fipronil Technical Fact Sheet. *http//npic.orst.edu/factsheets/fipronil.pdf [accessed 4 Febr. 2016]* **2016**, 1–3.

(26) Wu, J.; Lu, J.; Lu, H.; Lin, Y.; Chris Wilson, P. Occurrence and Ecological Risks from Fipronil in Aquatic Environments Located within Residential Landscapes. *Sci. Total Environ.* **2015**, *518–519*, 139–147. https://doi.org/10.1016/j.scitotenv.2014.12.103.

(27) Ensminger, M. P.; Budd, R.; Kelley, K. C.; Goh, K. S. Pesticide Occurrence and Aquatic Benchmark Exceedances in Urban Surface Waters and Sediments in Three Urban Areas of California, USA, 2008-2011. *Environ. Monit. Assess.* **2013**, *185* (5), 3697–3710. https://doi.org/10.1007/s10661-012-2821-8.

(28) da Silva, D. R. O.; de Avila, L. A.; Agostinetto, D.; Dal Magro, T.; de Oliveira, E.; Zanella, R.; Noldin, J. A. Pesticides Monitoring in Surface Water of Rice Production Areas in Southern Brazil. *Cienc. Rural* **2009**, *39* (9), 2383–2389. https://doi.org/10.1590/s0103-84782009000900001.

(29) Prajapati, A. K.; Mondal, M. K. Development of CTAB Modified Ternary Phase α-Fe_2O_3-Mn_2O_3-Mn_3O_4nanocomposite as Innovative Super-Adsorbent for Congo Red Dye Adsorption. *J. Environ. Chem. Eng.* **2021**, *9* (1), 104827. https://doi.org/10.1016/j.jece.2020.104827.

(30) Vasiljevic, Z. Z.; Dojcinovic, M. P.; Vujancevic, J. D.; Jankovic-Castvan, I.; Ognjanovic, M.; Tadic, N. B.; Stojadinovic, S.; Brankovic, G. O.; Nikolic, M. V. Photocatalytic Degradation of Methylene Blue under Natural Sunlight Using Iron Titanate Nanoparticles Prepared by a Modified Sol-Gel Method: Methylene Blue Degradation with Fe_2TiO_5. *R. Soc. Open Sci.* **2020**, *7* (9), 200708. https://doi.org/10.1098/rsos.200708.

(31) Hou, C.; Hu, B.; Zhu, J. Photocatalytic Degradation of Methylene Blue over TiO_2 Pretreated with Varying Concentrations of NaOH. *Catalysts* **2018**, *8* (12), 575. https://doi.org/10.3390/catal8120575.

(32) Baldev, E.; MubarakAli, D.; Ilavarasi, A.; Pandiaraj, D.; Ishack, K. A. S. S.; Thajuddin, N. Degradation of Synthetic Dye, Rhodamine B to Environmentally Non-Toxic Products Using Microalgae. *Colloids Surfaces B Biointerfaces* **2013**, *105*, 207–214. https://doi.org/10.1016/j.colsurfb.2013.01.008.

(33) Yu, K.; Yang, S.; He, H.; Sun, C.; Gu, C.; Ju, Y. Visible Light-Driven Photocatalytic Degradation of Rhodamine B over $NaBiO_3$: Pathways and Mechanism. *J. Phys. Chem. A* **2009**, *113* (37), 10024–10032. https://doi.org/10.1021/jp905173e.

(34) Monga, D.; Basu, S. Enhanced Photocatalytic Degradation of Industrial Dye by g-

C_3N_4/TiO_2 Nanocomposite: Role of Shape of TiO_2. *Adv. Powder Technol.* **2019**, *30* (5), 1089–1098. https://doi.org/10.1016/j.apt.2019.03.004.

(35) Carneiro, J. O.; Samantilleke, A. P.; Parpot, P.; Fernandes, F.; Pastor, M.; Correia, A.; Luís, E. A.; Chivanga Barros, A. A.; Teixeira, V. Visible Light Induced Enhanced Photocatalytic Degradation of Industrial Effluents (Rhodamine B) in Aqueous Media Using TiO_2 Nanoparticles. *J. Nanomater.* **2016**, *2016*, 1–13. https://doi.org/10.1155/2016/4396175.

(36) Naveed, S. Degradation Study of Metronidazole in Active and Different Formulation by UV Spectroscopy. *J. Bioequiv. Availab.* **2014**, *06* (04). https://doi.org/10.4172/jbb.10000191.

(37) Barrios-Estrada, C.; de Jesús Rostro-Alanis, M.; Muñoz-Gutiérrez, B. D.; Iqbal, H. M. N.; Kannan, S.; Parra-Saldívar, R. Emergent Contaminants: Endocrine Disruptors and Their Laccase-Assisted Degradation – A Review. *Sci. Total Environ.* **2018**, *612*, 1516–1531. https://doi.org/10.1016/j.scitotenv.2017.09.013.

(38) Sharma, S.; Basu, S. Visible-Light-Driven Efficient Photocatalytic Abatement of Recalcitrant Pollutants by Centimeter-Length MoO_3/SiO_2 Monoliths with Long Service Life. *Appl. Mater. Today* **2021**, *23*, 101033. https://doi.org/10.1016/j.apmt.2021.101033.

(39) Prajapati, A. K.; Mondal, M. K. Comprehensive Kinetic and Mass Transfer Modeling for Methylene Blue Dye Adsorption onto CuO Nanoparticles Loaded on Nanoporous Activated Carbon Prepared from Waste Coconut Shell. *J. Mol. Liq.* **2020**, *307*, 112949. https://doi.org/10.1016/j.molliq.2020.112949.

(40) Dashairya, L.; Sharma, S.; Rathi, A.; Saha, P.; Basu, S. Solar-Light-Driven Photocatalysis by Sb_2S_3/Carbon Based Composites towards Degradation of Noxious Organic Pollutants. *Mater. Chem. Phys.* **2021**, *273*, 125120. https://doi.org/10.1016/j.matchemphys.2021.125120.

(41) Terçariol, P. R. G.; Godinho, A. F. Behavioral Effects of Acute Exposure to the Insecticide Fipronil. *Pestic. Biochem. Physiol.* **2011**, *99* (3), 221–225. https://doi.org/10.1016/j.pestbp.2010.12.007.

(42) Lee, S.-J.; Mulay, P.; Diebolt-Brown, B.; Lackovic, M. J.; Mehler, L. N.; Beckman, J.; Waltz, J.; Prado, J. B.; Mitchell, Y. A.; Higgins, S. A.; Schwartz, A.; Calvert, G. M. Acute Illnesses Associated with Exposure to Fipronil—Surveillance Data from 11 States in the United States, 2001–2007. *Clin. Toxicol.* **2010**, *48* (7), 737–744. https://doi.org/10.3109/15563650.2010.507548.

(43) Huang, X.; Lin, J.; Yuan, D. Simple and Sensitive Determination of Nitroimidazole Residues in Honey Using Stir Bar Sorptive Extraction with Mixed Mode Monolith Followed by Liquid Chromatography. *J. Sep. Sci.* **2011**, *34* (16–17), 2138–2144. https://doi.org/10.1002/jssc.201000880.

(44) Hu, G.; Yang, J.; Duan, X.; Farnood, R.; Yang, C.; Yang, J.; Liu, W.; Liu, Q. Recent Developments and Challenges in Zeolite-Based Composite Photocatalysts for

Environmental Applications. *Chem. Eng. J.* **2021**, *417*, 129209. https://doi.org/10.1016/j.cej.2021.129209.

(45) Nagar, A.; Basu, S. Ternary g-C_3N_4/Ag/$BiVO_4$ Nanocomposite: Fabrication and Implementation to Remove Organic Pollutants . *Environ. Technol. Innov.* **2021**, *23*, 101646. https://doi.org/10.1016/j.eti.2021.101646.

(46) Kundu, A.; Sharma, S.; Basu, S. Modulated BiOCl Nanoplates with Porous g-C_3N_4 Nanosheets for Photocatalytic Degradation of Color/Colorless Pollutants in Natural Sunlight. *J. Phys. Chem. Solids* **2021**, *154*, 110064. https://doi.org/10.1016/j.jpcs.2021.110064.

(47) Hasan, Z.; Khan, N. A.; Jhung, S. H. Adsorptive Removal of Diclofenac Sodium from Water with Zr-Based Metal–Organic Frameworks. *Chem. Eng. J.* **2016**, *284*, 1406–1413. https://doi.org/10.1016/j.cej.2015.08.087.

(48) Cook, M. M.; Symonds, E. M.; Gerber, B.; Hoare, A.; Van Vleet, E. S.; Breitbart, M. Removal of Six Estrogenic Endocrine-Disrupting Compounds (EDCs) from Municipal Wastewater Using Aluminum Electrocoagulation. *Water (Switzerland)* **2016**, *8* (4), 128. https://doi.org/10.3390/w8040128.

(49) Bazrafshan, E.; Kord Mostafapour, F.; Farzadkia, M.; Ownagh, K. A.; Mahvi, A. H. Slaughterhouse Wastewater Treatment by Combined Chemical Coagulation and Electrocoagulation Process. *PLoS One* **2012**, *7* (6), e40108. https://doi.org/10.1371/journal.pone.0040108.

(50) Katibi, K. K.; Yunos, K. F.; Man, H. C.; Aris, A. Z.; bin Mohd Nor, M. Z.; binti Azis, R. S. Recent Advances in the Rejection of Endocrine-Disrupting Compounds from Water Using Membrane and Membrane Bioreactor Technologies: A Review. *Polymers (Basel).* **2021**, *13* (3), 1–52. https://doi.org/10.3390/polym13030392.

(51) Aziman, E. S.; Mohd Salehuddin, A. H. J.; Ismail, A. F. Remediation of Thorium (IV) from Wastewater: Current Status and Way Forward. *Sep. Purif. Rev.* **2021**, *50* (2), 177–202. https://doi.org/10.1080/15422119.2019.1639519.

(52) Coday, B. D.; Yaffe, B. G. M.; Xu, P.; Cath, T. Y. Rejection of Trace Organic Compounds by Forward Osmosis Membranes: A Literature Review. *Environ. Sci. Technol.* **2014**, *48* (7), 3612–3624. https://doi.org/10.1021/es4038676.

(53) Wang, J.; Chen, X.; Reis, R.; Chen, Z.; Milne, N.; Winther-Jensen, B.; Kong, L.; Dumée, L. F. Plasma Modification and Synthesis of Membrane Materials—a Mechanistic Review. *Membranes (Basel).* **2018**, *8* (3), 56. https://doi.org/10.3390/membranes8030056.

(54) Baghel, R.; Upadhyaya, S.; Chaurasia, S. P.; Singh, K.; Kalla, S. Optimization of Process Variables by the Application of Response Surface Methodology for Naphthol Blue Black Dye Removal in Vacuum Membrane Distillation. *J. Clean. Prod.* **2018**, *199*, 900–915. https://doi.org/10.1016/j.jclepro.2018.07.214.

(55) Cañizares, P.; Martínez, F.; Jiménez, C.; Lobato, J.; Rodrigo, M. A. Coagulation and

Electrocoagulation of Wastes Polluted with Dyes. *Environ. Sci. Technol.* **2006**, *40* (20), 6418–6424. https://doi.org/10.1021/es0608390.

(56) Homem, V.; Santos, L. Degradation and Removal Methods of Antibiotics from Aqueous Matrices - A Review. *J. Environ. Manage.* **2011**, *92* (10), 2304–2347. https://doi.org/10.1016/j.jenvman.2011.05.023.

(57) Sahu, O.; Mazumdar, B.; Chaudhari, P. K. Electrochemical Treatment of Sugar Industry Wastewater: Process Optimization by Response Surface Methodology. *Int. J. Environ. Sci. Technol.* **2019**, *16* (3), 1527–1540. https://doi.org/10.1007/s13762-018-1765-0.

(58) Panizza, M.; Cerisola, G. Direct and Mediated Anodic Oxidation of Organic Pollutants. *Chem. Rev.* **2009**, *109* (12), 6541–6569. https://doi.org/10.1021/cr9001319.

(59) Sharma, M.; Singh, J.; Hazra, S.; Basu, S. Remediation of Heavy Metal Ions Using Hierarchically Porous Carbon Monolith Synthesized via Nanocasting Method. *J. Environ. Chem. Eng.* **2018**, *6* (2), 2829–2836. https://doi.org/10.1016/j.jece.2018.04.042.

(60) Mishra, A.; Mehta, A.; Kainth, S.; Basu, S. Effect of g-C_3N_4 Loading on TiO_2/Bentonite Nanocomposites for Efficient Heterogeneous Photocatalytic Degradation of Industrial Dye under Visible Light. *J. Alloys Compd.* **2018**, *764*, 406–415. https://doi.org/10.1016/j.jallcom.2018.06.089.

(61) Mishra, A.; Mehta, A.; Sharma, M.; Basu, S. Enhanced Heterogeneous Photodegradation of VOC and Dye Using Microwave Synthesized TiO_2/Clay Nanocomposites: A Comparison Study of Different Type of Clays. *J. Alloys Compd.* **2017**, *694*, 574–580. https://doi.org/10.1016/j.jallcom.2016.10.036.

(62) Sharma, M.; Hazra, S.; Basu, S. Kinetic and Isotherm Studies on Adsorption of Toxic Pollutants Using Porous ZnO@SiO_2 Monolith. *J. Colloid Interface Sci.* **2017**, *504*, 669–679. https://doi.org/10.1016/j.jcis.2017.06.020.

(63) Mehta, T.; Rathi, A.; Verma, A.; Barman, S.; Halder, G. Elimination of Fipronil Insecticide by Adsorption Technique from Aqueous Solution by Cu-13X Zeolite Composite: Isotherms, Kinetic and Thermodynamic Studies. *Int. J. Environ. Anal. Chem.* **2020**, *00* (00), 1–17. https://doi.org/10.1080/03067319.2020.1790545.

(64) Gusain, R.; Gupta, K.; Joshi, P.; Khatri, O. P. Adsorptive Removal and Photocatalytic Degradation of Organic Pollutants Using Metal Oxides and Their Composites: A Comprehensive Review. *Adv. Colloid Interface Sci.* **2019**, *272*, 102009. https://doi.org/10.1016/j.cis.2019.102009.

(65) Yagub, M. T.; Sen, T. K.; Afroze, S.; Ang, H. M. Dye and Its Removal from Aqueous Solution by Adsorption: A Review. *Adv. Colloid Interface Sci.* **2014**, *209*, 172–184. https://doi.org/10.1016/j.cis.2014.04.002.

(66) Kennedy, K. K.; Maseka, K. J.; Mbulo, M. Selected Adsorbents for Removal of Contaminants from Wastewater: Towards Engineering Clay Minerals. *Open J. Appl. Sci.* **2018**, *08* (08), 355–369. https://doi.org/10.4236/ojapps.2018.88027.

(67) Rathi, A.; Basu, S.; Barman, S. Adsorptive Removal of Fipronil from Its Aqueous Solution by Modified Zeolite HZSM-5: Equilibrium, Kinetic and Thermodynamic Study. *J. Mol. Liq.* **2019**, *283*, 867–878. https://doi.org/10.1016/j.molliq.2019.02.140.

(68) Zhu, H. Y.; Jiang, R.; Fu, Y. Q.; Li, R. R.; Yao, J.; Jiang, S. T. Novel Multifunctional $NiFe_2O_4$/ZnO Hybrids for Dye Removal by Adsorption, Photocatalysis and Magnetic Separation. *Appl. Surf. Sci.* **2016**, *369*, 1–10. https://doi.org/10.1016/j.apsusc.2016.02.025.

(69) Mehta, A.; Mishra, A.; Sharma, M.; Singh, S.; Basu, S. Effect of Silica/Titania Ratio on Enhanced Photooxidation of Industrial Hazardous Materials by Microwave Treated Mesoporous SBA-15/TiO_2 Nanocomposites. *J. Nanoparticle Res.* **2016**, *18* (7), 209. https://doi.org/10.1007/s11051-016-3523-x.

(70) Sharma, S.; Basu, S.; Shetti, N. P.; Kamali, M.; Walvekar, P.; Aminabhavi, T. M. Waste-to-Energy Nexus: A Sustainable Development. *Environ. Pollut.* **2020**, 115501. https://doi.org/10.1016/j.envpol.2020.115501.

(71) Sánchez-Rodríguez, D.; Méndez Medrano, M. G.; Remita, H.; Escobar-Barrios, V. Photocatalytic Properties of BiOCl-TiO_2 Composites for Phenol Photodegradation. *J. Environ. Chem. Eng.* **2018**, *6* (2), 1601–1612. https://doi.org/10.1016/j.jece.2018.01.061.

(72) Herrmann, J. M. Heterogeneous Photocatalysis: Fundamentals and Applications to the Removal of Various Types of Aqueous Pollutants. *Catal. Today* **1999**, *53* (1), 115–129. https://doi.org/10.1016/S0920-5861(99)00107-8.

(73) Yu, H.; Zang, J.; Liu, G.; Hong, M.; Chen, R.; Chen, T. Acid-Modified Hierarchical Porous Rare-Earth-Containing y Zeolite as a Highly Active and Stable Catalyst for Olefin Removal. *ACS Omega* **2020**, *5* (29), 18028–18034. https://doi.org/10.1021/acsomega.0c01457.

(74) Wang, Y.; Jia, H.; Chen, P.; Fang, X.; Du, T. Synthesis of La and Ce Modified X Zeolite from Rice Husk Ash for Carbon Dioxide Capture. *J. Mater. Res. Technol.* **2020**, *9* (3), 4368–4378. https://doi.org/10.1016/j.jmrt.2020.02.061.

(75) Thakur, R.; Gupta, R. K.; Barman, S. A Comparative Study of Catalytic Performance of Rare Earth Metal-Modified Beta Zeolites for Synthesis of Cymene. *Chem. Pap.* **2017**, *71* (1), 137–148. https://doi.org/10.1007/s11696-016-0071-x.

(76) Gautam, P.; Barman, S.; Ali, A. Catalytic Performance of Cerium-Modified ZSM-5 Zeolite as a Catalyst for the Esterification of Glycerol with Acetic Acid. *Int. J. Chem. React. Eng.* **2020**, *18* (9). https://doi.org/10.1515/ijcre-2020-0081.

Chapter 2: Literature review and zeolite framework

This chapter deals with the literature survey of the different noxious contaminants (EDCs, or dyes) which were removed from their aqueous solution either by adsorption or photocatalytic oxidation over zeolite-based composites or other composites. The adsorption capacities of various zeolites for the removal of FIP and photocatalytic degradation efficiencies of various photocatalysts towards the MB and RhB dye pollutants were tabulated. The pros and cons of various other materials such as carbonaceous materials, metal-organic frameworks, zeolites, carbon nanotubes, adsorbents, and activated carbon materials were also briefly discussed. The structural properties along with their significance in adsorption and photocatalytic degradation were explored. In comparison to other support materials zeolites were found to be an appropriate substance for the hybrid adsorption and photocatalysis process, because it has a huge surface area for adsorption, tunable pore size, high ion-exchange capability, and the abundance of acidic-basic sites which make zeolite more active towards adsorption and photocatalytic degradation.[1,2]

2.1 Literature review

The presence of new emerging organic contaminants e.g., EDCs, pharmaceuticals, or dyes in the contaminated wastewater has resulted in health-related problems and environmental deterioration. The toxic effluent of established industries or hospitals wastes directly affects aquatic bodies.[3–7] Especially the group of organic pollutants which fall in the category of EDCs can cause an imbalance in the hormonal systems affecting reproductive issues, cancer, miscarriages, endometriosis, and infertility in humans. Therefore, there is a crucial need for the effective removal of these noxious organic contaminants.[8] Some selected literature on organic pollutants (EDCs, dyes, and pharmaceuticals) removal by various adsorbents/photocatalysts is shown in **Table 2.1.**

The organic pollutants can be eradicated from the wastewater by adsorption or photodegradation techniques.[9,10] For the adsorption process, the adsorbent bed must possess a huge surface area, tendency to adsorb noxious contaminants, and porosity while in the photocatalysis process the photoactive material has to be fabricated over porous support material.

Table 2.1: The comparative table for the removal of different pollutants by various adsorbents/photocatalysts

Name of pollutant	Adsorbent/photocatalyst used	% Removal (rate constant 'k')	Optimized parameters (dose, pH, time)	Ref.
Bisphenol A	TiO_2	~70%	10.0g/L, pH 6, time: 60 min	11
Diclofenac	CTAC (*Cyclamen persicum* tubers based activated carbon)	81%	14g/L, pH 2, time: 120 min	12
α-naphthol	Fe_3O_4@PANI (polyaniline coated Fe_3O_4)	91.11%	20mg, pH 7, time: 300 min	13
FIP	White rot fungus (*Trametes versicolor*)	96.5%	$t_{1/2}$=4.2d, pH 9	14
FIP	Metal-organic-framework (M-ZIF-8@ZIF-67)	95%	45min, 3.75 g/L, pH 6	15
MB	ZnS and CdS nanoparticles	73 % ($k = 0.00361\ min^{-1}$)	0.1 g/L, 360 min	16
MB	Hematite (α-Fe_2O_3) nanoparticle	97% ($k = 0.00462\ min^{-1}$)	2.5 g/L, 500 min	17
MB	(Yb, N)-TiO_2	93.55%	3 g/L, 300 min	18
MB	Ag-TiO_2/zeolite	93.08%	1 g/L, 90 min	19
RhB	TiO_2-rGO	81% ($k = 0.005\ min^{-1}$)	0.4 g/L, 320 min	20
RhB	g-C_3N_4	$k = 0.014\ min^{-1}$	1 g/L, 30 min	21
RhB	g-C_3N_4/TiO_2 (P25)	74% ($k = 0.0217\ min^{-1}$)	0.4 g/L, 80 min	22
RhB	ZnO/zeolite A	99.4%	1g/L, 63 min,	23
MET	Activated carbon@ZnO composite	83%	2 g/L, 30 min, pH 11	24
MET	Na@giniite particles	91.2 % ($k = 0.2918\ h^{-1}$)	0.2 g/L, 9h, pH 2.8	25
MET	MgO nanoparticles	93.2%	0.1 g/L, 180 min, pH 6	26

For the preparation of adsorbents[27] or photocatalysts, various inorganic support materials like cellulose-based adsorbents, metal-organic frameworks, activated carbon, glass, carbon nanotubes, and zeolites were used.[1,28,29] These materials provide the adsorption sites on their

surfaces for the removal of the contaminants and also allow the photoactive materials to perform their photocatalytic activities. In addition, the dispersion effect reduces the chances of aggregation or crystallite size growth of photoactive particles, however, promotes the easy recovery and separation of the material from the aqueous medium.

2.2 Zeolite frameworks as adsorbents/photocatalysts

The zeolite frameworks have been considered as a promising adsorbent among the different support materials because of their salient features like huge active surface area, stability of structures, regenerability, and high adsorption capacity, an abundance of acidic and basic sites which helps in reducing e^-/h^+ pair recombination and tunable surface properties. The conventional zeolite frameworks consist of aluminosilicate-type skeletal with SiO_4 and AlO_4 tetrahedral units. Each tetrahedral unit of AlO_4 possesses a net negative charge which needs to be balanced by extra exchangeable cations like H^+, Na^+, K^+, Ca^{2+}, Mg^{2+}, Ce^{3+} and others. Moreover, these cationic species are loosely held and can be readily exchanged in mild conditions. The stability of zeolite structures and its performance as adsorbent depends on the nature of exchanged cations and their ionic properties which influences the adsorption.[1,30] The zeolites like ZSM-5 (zeolite Socony Mobil-5), Mordenite, beta, and faujasite type (13X) have been discussed as they have a high surface area, pore size, and are most frequently used for the adsorption and photodegradation processes. These zeolites have been used after modification with some metals to enhance their adsorptive/photocatalytic properties.

The ZSM-5 zeolite (**Figure 2.1a**) is a medium pore zeolite with 0.51 nm x 0.56 nm which easily allows small molecules to disperse inside the cavities. It also posses 2 intersecting channel networks that form a 3-D network system.[31,32] It has strong acidity, C-C bond scission, and exclusive pore cavities that reduce the formation of coke, such properties make this zeolite an appropriate candidate for photocatalytic degradation. The modification with transition metals makes the zeolite oxidation photocatalysts, which effectively works in the liquid phase and can be easily utilized for wastewater degradation purposes.[33] The special orientation of cavities and pore channels allows the crystalline zeolite to provide space for the molecule's position and activity.

Zeolite 13X is a faujasite type of zeolite with a 3-dimensional structure. It is comprised of an alumino-silicate tetrahedral structure with beta-cage as a structural basic unit and adjacent to

this there is a 6-angle prism connection to form a molecular sieve. The positions of SI, SI', SII, and SIII (**Figure 2.1b**) are available in 13X zeolite.[34] Whereas, mordenite zeolite (MOR) (**Figure 2.1c**) is comprised of 3 different cavities, a 12-membered ringed structure, oval shape 8-membered side ring channels, and link cavity channels. Probable positions of cations over the zeolite framework were categorized and suggested that the cation occupies primarily Mortier positions i.e. β-sites and α-sites.[35]

The BETA zeolite (**Figure 2.1d**) is a large pore-sized zeolite with a 3-D complex framework structure and has a 12-membered ring with a 7.1 Å pore size and has varied applications in petrochemical industries, fine chemicals, and photocatalysis.[36] It is composed of 3 polymorphic structural forms (A, B, C). The positions of Al/Si substitutions in the zeolite structure are significant for the stability of the cation (metal) position in exchanged frameworks.[35] It acts as an active host for accommodating reactants and their degraded side products inside their cavities, which leads the molecules to the photoactive semiconductors for the photocatalysis phenomenon. The beta zeolite was observed to be a better supporting zeolite as it has a huge adsorption capacity than ZSM-5 zeolite. The nano-sized crystalline beta zeolite has attracted more attention from scientists than large crystalline zeolite materials. This decreased size of zeolite to nano-scale level leads to an increase in surface area and catalytic activity as it reduces the dispersion paths.[37]

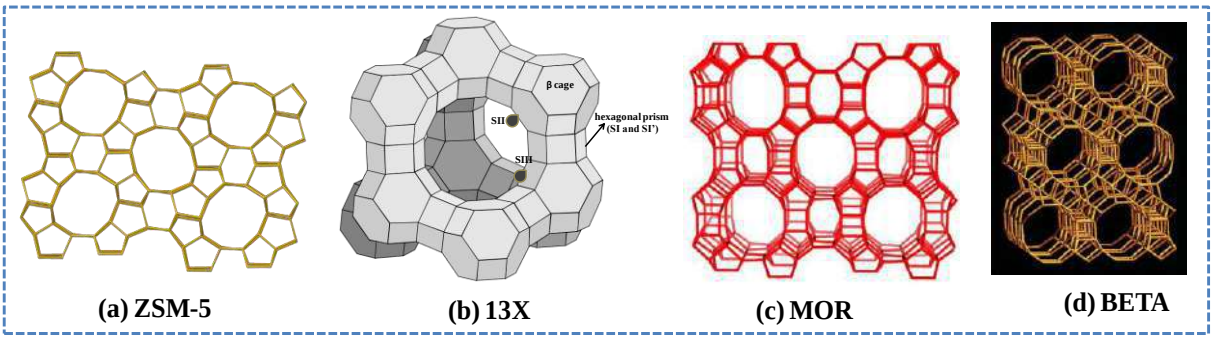

Figure 2.1: The zeolite structures of ZSM-5, 13X, MOR, and BETA zeolite.[36,38]

In general, with the change in Si/Al or SiO_2/Al_2O_3 ratios, the structural properties of zeolites changes like hydrophobicity and resistance to acids increases with Si/Al ratios. based on Si/Al ratios the zeolites have been divided mainly into 3 categories: low silica, intermediate

silica, and high silica zeolites with Si/Al ratios < 2, 2-5, and > 5 respectively.[1,39] The beta zeolite has a comparatively high ratio of Si/Al (~13) as compared to 13X zeolite. The faujasite type X zeolite has 1.0-1.5 (Si/Al ratio) while Mordenite also having a relatively higher Si/Al ratio. With this low value of Si/Al ratio, the 13X zeolite leads to deactivation in the company of the water medium.[40] This ratio increases the stability of the zeolite in the acidic stream and also promotes higher metal loadings.[41] For environment remediation, high silica zeolites have been implied for the elimination of noxious organic contaminants. These features promote the zeolite-based adsorbents and photocatalyst for water treatment to tackle environmental issues. To make a zeolite an efficient material the photoactive/semiconductor material needs to be fabricated over the zeolite for water treatment processes. The comparison of these mentioned zeolites with organic pollutants has been tabularized in **Table 2.2**.

Table 2.2: The removal of pollutants by zeolite based materials zeolites

Zeolite-based materials	**Description**
In-TiO_2(50%)/HZSM-5	Implied for the degradation of MO dye (10 ppm) in 30 min under a UV light source of 20 W and 60% of degradation was achieved[42]
Fe_3O_4@MOR@CuO core-shell composite	The pollutant MB dye was tested in the presence of H_2O_2 and resulted in 93% efficiency which suggests that Fe_3O_4@MOR@CuO core-shell composite is more stable than other core-shell nanomaterials/other nano-composites[43]
$H_6P_2W_{18}O_{62}$/TiO_2/BET A zeolite	70 mg of the catalyst was used to degrade MO dye with 70% of photocatalytic efficiency in 120 min under12 W lamps[44]
AgBr/Ag_2CO_3-Fe/MOR	70 mg dose of the catalyst was used to degrade the MB dye of concentration 3.2 ppm under a 200 W tungsten lamp in 75 min of contact time and 90% of removal was achieved[45]
B-TiO_2(20%)/HZSM-5	Azophloxine dye was removed with an efficiency of 61.8% at optimum conditions: catalyst dose 400 mg/L, dye concentration 40 mg/L in contact time of 30 min[46]
ZnO/Ag/ZSM-5	Methyl Orange of 20 ppm concentration was removed with catalyst dose of 250 mg, in 180 min and % removal of 90% was achieved [47]
Au-NPs/HX	Implied to remove 63.9% of phenol with a dose of 50 mg in 120 min of contact time[48]

TiO_2/HBETA	Implied for 90% degradation of diclofenac with100 mg of catalyst dose under 125 W high-pressure Hg lamp in 240 min of contact time [49]
CeO_2/NaX	Used to remove MO dye of 5 ppm concentration with a dose of 50 mg and 90% of removal was observed[50]
Z/CeO_2/NC	Zeolite/Cerium oxide nanocomposite (Z/CeO_2–NC) was hydrothermally synthesized to remove MB dye by adsorption process and maximum efficiency of 93.9% was achieved[51]
CeO_2–Ce_2S_3	Acetamiprid was removed with 82% of removal efficiency in 180 min[52]
$Bi_2Sn_2O_7$/C_3N_4/Y	The different wt% of zeolite was varied and best composite was utilized to remove tetracycline antibiotic (20 ppm) in 120 min at pH 6 and ~80% was achieved[53]
C_3N_4/Tungstophosphoric acid	Used to remove the acetamiprid pollutants and 43% of photodegradation was achieved in 180 min under visible light illumination[52]

These zeolite-based materials have been widely utilized for the removal of noxious contaminants from the water bodies. The BETA zeolite was fabricated with $H_6P_2W_{18}O_{62}$, Au, and TiO_2 and was used for the elimination of MO dye and diclofenac.[44,49] The ZSM-5 zeolite was fabricated with TiO_2 particles, zinc oxide/Ag in order to remove methyl orange (MO), and azophloxine dye.[42,46,47] But not more than 90% of efficiency was achieved. The MOR zeolite was used to form Fe_3O_4@MOR@CuO core-shell and AgBr/Ag_2CO_3-Fe/MOR composites to eliminate MB dye with 93% and 90% efficiency, but in the case of core-shell composite H_2O_2 was also applied which is not a cost-friendly.

2.3 Various fabricated semiconductor materials

The various semiconductor materials fabricated on zeolite surfaces for adsorption or photodegradation purposes have been elaborated below:

2.3.1 CeO_2 (Cerium oxide)

Cerium metal (CeO_2) is recently preferred to be used in photocatalytic degradation owing to its exclusive properties.[54] The redox character of CeO_2 is a potent feature as it proficiently exists in

two oxidation states (Ce^{3+}/Ce^{4+}).[55] As CeO_2 is having a high oxidation state and thermal stability, it can be applied for the modification of various adsorbents to enhance adsorption capacity.[56] This capability of high adsorption helps to eradicate the anionic species and have resistance against acidic conditions.[57] The CeO_2 particles are less soluble in acid medium and don't elute while used for the water treatment processes like adsorption/photodegradation.[51] The cerium oxides have significant capabilities in destructing or wiping out the noxious organophosphate compounds like pesticides/insecticides.[58]

2.3.2 g-C_3N_4 (graphitic carbon nitride)

Wang and coworkers brought the revolution of graphitic carbon nitride (g-C_3N_4) with a 2-D polymeric structure that attracted much attention for various applications.[59,60] Due to its fascinating properties, g-C_3N_4 is widely used in recent years that include facile synthesis, low-cost precursors, and stable physicochemical properties with medium electronic band structure.[61–63] It can be developed as a metal-free, nontoxic potential photocatalyst with a good response in visible light with a bandgap of 2.7 eV.[62,64–66] Additionally, in an ambient condition, it is chemically and thermally stable, having low density, layered structure, resistivity towards the water. Biocompatibility originates it greatly promising in the area of photocatalysis. Regardless of having these amazing properties, lacking in visible-light absorption, high recombination of the photo-induced electron/hole pairs, less surface area, and reduced morphological properties obstruct their extensive exploitation in photocatalytic processes.[62,63,67] To conquer these limitations, the most suitable method is to fabricate with the material which has a high surface area for adsorption and also reduces the recombination rate.

2.3.3 C-dots (Carbon dots)

The C-dots in the size range of 1-10 nm are nanostructured carbon materials which possess strong and tunable chemical properties. They are photoluminescent nanoparticles possessing very little toxicity, potent and compatible structures with high stability, and interesting photocatalytic traits.[68–70] These interesting properties provide a wide range of applications like sensing,[71] drug delivery, bioimaging, photocatalysis, and electrocatalysis. The C-dot structures have delocalized conjugated π-bonds which promotes fast charge separation and photo-induced charge carrier movement, and finally improves the photocatalytic efficiency.[72,73] The carbon of

C-dots is sp^2/sp^3 hybridized which holds the fine electron transferring or storage property.[74,75] They can act as an efficient photocatalyst as well as photovoltaic cells due to their light absorber property.[76] A new temperature-controlled fluorescent particle has been synthesized by introducing C-dots into the templates of polyvinyl alcohol, potassium alum, and polyurethane.[77–79] These templates can hinder the vibrations and rotations of the exposed functional groups on C-dots at the intramolecular level, and hence stabilizes the triplet excited states. On the other hand, these C-dots are small crystal-like structure and gives lesser yield on synthesis in batches, while their reusability is not an easy task and time consuming too. These C-dots are rich in surface active groups which promote its attachment to the other materials for forming potent composite materials. These C-dots have some demerits like separation problem, decrease in efficiency due to oxidation;[80] but their photoactivity creates an impact in the field of photodegradation, therefore C-dot composites are upgraded.

References

(1) Hu, G.; Yang, J.; Duan, X.; Farnood, R.; Yang, C.; Yang, J.; Liu, W.; Liu, Q. Recent Developments and Challenges in Zeolite-Based Composite Photocatalysts for Environmental Applications. *Chem. Eng. J.* **2021**, *417*, 129209. https://doi.org/10.1016/j.cej.2021.129209.

(2) Rathi, A.; Basu, S.; Barman, S. Structural Framework Effect of Various CeO_2-Loaded Zeolites on the Adsorptive Removal of Fipronil. *J. Environ. Chem. Eng.* **2021**, *9* (2), 105167. https://doi.org/10.1016/j.jece.2021.105167.

(3) Edward Charles Dodds and W. Lawson. Molecular Structure in Relation to Oestrogenic Activity. Compounds without a Phenanthrene Nucleus. *Proc. R. Soc. London. Ser. B - Biol. Sci.* **1938**, *125* (839), 222–232. https://doi.org/10.1098/rspb.1938.0023.

(4) Sohoni, P.; Sumpter, J. P. Several Environmental Oestrogens Are Also Anti-Androgens. *J. Endocrinol.* **1998**, *158* (3), 327–339. https://doi.org/10.1677/joe.0.1580327.

(5) Retana-Márquez, S.; Hernández, H.; Flores, J. A.; Muñoz-Gutiérrez, M.; Duarte, G.; Vielma, J.; Fitz-Rodríguez, G.; Fernández, I. G.; Keller, M.; Delgadillo, J. A. Effects of Phytoestrogens on Mammalian Reproductive Physiology. *Trop. Subtrop. Agroecosystems* **2012**, *15* (SUPPL. 1).

(6) Joo, S. H.; Liang, Y.; Kim, M.; Byun, J.; Choi, H. Microplastics with Adsorbed Contaminants: Mechanisms and Treatment. *Environ. Challenges* **2021**, *3*, 100042. https://doi.org/10.1016/j.envc.2021.100042.

(7) Gebru, K. A.; Das, C. Removal of Bovine Serum Albumin from Wastewater Using Fouling Resistant Ultrafiltration Membranes Based on the Blends of Cellulose Acetate, and PVP-TiO_2 Nanoparticles. *J. Environ. Manage.* **2017**, *200*, 283–294. https://doi.org/10.1016/j.jenvman.2017.05.086.

(8) Rogers, J. A.; Metz, L.; Yong, V. W. Review: Endocrine Disrupting Chemicals and Immune Responses: A Focus on Bisphenol-A and Its Potential Mechanisms. *Mol. Immunol.* **2013**, *53* (4), 421–430. https://doi.org/10.1016/j.molimm.2012.09.013.

(9) Maji, S. K.; Pal, A.; Pal, T. Arsenic Removal from Real-Life Groundwater by Adsorption on Laterite Soil. *J. Hazard. Mater.* **2008**, *151* (2–3), 811–820. https://doi.org/10.1016/j.jhazmat.2007.06.060.

(10) Gupta, A. K.; Pal, A.; Sahoo, C. Photocatalytic Degradation of a Mixture of Crystal Violet (Basic Violet 3) and Methyl Red Dye in Aqueous Suspensions Using Ag^+ Doped TiO_2. *Dye. Pigment.* **2006**, *69* (3), 224–232. https://doi.org/10.1016/j.dyepig.2005.04.001.

(11) Kaneco, S.; Rahman, M. A.; Suzuki, T.; Katsumata, H.; Ohta, K. Optimization of Solar Photocatalytic Degradation Conditions of Bisphenol A in Water Using Titanium Dioxide. *J. Photochem. Photobiol. A Chem.* **2004**, *163* (3), 419–424. https://doi.org/10.1016/j.jphotochem.2004.01.012.

(12) Jodeh, S.; Abdelwahab, F.; Jaradat, N.; Warad, I.; Jodeh, W. Adsorption of Diclofenac from Aqueous Solution Using Cyclamen Persicum Tubers Based Activated Carbon (CTAC). *J. Assoc. Arab Univ. Basic Appl. Sci.* **2016**, *20* (1), 32–38. https://doi.org/10.1016/j.jaubas.2014.11.002.

(13) Zhou, Q.; Wang, Y.; Xiao, J.; Fan, H. Adsorption and Removal of Bisphenol A, α-Naphthol and β-Naphthol from Aqueous Solution by Fe_3O_4@polyaniline Core-Shell Nanomaterials. *Synth. Met.* **2016**, *212*, 113–122. https://doi.org/10.1016/j.synthmet.2015.12.008.

(14) Wolfand, J. M.; Lefevre, G. H.; Luthy, R. G. Metabolization and Degradation Kinetics of the Urban-Use Pesticide Fipronil by White Rot Fungus: Trametes Versicolor. *Environ. Sci. Process. Impacts* **2016**, *18* (10), 1256–1265. https://doi.org/10.1039/c6em00344c.

(15) Li, T.; Lu, M.; Gao, Y.; Huang, X.; Liu, G.; Xu, D. Double Layer MOFs M-ZIF-8@ZIF-67: The Adsorption Capacity and Removal Mechanism of Fipronil and Its Metabolites from Environmental Water and Cucumber Samples. *J. Adv. Res.* **2020**, *24*, 159–166. https://doi.org/10.1016/j.jare.2020.03.013.

(16) Soltani, N.; Saion, E.; Hussein, M. Z.; Erfani, M.; Abedini, A.; Bahmanrokh, G.; Navasery, M.; Vaziri, P. Visible Light-Induced Degradation of Methylene Blue in the Presence of Photocatalytic ZnS and CdS Nanoparticles. *Int. J. Mol. Sci.* **2012**, *13* (10), 12242–12258. https://doi.org/10.3390/ijms131012242.

(17) Tan, W. F.; Yu, Y. T.; Wang, M. X.; Liu, F.; Koopal, L. K. Shape Evolution Synthesis of Monodisperse Spherical, Ellipsoidal, and Elongated Hematite (α-Fe_2O_3) Nanoparticles

Using Ascorbic Acid. *Cryst. Growth Des.* **2014**, *14* (1), 157–164. https://doi.org/10.1021/cg401334d.

(18) Zhang, J.; Xu, L. J.; Zhu, Z. Q.; Liu, Q. J. Synthesis and Properties of (Yb, N)-TiO_2 Photocatalyst for Degradation of Methylene Blue (MB) under Visible Light Irradiation. *Mater. Res. Bull.* **2015**, *70*, 358–364. https://doi.org/10.1016/j.materresbull.2015.04.060.

(19) Sun, C.; He, P.; Pan, G.; Miao, Y.; Zhang, T.; Zhang, L. Study on Preparation and Visible-Light Activity of Ag–TiO_2 Supported by Artificial Zeolite. *Res. Chem. Intermed.* **2018**, *44* (4), 2607–2620. https://doi.org/10.1007/s11164-017-3249-0.

(20) Zhang, J. J.; Liu, X.; Ye, T.; Zheng, G. P.; Zheng, X. C.; Liu, P.; Guan, X. X. Novel Assembly of Homogeneous Reduced Graphene Oxide-Doped Mesoporous TiO_2 hybrids for Elimination of Rhodamine-B Dye under Visible Light Irradiation. *J. Alloys Compd.* **2017**, *698*, 819–827. https://doi.org/10.1016/j.jallcom.2016.12.279.

(21) Dong, G.; Zhang, L. Porous Structure Dependent Photoreactivity of Graphitic Carbon Nitride under Visible Light. *J. Mater. Chem.* **2012**, *22* (3), 1160–1166. https://doi.org/10.1039/c1jm14312c.

(22) Monga, D.; Basu, S. Enhanced Photocatalytic Degradation of Industrial Dye by g-C_3N_4/TiO_2 Nanocomposite: Role of Shape of TiO_2. *Adv. Powder Technol.* **2019**, *30* (5), 1089–1098. https://doi.org/10.1016/j.apt.2019.03.004.

(23) Du, G.; Feng, P.; Cheng, X.; Li, J.; Luo, X. Immobilizing of ZIF-8 Derived ZnO with Controllable Morphologies on Zeolite A for Efficient Photocatalysis. *J. Solid State Chem.* **2017**, *255*, 215–218. https://doi.org/10.1016/j.jssc.2017.07.035.

(24) Nasseh, N.; Arghavan, F. S.; Rodriguez-Couto, S.; Hossein Panahi, A.; Esmati, M.; A-Musawi, T. J. Preparation of Activated Carbon@ZnO Composite and Its Application as a Novel Catalyst in Catalytic Ozonation Process for Metronidazole Degradation. *Adv. Powder Technol.* **2020**, *31* (2), 875–885. https://doi.org/10.1016/j.apt.2019.12.006.

(25) Martins, P. M.; Salazar, H.; Aoudjit, L.; Gonçalves, R.; Zioui, D.; Fidalgo-Marijuan, A.; Costa, C. M.; Ferdov, S.; Lanceros-Mendez, S. Crystal Morphology Control of Synthetic Giniite for Enhanced Photo-Fenton Activity against the Emerging Pollutant Metronidazole. *Chemosphere* **2021**, *262*, 128300. https://doi.org/10.1016/j.chemosphere.2020.128300.

(26) El Bouraie, M. M.; Ibrahim, S. S. Comparative Study Between Metronidazole Residues Disposal by Using Adsorption and Photodegradation Processes onto MgO Nanoparticles. *J. Inorg. Organomet. Polym. Mater.* **2021**, *31* (1), 344–364. https://doi.org/10.1007/s10904-020-01711-6.

(27) Gebru, K. A.; Das, C. Removal of Pb (II) and Cu (II) Ions from Wastewater Using Composite Electrospun Cellulose Acetate/Titanium Oxide (TiO_2) Adsorbent. *J. Water Process Eng.* **2017**, *16*, 1–13. https://doi.org/10.1016/j.jwpe.2016.11.008.

(28) Rao, U.; Su, Y.; Khor, C. M.; Jung, B.; Ma, S.; Cwiertny, D. M.; Wong, B. M.; Jassby, D.

Structural Dependence of Reductive Defluorination of Linear PFAS Compounds in a UV/Electrochemical System. *Environ. Sci. Technol.* **2020**, *54* (17), 10668–10677. https://doi.org/10.1021/acs.est.0c02773.

(29) Sakthikumar, K.; Ede, S. R.; Mishra, S.; Kundu, S. Shape-Selective Synthesis of $Sn(MoO_4)_2$ Nanomaterials for Catalysis and Supercapacitor Applications. *Dalt. Trans.* **2016**, *45* (21), 8897–8915. https://doi.org/10.1039/c6dt00208k.

(30) Wang, S.; Peng, Y. Natural Zeolites as Effective Adsorbents in Water and Wastewater Treatment. *Chem. Eng. J.* **2010**, *156* (1), 11–24. https://doi.org/10.1016/j.cej.2009.10.029.

(31) Velaga, B.; Doley, R.; Peela, N. R. Rapid Synthesis of Hierarchical ZSM-5 Zeolites for the Reactions Involving Larger Reactant Molecules. *Adv. Powder Technol.* **2021**, *32* (4), 1033–1046. https://doi.org/10.1016/j.apt.2021.02.002.

(32) Lima, C. G. S.; Jorge, E. Y. C.; Batinga, L. G. S.; Lima, T. de M.; Paixão, M. W. ZSM-5 Zeolite as a Promising Catalyst for the Preparation and Upgrading of Lignocellulosic Biomass-Derived Chemicals. *Curr. Opin. Green Sustain. Chem.* **2019**, *15*, 13–19. https://doi.org/10.1016/j.cogsc.2018.08.001.

(33) Ali, I.; Hassan, A.; Shabaan, S.; El-Nasser, K. Synthesis and Characterization of Composite Catalysts Cr/ZSM-5 and Their Effects toward Photocatalytic Degradation of p-Nitrophenol. *Arab. J. Chem.* **2017**, *10*, S2106–S2114. https://doi.org/10.1016/j.arabjc.2013.07.042.

(34) Guo, Y.; Zhang, H.; Liu, Y. Desorption Characteristics and Kinetic Parameters Determination of Molecular Sieve by Thermogravimetric Analysis/Differential Thermogravimetric Analysis Technique. *Adsorpt. Sci. Technol.* **2018**, *36* (7–8), 1389–1404. https://doi.org/10.1177/0263617418772665.

(35) Mohammadzadeh Kakhki, R.; Karimian, A.; Hasan-nejad, H.; Ahsani, F. Zinc Oxide–Nanoclinoptilolite as a Superior Catalyst for Visible Photo-Oxidation of Dyes and Green Synthesis of Pyrazole Derivatives. *J. Inorg. Organomet. Polym. Mater.* **2019**, *29* (4), 1358–1367. https://doi.org/10.1007/s10904-019-01100-8.

(36) Smith, K.; El-Hiti, G. A. Use of Zeolites for Greener and More Para-Selective Electrophilic Aromatic Substitution Reactions. *Green Chem.* **2011**, *13* (7), 1579. https://doi.org/10.1039/c0gc00689k.

(37) Maksod, I. H. A. El; Al-Shehri, A.; Bawaked, S.; Mokhtar, M.; Narasimharao, K. Structural and Photocatalytic Properties of Precious Metals Modified TiO_2-BEA Zeolite Composites. *Mol. Catal.* **2017**, *441*, 140–149. https://doi.org/10.1016/j.mcat.2017.08.012.

(38) Mafra, L.; Vidal-Moya, J. A.; Blasco, T. Structural Characterization of Zeolites by Advanced Solid State NMR Spectroscopic Methods. In *Annual Reports on NMR Spectroscopy*; 2012; Vol. 77, pp 259–351. https://doi.org/10.1016/B978-0-12-397020-6.00004-0.

(39) Jiang, N.; Shang, R.; Heijman, S. G. J.; Rietveld, L. C. High-Silica Zeolites for

Adsorption of Organic Micro-Pollutants in Water Treatment: A Review. *Water Res.* **2018**, *144*, 145–161. https://doi.org/10.1016/j.watres.2018.07.017.

(40) Chibani, S.; Chebbi, M.; Lebègue, S.; Bučko, T.; Badawi, M. A DFT Investigation of the Adsorption of Iodine Compounds and Water in H-, Na-, Ag-, and Cu- Mordenite. *J. Chem. Phys.* **2016**, *144* (24), 244705. https://doi.org/10.1063/1.4954659.

(41) Nenoff, T. M.; Rodriguez, M. A.; Soelberg, N. R.; Chapman, K. W. Silver-Mordenite for Radiologic Gas Capture from Complex Streams: Dual Catalytic CH_3I Decomposition and I Confinement. *Microporous Mesoporous Mater.* **2014**, *200*, 297–303. https://doi.org/10.1016/j.micromeso.2014.04.041.

(42) Zhang, W.; Yang, J.; Pei, X. Enhanced Photocatalytic Activity of In-TiO_2 Supported on HZSM-5 Zeolite. *Optoelectron. Adv. Mater. Rapid Commun.* **2018**, *12* (3–4), 227–230.

(43) Rajabi, S. K.; Sohrabnezhad, S. Synthesis and Characterization of Magnetic Core with Two Shells: Mordenite Zeolite and CuO to Form Fe_3O_4@MOR@CuO Core-Shell: As a Visible Light Driven Photocatalyst. *Microporous Mesoporous Mater.* **2017**, *242*, 136–143. https://doi.org/10.1016/j.micromeso.2017.01.024.

(44) Moosavifar, M.; Bagheri, S. Photocatalytic Performance of $H_6P_2W_{18}O_{62}/TiO_2$ Nanocomposite Encapsulated into Beta Zeolite under UV Irradiation in the Degradation of Methyl Orange. *Photochem. Photobiol.* **2019**, *95* (2), 532–542. https://doi.org/10.1111/php.13015.

(45) Asadollahi, A.; Sohrabnezhad, S.; Ansari, R. Enhancement of Photocatalytic Activity and Stability of Ag_2CO_3 by Formation of AgBr/Ag_2CO_3 Heterojunction in Mordenite Zeolite. *Adv. Powder Technol.* **2017**, *28* (1), 304–313. https://doi.org/10.1016/j.apt.2016.10.004.

(46) Yang, L.; Zhao, Y.; Liu, Y.; Zhang, W. Sol–Gel Synthesis of B-TiO_2(20%)/HZSM-5 Composite Photocatalyst for Azophloxine Degradation. *J. Sol-Gel Sci. Technol.* **2020**, *93* (2), 371–379. https://doi.org/10.1007/s10971-019-05153-6.

(47) Vaez, Z.; Javanbakht, V. Synthesis, Characterization and Photocatalytic Activity of ZSM-5/ZnO Nanocomposite Modified by Ag Nanoparticles for Methyl Orange Degradation. *J. Photochem. Photobiol. A Chem.* **2020**, *388*, 112064. https://doi.org/10.1016/j.jphotochem.2019.112064.

(48) Anusha, J. V.; Nambi, A. B.; Subramanian, E. In Situ and Ex Situ Immobilization of Nano Gold Particles in Zeolite Framework and a Comparison of Their Photocatalytic Activities. *J. Inorg. Organomet. Polym. Mater.* **2018**, *28* (1), 15–26. https://doi.org/10.1007/s10904-017-0753-z.

(49) Gomez, S.; Marchena, C. L.; Renzini, M. S.; Pizzio, L.; Pierella, L. In Situ Generated TiO_2 over Zeolitic Supports as Reusable Photocatalysts for the Degradation of Dichlorvos. *Appl. Catal. B Environ.* **2015**, *162*, 167–173. https://doi.org/10.1016/j.apcatb.2014.06.047.

(50) Latha, P.; Karuthapandian, S. Novel, Facile and Swift Technique for Synthesis of CeO_2 Nanocubes Immobilized on Zeolite for Removal of CR and MO Dye. *J. Clust. Sci.* **2017**,

28 (6), 3265–3280. https://doi.org/10.1007/s10876-017-1292-z.

(51) Nyankson, E.; Adjasoo, J.; Efavi, J. K.; Yaya, A.; Manu, G.; Kingsford, A.; Abrokwah, R. Y. Synthesis and Kinetic Adsorption Characteristics of Zeolite/CeO_2 Nanocomposite. *Sci. African* **2020**, *7*, e00257. https://doi.org/10.1016/j.sciaf.2019.e00257.

(52) Padervand, M.; Heidarpour, H.; Bargahi, A. A Mechanistic Study and In-Vivo Toxicity Bioassay on Acetamiprid Photodegradation over the Zeolite Supported Cerium-Based Photocatalyst. *J. Photochem. Photobiol. A Chem.* **2020**, *395*, 112526. https://doi.org/10.1016/j.jphotochem.2020.112526.

(53) Heidari, S.; Haghighi, M.; Shabani, M. Ultrasound Assisted Dispersion of $Bi_2Sn_2O_7$-C_3N_4 Nanophotocatalyst over Various Amount of Zeolite Y for Enhanced Solar-Light Photocatalytic Degradation of Tetracycline in Aqueous Solution. *Ultrason. Sonochem.* **2018**, *43*, 61–72. https://doi.org/10.1016/j.ultsonch.2018.01.001.

(54) Qi, L.; Tang, C.; Zhang, L.; Yao, X.; Cao, Y.; Liu, L.; Gao, F.; Dong, L.; Chen, Y. Influence of Cerium Modification Methods on Catalytic Performance of Au/Mordenite Catalysts in CO Oxidation. *Appl. Catal. B Environ.* **2012**, *127*, 234–245. https://doi.org/10.1016/j.apcatb.2012.08.013.

(55) Janoš, P.; Henych, J.; Pfeifer, J.; Zemanová, N.; Pilařová, V.; Milde, D.; Opletal, T.; Tolasz, J.; Malý, M.; Štengl, V. Nanocrystalline Cerium Oxide Prepared from a Carbonate Precursor and Its Ability to Breakdown Biologically Relevant Organophosphates. *Environ. Sci. Nano* **2017**, *4* (6), 1283–1293. https://doi.org/10.1039/c7en00119c.

(56) Niu, J.; Jia, X.; Zhao, Y.; Liu, Y.; Zhong, W.; Zhai, Z.; Li, Z. Adsorbing Low Concentrations of Cr(VI) onto CeO_2@ZSM-5 and the Adsorption Kinetics, Isotherms and Thermodynamics. *Water Sci. Technol.* **2018**, *77* (9), 2327–2340. https://doi.org/10.2166/wst.2018.157.

(57) Tokunaga, S.; Haron, M. J.; Wasay, S. A.; Uchiumi, A.; Wong, K. F.; Laosangthum, K. Removal of Fluoride Ions from Aqueous Solutions by Multivalent Metal Compounds. *Int. J. Environ. Stud.* **1995**, *48* (1), 17–28. https://doi.org/10.1080/00207239508710973.

(58) Janoš, P.; Henych, J.; Pelant, O.; Pilařová, V.; Vrtoch, L.; Kormunda, M.; Mazanec, K.; Štengl, V. Cerium Oxide for the Destruction of Chemical Warfare Agents: A Comparison of Synthetic Routes. *J. Hazard. Mater.* **2016**, *304*, 259–268. https://doi.org/10.1016/j.jhazmat.2015.10.069.

(59) Wang, X.; Maeda, K.; Thomas, A.; Takanabe, K.; Xin, G.; Carlsson, J. M.; Domen, K.; Antonietti, M. A Metal-Free Polymeric Photocatalyst for Hydrogen Production from Water under Visible Light. *Nat. Mater.* **2009**, *8* (1), 76–80. https://doi.org/10.1038/nmat2317.

(60) Lin, J.; Tian, W.; Zhang, H.; Duan, X.; Sun, H.; Wang, S. Graphitic Carbon Nitride-Based Z-Scheme Structure for Photocatalytic CO_2 Reduction. *Energy and Fuels* **2021**, *35* (1), 7–24. https://doi.org/10.1021/acs.energyfuels.0c03048.

(61) Mousavi, M.; Habibi-Yangjeh, A. Magnetically Recoverable Highly Efficient Visible-Light-Active g-C_3N_4/Fe_3O_4/Ag_2WO_4/AgBr Nanocomposites for Photocatalytic Degradations of Environmental Pollutants. *Adv. Powder Technol.* **2018**, *29* (1), 94–105. https://doi.org/10.1016/j.apt.2017.10.016.

(62) Mousavi, M.; Habibi-Yangjeh, A.; Pouran, S. R. Review on Magnetically Separable Graphitic Carbon Nitride-Based Nanocomposites as Promising Visible-Light-Driven Photocatalysts. *J. Mater. Sci. Mater. Electron.* **2018**, *29* (3), 1719–1747. https://doi.org/10.1007/s10854-017-8166-x.

(63) Mishra, A.; Mehta, A.; Kainth, S.; Basu, S. Effect of g-C_3N_4 Loading on TiO_2/Bentonite Nanocomposites for Efficient Heterogeneous Photocatalytic Degradation of Industrial Dye under Visible Light. *J. Alloys Compd.* **2018**, *764*, 406–415. https://doi.org/10.1016/j.jallcom.2018.06.089.

(64) Wang, Y.; Di, Y.; Antonietti, M.; Li, H.; Chen, X.; Wang, X. Excellent Visible-Light Photocatalysis of Fluorinated Polymeric Carbon Nitride Solids. *Chem. Mater.* **2010**, *22* (18), 5119–5121. https://doi.org/10.1021/cm1019102.

(65) Wang, Y.; Li, H.; Yao, J.; Wang, X.; Antonietti, M. Synthesis of Boron Doped Polymeric Carbon Nitride Solids and Their Use as Metal-Free Catalysts for Aliphatic C-H Bond Oxidation. *Chem. Sci.* **2011**, *2* (3), 446–450. https://doi.org/10.1039/c0sc00475h.

(66) Jiang, D.; Yu, H.; Yu, H. Modified g-C_3N_4/TiO_2 Nanosheets/ZnO Ternary Facet Coupled Heterojunction for Photocatalytic Degradation of p-Toluenesulfonic Acid (p-TSA) under Visible Light. *Phys. E Low-Dimensional Syst. Nanostructures* **2017**, *85*, 1–6. https://doi.org/10.1016/j.physe.2016.08.014.

(67) Mishra, A.; Mehta, A.; Basu, S. Clay Supported TiO_2 Nanoparticles for Photocatalytic Degradation of Environmental Pollutants: A Review. *J. Environ. Chem. Eng.* **2018**, *6* (5), 6088–6107. https://doi.org/10.1016/j.jece.2018.09.029.

(68) Mu, Y.; Wang, N.; Sun, Z.; Wang, J.; Li, J.; Yu, J. Carbogenic Nanodots Derived from Organo-Templated Zeolites with Modulated Full-Color Luminescence. *Chem. Sci.* **2016**, *7* (6), 3564–3568. https://doi.org/10.1039/c6sc00085a.

(69) Liu, J.; Wang, N.; Yu, Y.; Yan, Y.; Zhang, H.; Li, J.; Yu, J. Carbon Dots in Zeolites: A New Class of Thermally Activated Delayed Fluorescence Materials with Ultralong Lifetimes. *Sci. Adv.* **2017**, *3* (5), e1603171. https://doi.org/10.1126/sciadv.1603171.

(70) Anantharaj, S.; Valappil, M. O.; Karthick, K.; Pillai, V. K.; Alwarappan, S.; Kundu, S. Electrochemically Chopped WS_2 Quantum Dots as an Efficient and Stable Electrocatalyst for Water Reduction. *Catal. Sci. Technol.* **2019**, *9* (1), 223–231. https://doi.org/10.1039/c8cy02168f.

(71) Sohal, N.; Maity, B.; Basu, S. Carbon Dot-MnO_2 Nanosphere Composite Sensors for Selective Detection of Glutathione. *ACS Appl. Nano Mater.* **2020**, *3* (6), 5955–5964. https://doi.org/10.1021/acsanm.0c01088.

(72) Wang, Y.; Shi, R.; Lin, J.; Zhu, Y. Enhancement of Photocurrent and Photocatalytic Activity of ZnO Hybridized with Graphite-like C_3N_4. *Energy Environ. Sci.* **2011**, *4* (8), 2922. https://doi.org/10.1039/c0ee00825g.

(73) Pirsaheb, M.; Asadi, A.; Sillanpää, M.; Farhadian, N. Application of Carbon Quantum Dots to Increase the Activity of Conventional Photocatalysts: A Systematic Review. *J. Mol. Liq.* **2018**, *271*, 857–871. https://doi.org/10.1016/j.molliq.2018.09.064.

(74) Di, J.; Xia, J.; Ge, Y.; Li, H.; Ji, H.; Xu, H.; Zhang, Q.; Li, H.; Li, M. Novel Visible-Light-Driven CQDs/Bi_2WO_6 Hybrid Materials with Enhanced Photocatalytic Activity toward Organic Pollutants Degradation and Mechanism Insight. *Appl. Catal. B Environ.* **2015**, *168–169*, 51–61. https://doi.org/10.1016/j.apcatb.2014.11.057.

(75) Yu, H.; Shi, R.; Zhao, Y.; Waterhouse, G. I. N.; Wu, L.-Z.; Tung, C.-H.; Zhang, T. Smart Utilization of Carbon Dots in Semiconductor Photocatalysis. *Adv. Mater.* **2016**, *28* (43), 9454–9477. https://doi.org/10.1002/adma.201602581.

(76) Li, H.; Shi, W.; Huang, W.; Yao, E. P.; Han, J.; Chen, Z.; Liu, S.; Shen, Y.; Wang, M.; Yang, Y. Carbon Quantum Dots/TiOx Electron Transport Layer Boosts Efficiency of Planar Heterojunction Perovskite Solar Cells to 19%. *Nano Lett.* **2017**, *17* (4), 2328–2335. https://doi.org/10.1021/acs.nanolett.6b05177.

(77) Jiang, K.; Zhang, L.; Lu, J.; Xu, C.; Cai, C.; Lin, H. Triple-Mode Emission of Carbon Dots: Applications for Advanced Anti-Counterfeiting. *Angew. Chemie - Int. Ed.* **2016**, *55* (25), 7231–7235. https://doi.org/10.1002/anie.201602445.

(78) Dong, X.; Wei, L.; Su, Y.; Li, Z.; Geng, H.; Yang, C.; Zhang, Y. Efficient Long Lifetime Room Temperature Phosphorescence of Carbon Dots in a Potash Alum Matrix. *J. Mater. Chem. C* **2015**, *3* (12), 2798–2801. https://doi.org/10.1039/c5tc00126a.

(79) Tan, J.; Zou, R.; Zhang, J.; Li, W.; Zhang, L.; Yue, D. Large-Scale Synthesis of N-Doped Carbon Quantum Dots and Their Phosphorescence Properties in a Polyurethane Matrix. *Nanoscale* **2016**, *8* (8), 4742–4747. https://doi.org/10.1039/c5nr08516k.

(80) Samadi-Maybodi, A.; Sadeghi-Maleki, M. R. Preparation of Mesoporous SBA-15 Supported CdS Quantum Dots and Its Application for Photocatalytic Degradation of Organic Pollutants in Aqueous Media. *J. Inorg. Organomet. Polym. Mater.* **2018**, *28* (6), 2620–2632. https://doi.org/10.1007/s10904-018-0918-4.

Chapter 3: Experimental Methods, Kinetics and Isotherm Models

This chapter discusses about the chemicals used for the synthesis/modification of zeolite composite materials and the characterization methods used for the analysis of prepared nano-composite materials. The various characterization like N_2 adsorption-desorption analysis, X-ray diffraction analysis (XRD), Scanning electron microscopy (SEM), High-Resolution Transmission electron microscopy (HRTEM), Energy-dispersive X-ray spectroscopy analysis (EDX), X-ray photoelectron spectroscopy (XPS) were elaborated along with their methods. The adsorption study data were further analyzed with the help of adsorption isotherms and the interactions between the adsorbate and adsorbent can also be predicted by plotting the data in the Langmuir, Freundlich, Harkins-Jura, Dubbin-Radushkevich (D-R), and Halsey adsorption isotherm models. Different kinetic models such as Pseudo-first order, Pseudo-second order, Elovich model, and intra-particle diffusion were also investigated. Based on R^2 (Pearson correlation coefficient) values their accuracies were estimated. A thermodynamics study was carried out to know the enthalpy and entropy of performed adsorption process.

3.1 Materials

Ammonium ZSM-5 zeolite, ammonium mordenite, and ammonium beta zeolite were purchased from Thermo Fisher Scientific India Pvt. Ltd. and 13X zeolite from Allied Products Private Limited. The NH_4NO_3 salt was obtained from Loba Chemie. Ceric ammonium nitrate (99% pure) salt was procured from CDH chemicals, India. The melamine was purchased from S D Fine-Chem Limited, Industrial Estate, Mumbai. Catechol was obtained from SD Fine-Chem Limited and HPLC grade solvents were used for synthesizing photocatalyst. Raw wastewater was acquired from the industry, Ludhiana. The Methylene Blue (MB) dye and insecticide Fipronil (5% w/w) were bought from Merck and Bayer Crop Science, respectively. Metronidazole antibiotic from Flagyl brand was procured from the pharmaceutical industry, HP India.

3.2 Characterization

3.2.1 Brunauer–Emmett–Teller

The BET (Brunauer–Emmett–Teller) surface area and pore distribution of the zeolites and modified zeolites were analyzed with the help of the BET surface area analyzer instrument. The Microtrac BELSORP MINI-II (Bel, Japan) instrument was used to find out BET surface area, mean pore diameter, and volume of pores, and BJH (Barrett–Joyner–Halenda) plot for pore-size distribution of all adsorbents through N_2 adsorption-desorption isotherms at 77 K. The BET specific surface area was obtained with the help of experimental points at a relative pressure of $P/P_0 \leq 0.5$. The total volume of pores of various adsorbents was determined by the amount of nitrogen adsorbed (at $P/P_0 = 0.99$).

3.2.2 X-ray diffraction

The chemical structure and crystallinity of the synthesized nano-zeolites were analyzed by the X-ray diffraction (XRD) technique. The Pan Analytical X′ Pert-Pro X-ray diffractometer was adopted to study the XRD patterns of unmodified and modified zeolites, with Ni-filtered CuK_α radiation having a step size of 0.013° (45 kV, 40 mA) and wavelength $\lambda = 1.5406$ Å. The XRD analysis was done at a slow scan from a 2Θ range of $5–80^\circ$.

3.2.3 Energy Dispersive X-Ray Spectroscopy

Energy Dispersive X-Ray Spectroscopy (EDX or EDS) was used to analyze the elemental composition, color mapping, and surface morphology in combination with scanning electron microscopy. The EDS along with elemental maps were used to determine chemical compositions by both qualitatively and quantitatively using JEOL JSM-6510 with a voltage of 15 kV.

3.2.4 High-resolution transmission electron microscopy

The HR-TEM analysis was done with instrument specification: Thermofisher (TALOS F200S G2) - 200 KV, FEG, CMOS Camera 4 K x 4 K, In Column EDS Detector. The sample was homogenized in an ultrasonic bath for 30 min. The pores location, alignment of particles, surface morphology, d-spacing, planes, and size of adsorbent/loaded material were observed by HR-TEM analysis.

3.2.5 X-ray photoelectron spectroscopy

The chemical states of metal oxide and carbon-based photoactive materials were investigated by XPS (X-ray Photoelectron Spectroscopy, Omicron ESCA instrument) employed for characterization with a monochromatic Al kα radiation (hν ~1486.7 eV).

3.2.6 Gas Chromatography-Mass Spectrometry

Gas Chromatography-Mass Spectrometry (GC–MS) analysis was carried out to analyze the intermediates of the photodegradation process. The Thermo Scientific TSQ 8000 triple quadrupole MS was coupled with Thermo Trace 1300 GC was used. The helium gas was used as a carrier gas with a flow rate of 1 mL/min. The splitless injector mode with BP 5MS column having dimensions of 30 *m* ×0.25 mm; 0.s25 μm along with the column makeup of 5% phenyl polysilphenylene-siloxane was used. The injection volume was 1 μL with injector temperature (250 °C), ion source temp. (230 °C), MS transfer line temp. (240 °C) was implied. Initially, the temperature of the oven was set to 50°C (hold time:1 min) with an increasing rate of 10°C/min to reach 150°C (hold time:1 min). Then its temperature was increased from 250 °C (hold time:1 min) to 280 °C (hold time:5 min) at an increasing rate of 8°C/min and 15°C/min. The MS spectra were obtained from range m/z (40-650) with 3525 scans and Xcalibur 2.2SP1 with foundation 2.0SP1 software was used.

3.3 Performance evaluation of adsorbents/photocatalysts

3.3.1 Batch adsorption experiments

The stock solution of FIP (600 ppm) was prepared by dissolving FIP in deionized water. The modification with cerium oxide was done to improve the surface properties or charge to facilitate the adsorption. Adsorption of FIP on modified zeolite was carried out in a flask (250 ml) in batch mode over a certain amount of adsorbent (0.5-4 g/L). In order to obtain maximum removal of FIP from aqueous solution, the EDC solution with adsorbent was shaken by an incubator shaker (Bionics, BST-AS35) with varying agitation speed (50-300 rpm) at the temperature range from 25°C - 45 °C for a specific time period (0-140 min). The samples were withdrawn from the shaker at fixed time intervals, and the adsorbent was separated from the solution by centrifugation at 8,000 rpm for 5 min in a centrifuge machine (TG-16S, Benchtop). After this, the supernatants were analyzed by UV–visible spectrophotometer (HACH, DR 5000) to determine the residual concentrations of FIP (at 276 nm) by using a standard curve.[1] The removal efficiency of FIP (R%) and adsorption capacity of Cerium modified zeolites (q_t, mg/g) were calculated using **Equations 3.1 and 3.2** respectively.

Removal efficiency, R (%) = $(\frac{Ci-Cf}{Ci}) \times 100$ (3.1)

Adsorption capacity, $q_t = \frac{C_i - C_f}{m}$ (3.2)

Where C_i is the initial and C_f is the final concentration of the adsorbate; m is the mass of the adsorbent per litre of the solution, and q_t (mg/g) is the amount of the solute adsorbed per gram of the adsorbent at time t. All batch experiments were carried out in triplicate and the average values were accounted. The standard deviation of the data for various repetitions was less than 5%.

3.3.2 Adsorption kinetics study

To explore the adsorption process a variety of kinetic models like pseudo-first-order, pseudo-second-order[2] and Elovich models were tried for fitting the kinetic records.[3]

Lagergren's Pseudo-first-order model:

$$\log(Q_e - Q_t) = \log(Q_e) - \frac{K_1}{2.303} \times t \quad (3.3)$$

Linear expression for Pseudo-second-order model:

$$\frac{t}{Q_t} = \frac{1}{K_2 Q_e^2} + \frac{t}{Q_e} \quad (3.4)$$

Elovich kinetic model:

$$q_t = \frac{1}{B}\ln(ab) + \frac{1}{B}\ln(t) \quad (3.5)$$

Lagergren's pseudo-first-order model (**Equation 3.3**) is generally employed to primary rate with the assumption that the adsorption rate is associated with the measure of unoccupied adsorption sites.[4] The rate constant K_1 (L/min) was determined by the slope value of the graph of log(Q_e-Q_t) versus time.[4] The rate constant of pseudo-second-order (**Equation 3.4**) model K_2 (g/mg.min) was obtained by plotting the graph between t/Qt and t.[5] For explaining more accurately the heterogeneous nature of the Ce-modified zeolite and its energetic surface, Elovich kinetic model (**Equation 3.5**) was used. The rate of initial adsorption was determined from the graph of Q_t versus ln t.[6] The various kinetic parameters were calculated to know the favorable kinetic model for the adsorption process.

3.3.3 Adsorption isotherms

Adsorption isotherms reveal the efficacy of the Ce-zeolite and their binding efficiency towards FIP molecules which is a significant factor for the adsorption procedure to occur. The binding affinity in the form of adsorption capacity is obtained by fitting the data in various isotherms like Langmuir,[7] Freundlich, Temkin, Harkins-Jura, Halsey, and Dubbin-Radushkevich;[2,5,8,9] their linear expressions were depicted in equations given below and parameters were elaborated. The accurateness of these adsorption isotherms was being determined through R^2 values (Pearson correlation coefficient).

Langmuir isotherm

$$\frac{C_e}{q_e} = \frac{1}{Q_m K_L} + \frac{1}{Q_m} C_e \tag{3.6}$$

$$R_L = \frac{1}{1 + K_L C_0} \tag{3.7}$$

Freundlich isotherm

$$\log q_e = \log K_f + \frac{\log C_e}{\mathrm{n}} \tag{3.8}$$

Temkin isotherm

$$q_e = B_T \ln K_T + B_T \ln C_e \tag{3.9}$$

Harkins-Jura isotherm

$$\frac{1}{\mathrm{q_e^2}} = \left(\frac{\mathrm{B}}{\mathrm{A}}\right) - \frac{1}{\mathrm{A}} \log \mathrm{C_e} \tag{3.10}$$

Halsey isotherm

$$\ln \mathrm{q_e} = \frac{1}{\mathrm{n}} \ln \mathrm{K} - \frac{1}{\mathrm{n}} \ln \mathrm{C_e} \tag{3.11}$$

Dubinin–Radushkevich model

$$\ln \mathrm{q_e} = \ln \mathrm{Q_s} - \mathrm{B}\varepsilon^2 \tag{3.12}$$

$$\varepsilon = RT \ln\left(1 + \frac{1}{\mathrm{C_e}}\right) \tag{3.13}$$

$$E = \sqrt{1}/2\ B \tag{3.14}$$

Firstly, the data were fitted in Langmuir isotherm which presumed that there is single layer (monolayer) formation over the adsorbent, having a homogeneous surface with negligible interactions among the pollutant molecules and follows **Equation 3.6**. The maximum adsorption

capacity is denoted by 'Q_m' which indicates the maximum amount of pollutant adsorbed (in monolayer manner)/gram of the adsorbent (mg/g).[10] The adsorbent's activeness and its potency towards the binding channels are denoted by K_L (L/mg) and this K_L value can be used to find out separation factor (R_L) (**Equation 3.7**). The R_L value was determined for finding the characteristics and practicability of Langmuir isotherm. The unitless constant R_L value suggests that whether the adsorption is linear (R_L=1), irreversible (R_L>1), unfavorable (R_L>1) or favorable ($0 < R_L < 1$).[11]

The Freundlich isotherm (**Equation 3.8**) elucidates that the adsorption process occurs in a multilayer fashion on heterogeneous surfaces of the adsorbent. For favourable adsorption, the 'n' should be n>1, and specifically for a better sorption process, the value of Freundlich constant 1/n lies from 0 to 0.5. If the value of 1/n lies in the range of 0.5 to ≤ 1 suggesting difficulty in the adsorption process.[12,13]

Temkin isotherm (**Equation 3.9**) presumed that as linkages between adsorbate and adsorbent increases, the heat of adsorption decreases. The B_T is the heat of adsorption and expressed by formula $B_T = RT/\beta$; where 'β' denotes the maximum bond energy.[14] The Harkins-Jura isotherm reveals that there is heterogeneity in pore distribution which helps for the explanation of multilayer adsorption (**Equation 3.10**). Halsey isotherm (**Equation 3.11**) gives a proper explanation for the adsorption in multilayer fashion[6] and is used to describe hetero-porous solid adsorbent. The Dubinin–Radushkevich (D-R) model implies a hypothesis; no uniform surface is available for stable adsorption in conformity with Polanyi's potential theory. The linear form of D-R isotherm and Polanyi Potential is symbolized by 'ε' are written in **Equation 3.12 and 3.13**, respectively. The values of parameters B and Q_s were calculated from the plot of ln q_e and ε^2.[6] The mean adsorption energy 'E' was calculated from the B value by using **Equation 3.14**.[12,15]

3.3.4 Thermodynamic properties

Thermodynamic parameters, Δ*G*°-Gibbs free energy change with units kJ/mol, Δ*S*°-entropy change (kJ/mol.K), and Δ*H*°-enthalpy change with units (kJ/mol) were determined. To know the thermodynamic properties of the adsorption process in removing pollutant molecules by Ce-zeolite the Van't Hoff equation was used, as written below:[8]

$$\ln\left(\frac{q_e}{C_e}\right) = -\frac{\Delta H^\circ}{\mathrm{RT}} + \frac{\Delta S^\circ}{\mathrm{R}} \qquad (3.15)$$

$$K_c = 1000 \times \frac{q_e}{C_e} \quad (3.16)$$

$$\ln(K_c) = -\frac{\Delta H^\circ}{\mathrm{RT}} + \frac{\Delta S^\circ}{\mathrm{R}} \quad (3.17)$$

$$\Delta G^\circ = \Delta H^\circ - \mathrm{T}(\Delta S^\circ) \quad (3.18)$$

Here 'q_e' is the quantity of pollutant adsorbed per gram of the adsorbent with units mg/g, the equilibrium concentration of pollutant is denoted by 'C_e' with units mg/L, and the absolute temperature 'T' in Kelvin (K). The data of ΔH° and ΔS° were determined from the plot of $\ln(q_e/C_e)$ versus 1/T, following **Equation 3.15**.[4] The '*Kd*' distribution coefficient which equals to (q_e/C_e) is not appropriate for calculating the thermodynamic parameters. So, this '*Kd*' with units L/g was converted to K_c by multiplying it with the factor of 1000, which is dimensionless and appropriate for further calculations.[16] From **Equation 3.17**, the ΔG° values of FIP adsorption on Cerium modified zeolites were estimated for temperatures: 298K, 303K, 308K, 313K, and 318K.

3.3.5 Photocatalysis experiment

Appropriate amounts of the prepared photocatalysts were poured into the container having appropriate solution of pollutants of specific concentrations, were irradiated with various light sources (UV/sunlight/visible) after the attainment of equilibrium, and the treated solution was checked at different time intervals to know the kinetics and rate constants. After the photo-degradation experiment, the treated pollutants were separated from the catalyst via the centrifugation process. The absorbance values of the treated pollutants were observed from UV-Visible spectrophotometer (HACH DR 5000) at their λ_{max} values. According to Beer Lambert's law, the concentration is directly proportional to absorbance value; therefore the degradation efficiency can be calculated by the formula:

$$\% \text{ Degradation} = \{(C_0 - C)/ C_0\} \times 100 = \{(A_0 - A)/ A_0\} \times 100 \quad (3.19)$$

Where A_0, A, and C_0, C represents the absorbance and concentration at time t = 0 and t, respectively. The rate constant of the photodegradation experiment was calculated by the equation:

$$\ln (C/C_0) = -kt \quad (3.20)$$

Where k is the rate constant, C_0 and C is the concentration of the pollutant (dye or pesticide) at time 't' = 0 and t, respectively.

3.3.5.1 Photocatalytic degradation

The photocatalytic degradation was tracked so vastly by the wastewater treatment as it was proved to be the proficient and effective technique for the elimination of the noxious contaminants from the wastewater for the cleanliness rationales. This wastewater quantity has been increased bit by bit due to the industrialization and modernization of society.[17,18] As already mentioned in the above section, natural sunlight can also be used for degradation experiments because it is an eco-friendly energy source and satiates the energy necessity without harming our environment. So this technique fits in the cost effectual and safer category. For the photocatalytic degradation mechanism, these key points are followed: (a) movement of pollutant molecules present in reaction solution to the surface of the catalyst, (b) pollutant's adsorption, (c) photocatalysis in the adsorbed state, (d) desorption of the degraded products; and (f) detachment of the final products from the border.[19,20]

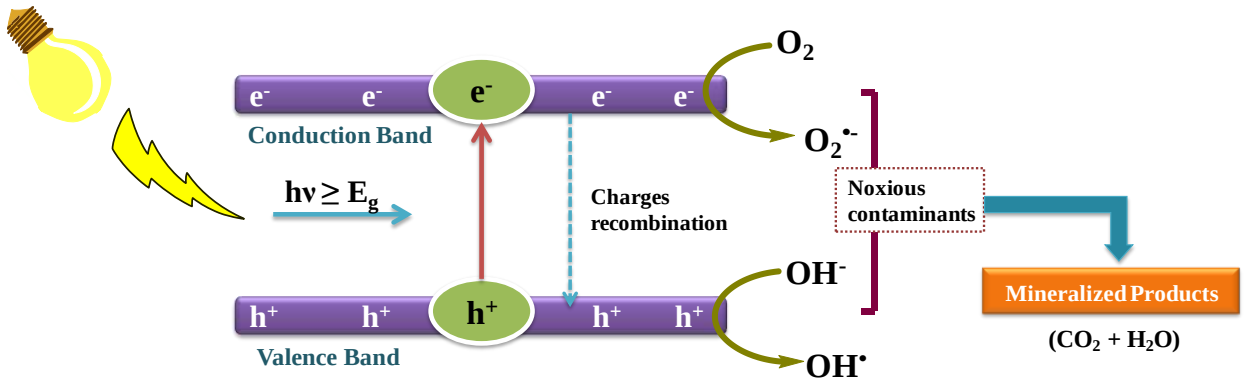

Figure 3.1: Proposed photocatalytic degradation mechanism of semiconductors under light sources.

3.3.5.2 Utilization of solar light as a sustainable energy source

Cost assessment is also a vital aspect of concern in the treatment of these organic contaminants via AOPs (photocatalytic process). Consequently, scientists have spotlighted the natural solar radiation (coming from the sun) as a sustainable source of energy for wastewater treatment by photoactive materials. On account of its enormous accessibility, purity, cost friendliness, and sustainability/feasibility; creates the idea of flourishing this solar energy for diverse purposes is successfully adopted by humankind. The solar band of sunlight comprises

nearly 3-5% of UV radiations and approximately 47% of visible light radiations in terms of energy with the wavelength (λ) of < 400 nm and 400 > λ < 700 nm respectively. In theory, it has been reported that nearly 89,300 TW of solar radiations reached the surface of the earth.[21] Whereas there is a huge space between its assessment and applicability for different purposes, so there is a crucial need to deal with this loophole smartly. The ecologist and scientists are searching for simple approaches and techniques to flourish and exploit this energy for wastewater treatment.

3.3.5.3 Mechanism of photocatalysis process

The mechanism of the photocatalysis process includes intermediary steps; the initial one is the electron-hole pair formation which will happen after the catalyst surface got irradiated with light flux (≤ band-gap of semiconductors) known as the photo-excitation stage of semiconductors.[22] In the photocatalysis process, the electron present in the VB (Valence Band) got an adequate amount of energy from light flux to cross the separation (band-gap) between VB and CB (Conduction Band). After crossing, the electron reaches/arrived at CB and creating electron vacancies in VB known as holes. These holes in VB and electrons in CB behave as strong oxidizing and reducing agents respectively. An electron donor got oxidized when the holes moved to the surface whereas an electron acceptor got reduced when semiconductors donate electrons. The semiconductor can alter its working according to the environment provided or available, like if the semiconductor has an oxygen environment (from dissolved oxygen) that is if the catalyst surface adsorbed molecular oxygen then there will be the generation of superoxide radical ($O_2^{\bullet -}$) species; and if photodegradation reaction was going in a water environment then there will be the generation of hydroxyl radical ($^{\bullet}OH$) species. These radical species ($O_2^{\bullet -}$ and $^{\bullet}OH$) were chiefly answerable for the contaminant's degradation and mechanism.[22,23] The diagrammatic illustration of the photocatalytic degradation mechanism is depicted in **Figure 3.1**.

3.3.5.4 Recombination rate

The light falls on the catalyst surface excites an electron from VB to CB, and creates holes with a positive charge. And this leads to redox reactions on the surface of the photocatalyst which will further give rise to the mineralized products or intermediate products. And if in case these electrons and holes are not quenched after the excitation phenomenon, then they will merge

within picoseconds and diffuses, known as recombination. If this recombination phenomenon occurs at the surface or in bulk then called surface recombination or volume recombination, respectively. This recombination gives rise to loss of energy and thereby reduces quantum efficiency. This process can happen on the surface or in the bulk of photocatalyst due to the reason like defects in the crystal structure. The reaction of e^-/h^+ recombination is:

Electron + hole → neutral centre + exothermic energy (heat) (3.21)

As the formation of electron-hole pairs enhances, the rate of recombination also increases parabolically according to the following **equation 3.22**:

$$r_R = k_R [e^-][h^+] = k_R [e^-]^2 \quad (3.22)$$

The chances of recombination can be reduced by methods like doping, co-catalyst addition, or heterogeneous coupling. The observation was made that after modification with the transition metals (Fe, Cu, Cr, Co, Mn, Mo, V) shifts the light-absorbing capability of the catalyst from UV to the visible region; and they were also found to work as the sites for recombination results in decreased quantum efficiency.[21,24,25] The fabrication of the material with Ag, Au, Pt, Pd metals creates the Schottky defects at the metal-catalyst surface which reduces the chances of recombination.[21,26] It was also examined that small crystallite size can decrease bulk recombination, while this can increase the chances of surface recombination; so controlled and appropriate preparation of these structures can help in tackling this problem.[27]

References

(1) Singh, A.; Srivastava, A.; Srivastava, P. C. Sorption-Desorption of Fipronil in Some Soils, as Influenced by Ionic Strength, PH and Temperature. *Pest Manag. Sci.* **2016**, *72* (8), 1491–1499. https://doi.org/10.1002/ps.4173.

(2) Sharma, M.; Singh, J.; Hazra, S.; Basu, S. Remediation of Heavy Metal Ions Using Hierarchically Porous Carbon Monolith Synthesized via Nanocasting Method. *J. Environ. Chem. Eng.* **2018**, *6* (2), 2829–2836. https://doi.org/10.1016/j.jece.2018.04.042.

(3) Zhu, J.; Wei, S.; Gu, H.; Rapole, S. B.; Wang, Q.; Luo, Z.; Haldolaarachchige, N.; Young, D. P.; Guo, Z. One-Pot Synthesis of Magnetic Graphene Nanocomposites Decorated with Core@double-Shell Nanoparticles for Fast Chromium Removal. *Environ. Sci. Technol.* **2012**, *46* (2), 977–985. https://doi.org/10.1021/es2014133.

(4) Sharma, M.; Choudhury, D.; Hazra, S.; Basu, S. Effective Removal of Metal Ions from Aqueous Solution by Mesoporous MnO_2 and TiO_2 Monoliths: Kinetic and Equilibrium Modelling. *J. Alloys Compd.* **2017**, *720*, 221–229.

https://doi.org/10.1016/j.jallcom.2017.05.260.

(5) Sharma, M.; Hazra, S.; Basu, S. Kinetic and Isotherm Studies on Adsorption of Toxic Pollutants Using Porous ZnO@SiO_2 Monolith. *J. Colloid Interface Sci.* **2017**, *504*, 669–679. https://doi.org/10.1016/j.jcis.2017.06.020.

(6) Goyal, N.; Bulasara, V. K.; Barman, S. Removal of Emerging Contaminants Daidzein and Coumestrol from Water by Nanozeolite Beta Modified with Tetrasubstituted Ammonium Cation. *J. Hazard. Mater.* **2018**, *344* (February), 417–430. https://doi.org/10.1016/j.jhazmat.2017.10.051.

(7) Langmuir, I. The Adsorption of Gases on Plane Surfaces of Glass, Mica and Platinum. *J. Am. Chem. Soc.* **1918**, *40* (9), 1361–1403. https://doi.org/10.1021/ja02242a004.

(8) Sharma, J.; Sharma, M.; Basu, S. Synthesis of Mesoporous MgO Nanostructures Using Mixed Surfactants Template for Enhanced Adsorption and Antimicrobial Activity. *J. Environ. Chem. Eng.* **2017**, *5* (4), 3429–3438. https://doi.org/10.1016/j.jece.2017.07.015.

(9) Zhang, Y.; Jing, C.; Zheng, J.; Yu, H.; Chen, Q.; Guo, L.; Pan, D.; Naik, N.; Shao, Q.; Guo, Z. Microwave Hydrothermal Fabrication of CuFeCr Ternary Layered Double Hydroxides with Excellent Cr(VI) Adsorption. *Colloids Surfaces A Physicochem. Eng. Asp.* **2021**, *628*, 127279. https://doi.org/10.1016/j.colsurfa.2021.127279.

(10) Mukwevho, N.; Gusain, R.; Fosso-Kankeu, E.; Kumar, N.; Waanders, F.; Ray, S. S. Removal of Naphthalene from Simulated Wastewater through Adsorption-Photodegradation by ZnO/Ag/GO Nanocomposite. *J. Ind. Eng. Chem.* **2020**, *81*, 393–404. https://doi.org/10.1016/j.jiec.2019.09.030.

(11) Trikkaliotis, D. G.; Christoforidis, A. K.; Mitropoulos, A. C.; Kyzas, G. Z. Adsorption of Copper Ions onto Chitosan/Poly(Vinyl Alcohol) Beads Functionalized with Poly(Ethylene Glycol). *Carbohydr. Polym.* **2020**, *234*, 115890. https://doi.org/10.1016/j.carbpol.2020.115890.

(12) Khadir, A.; Negarestani, M.; Ghiasinejad, H. Low-Cost Sisal Fibers/Polypyrrole/Polyaniline Biosorbent for Sequestration of Reactive Orange 5 from Aqueous Solutions. *J. Environ. Chem. Eng.* **2020**, *8* (4), 103956. https://doi.org/10.1016/j.jece.2020.103956.

(13) Ghasemi, N.; Ghasemi, M.; Moazeni, S.; Ghasemi, P.; Alharbi, N. S.; Gupta, V. K.; Agarwal, S.; Burakova, I. V.; Tkachev, A. G. Zn (II) Removal by Amino-Functionalized Magnetic Nanoparticles: Kinetics, Isotherm, and Thermodynamic Aspects of Adsorption. *J. Ind. Eng. Chem.* **2018**, *62*, 302–310. https://doi.org/10.1016/j.jiec.2018.01.008.

(14) Wang, N.; Chen, J.; Wang, J.; Feng, J.; Yan, W. Removal of Methylene Blue by Polyaniline/TiO_2 Hydrate: Adsorption Kinetic, Isotherm and Mechanism Studies. *Powder Technol.* **2019**, *347*, 93–102. https://doi.org/10.1016/j.powtec.2019.02.049.

(15) Inyinbor, A. A.; Adekola, F. A.; Olatunji, G. A. Kinetics, Isotherms and Thermodynamic Modeling of Liquid Phase Adsorption of Rhodamine B Dye onto Raphia Hookerie Fruit

Epicarp. *Water Resour. Ind.* **2016**, *15*, 14–27. https://doi.org/10.1016/j.wri.2016.06.001.

(16) Khadir, A.; Motamedi, M.; Negarestani, M.; Sillanpää, M.; Sasani, M. Preparation of a Nano Bio-Composite Based on Cellulosic Biomass and Conducting Polymeric Nanoparticles for Ibuprofen Removal: Kinetics, Isotherms, and Energy Site Distribution. *Int. J. Biol. Macromol.* **2020**, *162*, 663–677. https://doi.org/10.1016/j.ijbiomac.2020.06.095.

(17) Mehta, A.; Mishra, A.; Sharma, M.; Singh, S.; Basu, S. Effect of Silica/Titania Ratio on Enhanced Photooxidation of Industrial Hazardous Materials by Microwave Treated Mesoporous SBA-15/TiO_2 Nanocomposites. *J. Nanoparticle Res.* **2016**, *18* (7), 209. https://doi.org/10.1007/s11051-016-3523-x.

(18) Sharma, S.; Basu, S.; Shetti, N. P.; Kamali, M.; Walvekar, P.; Aminabhavi, T. M. Waste-to-Energy Nexus: A Sustainable Development. *Environ. Pollut.* **2020**, 115501. https://doi.org/10.1016/j.envpol.2020.115501.

(19) Sánchez-Rodríguez, D.; Méndez Medrano, M. G.; Remita, H.; Escobar-Barrios, V. Photocatalytic Properties of BiOCl-TiO_2 Composites for Phenol Photodegradation. *J. Environ. Chem. Eng.* **2018**, *6* (2), 1601–1612. https://doi.org/10.1016/j.jece.2018.01.061.

(20) Herrmann, J. M. Heterogeneous Photocatalysis: Fundamentals and Applications to the Removal of Various Types of Aqueous Pollutants. *Catal. Today* **1999**, *53* (1), 115–129. https://doi.org/10.1016/S0920-5861(99)00107-8.

(21) Bora, L. V.; Mewada, R. K. Visible/Solar Light Active Photocatalysts for Organic Effluent Treatment: Fundamentals, Mechanisms and Parametric Review. *Renew. Sustain. Energy Rev.* **2017**, *76*, 1393–1421. https://doi.org/10.1016/j.rser.2017.01.130.

(22) Srikanth, B.; Goutham, R.; Badri Narayan, R.; Ramprasath, A.; Gopinath, K. P.; Sankaranarayanan, A. R. Recent Advancements in Supporting Materials for Immobilised Photocatalytic Applications in Waste Water Treatment. *J. Environ. Manage.* **2017**, *200*, 60–78. https://doi.org/10.1016/j.jenvman.2017.05.063.

(23) He, W.; Sun, Y.; Jiang, G.; Huang, H.; Zhang, X.; Dong, F. Activation of Amorphous Bi_2WO_6 with Synchronous Bi Metal and Bi_2O_3 Coupling: Photocatalysis Mechanism and Reaction Pathway. *Appl. Catal. B Environ.* **2018**, *232*, 340–347. https://doi.org/10.1016/j.apcatb.2018.03.047.

(24) Wang, T.; Hu, J.; Liu, C. Simultaneous Determination of Insecticide Fipronil and Its Metabolites in Maize and Soil by Gas Chromatography with Electron Capture Detection. *Environ. Monit. Assess.* **2014**, *186* (5), 2767–2774. https://doi.org/10.1007/s10661-013-3577-5.

(25) Han, C.; Ge, L.; Chen, C.; Li, Y.; Xiao, X.; Zhang, Y.; Guo, L. Novel Visible Light Induced Co_3O_4-g-C_3N_4 Heterojunction Photocatalysts for Efficient Degradation of Methyl Orange. *Appl. Catal. B Environ.* **2014**, *147*, 546–553. https://doi.org/10.1016/j.apcatb.2013.09.038.

(26) Gamage McEvoy, J.; Zhang, Z. Antimicrobial and Photocatalytic Disinfection Mechanisms in Silver-Modified Photocatalysts under Dark and Light Conditions. *J. Photochem. Photobiol. C Photochem. Rev.* **2014**, *19* (1), 62–75. https://doi.org/10.1016/j.jphotochemrev.2014.01.001.

(27) Hernández-Alonso, M. D.; Fresno, F.; Suárez, S.; Coronado, J. M. Development of Alternative Photocatalysts to TiO_2: Challenges and Opportunities. *Energy Environ. Sci.* **2009**, *2* (12), 1231–1257. https://doi.org/10.1039/b907933e.

Chapter 4: Adsorptive removal of fipronil by cerium modified zeolite ZSM-5: Equilibrium, kinetic and thermodynamic studies

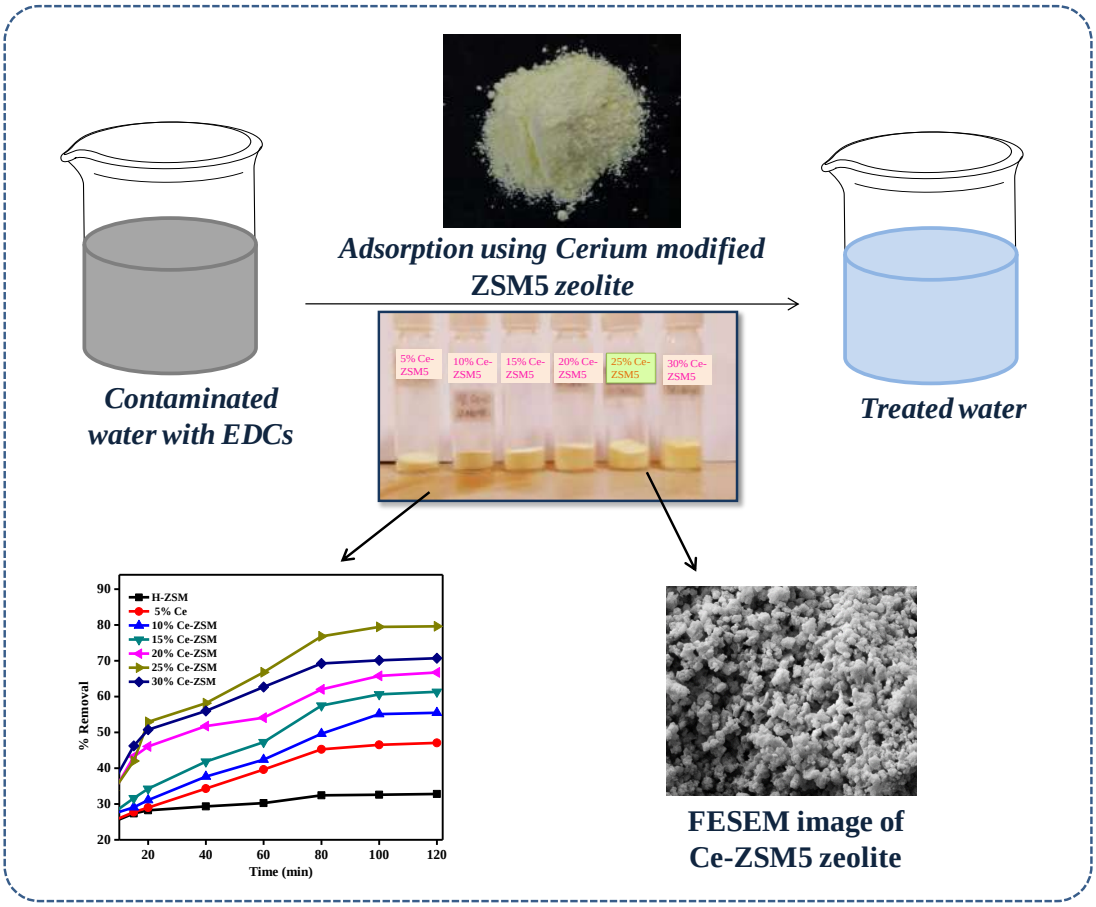

Highlights

- Mesoporous Ce_{25}ZSM-5 zeolite was synthesized via ion-exchange method.
- Modified zeolite possesses excellent adsorption capacity for Fipronil pesticide.
- Langmuir isotherm and Pseudo second-order model fitted best for adsorption process.
- Thermodynamic experiments confirmed the spontaneous & exothermic nature of adsorption.

4.1 Synthesis of modified zeolite

4.1.1 Cerium modified zeolites

Commercially available H-ZSM-5 zeolite was calcined for 3 h at 623K. The calcined zeolite was then refluxed with different percentages of ceric ammonium nitrate solution. In the refluxing set-up, 375K temperature was maintained for 24 hours, and H-ZSM-5 zeolite was modified to cerium modified (Ce-ZSM-5) form. The adsorbents obtained were centrifuged at 8000 rpm and were washed 3-4 times with deionized water and dried in an oven at 393K for 14 hours. Finally, cerium-modified zeolite was calcined at 723K for 4 hours to remove the excess ions.[1] This methodology is pictorially represented in **Scheme 4.1**. The modification of zeolite by cerium was confirmed by characterization techniques such as XRD, BET, FESEM, HR-TEM, EDS, and XPS. The H-ZSM-5 zeolite treated with 5%, 10%, 15%, 20%, 25% and 30% ceric ammonium nitrate solution were designated as Ce_5ZSM-5, Ce_{10}ZSM-5, Ce_{15}ZSM-5, Ce_{20}ZSM-5, Ce_{25}ZSM-5 and Ce_{30}ZSM-5, respectively.

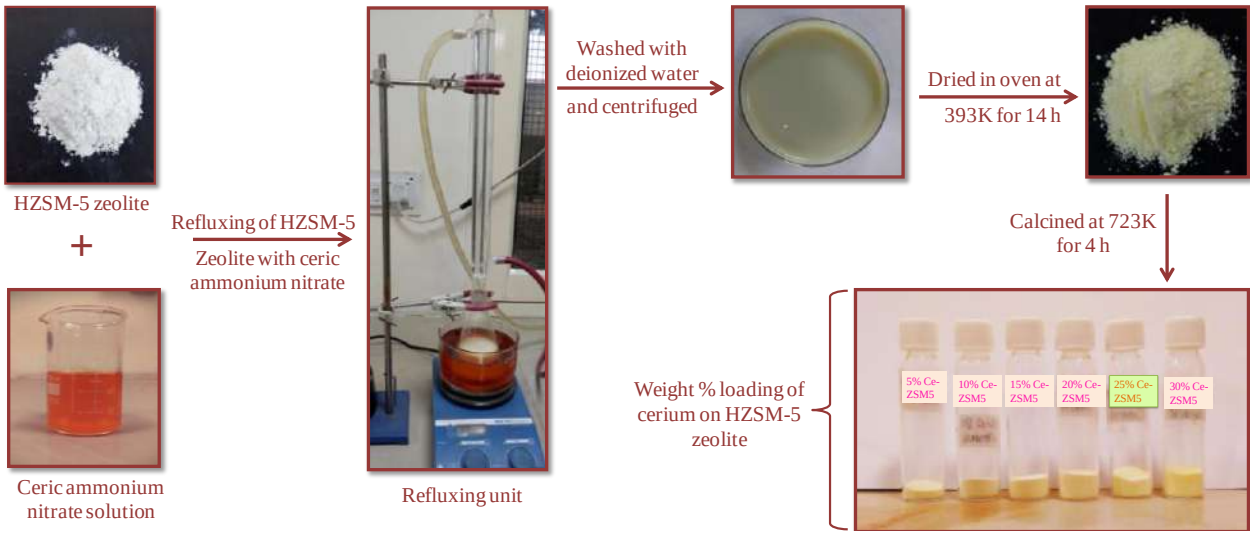

Scheme 4.1: Scheme for preparation of cerium modified (different cerium %) HZSM-5 zeolite.

4.2 Characterization of adsorbents

4.2.1 XRD analysis

The XRD spectrum of Ce-modified H-ZSM-5 zeolite is shown in **Figure 4.1**. It was clearly shown from the spectra that the modification with cerium has successfully been taken place, as

the peaks of CeO_2 was observed at 2θ approximately 28.4°, 32.96°, 47.44°, 56.28°, 59.1°, 69.22°, 76.59°, 78.93°, 88.3° which indexed to (111), (200), (220), (311), (222), (400), (331), (420), (422) planes, analogous to face-centered cubic (fcc) phase of crystalline CeO_2 respectively (JCPDS/PDF 34-0394). The peak observed at 2θ ≈ 23.2° corresponds to the (051) plane of H-ZSM-5 zeolite, signifying that the zeolite retained its original structure (JCPDS 44-0003).

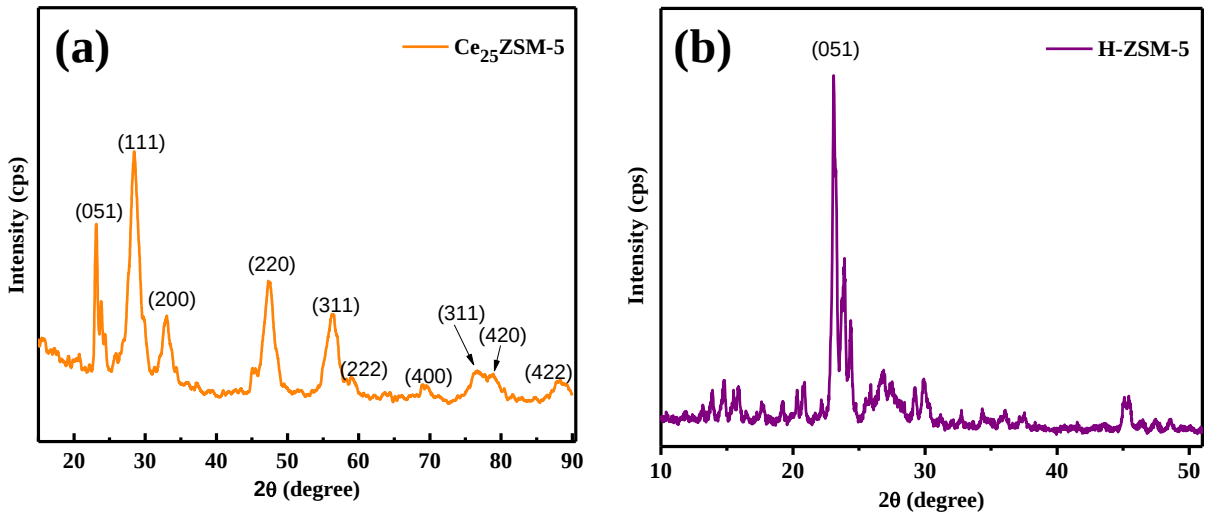

Figure 4.1: XRD spectrum of (a) Ce_{25}ZSM-5 adsorbent and (b) H-ZSM-5 zeolite.

4.2.2 Surface area and pore size distribution analysis

The surface properties of Ce_{25}ZSM-5 were determined by BET surface area and pore size analyzer and are shown in **Figure 4.2**. It has been observed that the physicochemical properties of zeolite changed after modification with cerium. The BET surface area and mean pore diameter of Ce_{25}ZSM-5 were found to be 193 m^2/g and 2.8 nm, respectively. The loaded zeolite with different concentrations of cerium possesses a type-IV isotherm with H2 hysteresis loop that is a feature of mesoporous material (**Figure 4.2a)**. The adsorbed pore volume decreases from H-ZSM-5 to Ce_{20}ZSM-5 zeolite and then it becomes constant for Ce_{25}ZSM-5 and Ce_{30}ZSM-5. The decrease of the pore volume is due to the exchange of cerium which may be blocking the pores. The BJH plot indicates that the pore size distribution of modified mesoporous material lies in the range of 2-50 nm (**Figure 4.2b**). The surface properties of modified zeolite evaluated by N_2 adsorption-desorption are summarized in **Table 4.1**.

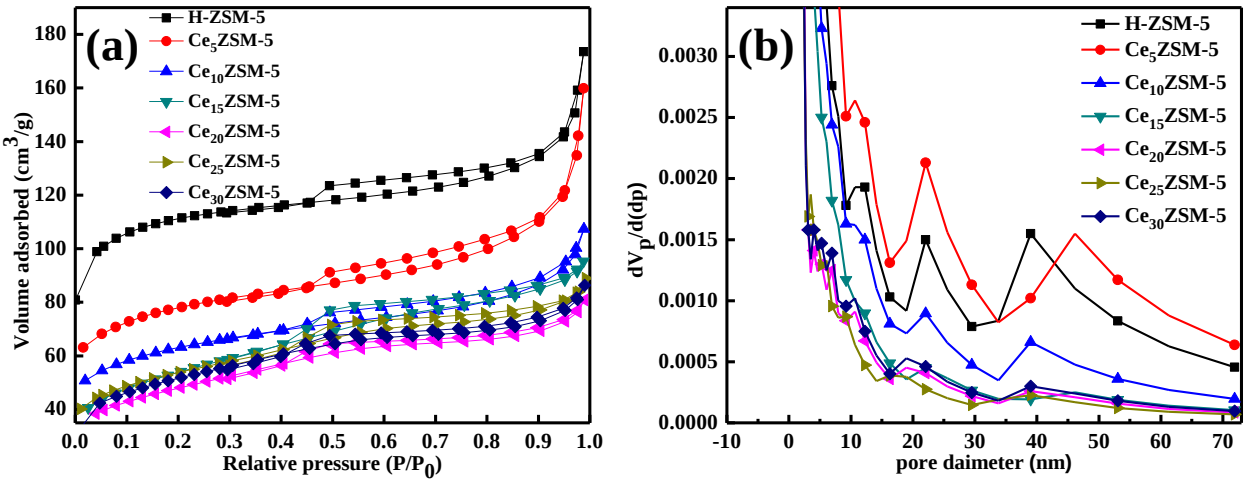

Figure 4.2: (a) Nitrogen adsorption-desorption isotherms, (b) BJH plot of H-ZSM-5 zeolite and different cerium wt% modified zeolite.

Table 4.1: Surface properties of the different modified adsorbents.

Sample	BET surface area (m^2/g) (± 10 m^2/g)	Mesopore diameter (nm)	Total pore volume (cm^3/g)	Micropore diameter (nm)	Micropore volume (cm^3/g)
H-ZSM-5	417	2.58	0.268	0.70	0.169
Ce_5ZSM-5	286	3.46	0.247	0.60	0.108
Ce_{10}ZSM-5	227	2.92	0.166	0.70	0.097
Ce_{15}ZSM-5	198	3.07	0.147	0.70	0.103
Ce_{20}ZSM-5	192	2.91	0.125	0.70	0.093
Ce_{25}ZSM-5	193	2.81	0.136	0.70	0.103
Ce_{30}ZSM-5	181	2.88	0.123	0.70	0.097

4.2.3 XPS analysis

The XPS survey spectrum of the Ce_{25}ZSM-5 shows the presence of cerium and oxygen species (**Figure 4.3a)**. The XPS data depicts that O 1s peak is asymmetric and two deconvoluted peaks appear at 531.3 eV and 534.4 eV (**Figure 4.3b)**. The peak at 531.3 eV (designated by O_α) corresponds to the lattice oxygen from H-ZSM-5 zeolite structure, and 534.4 eV (designated by O_β) is attributed to the surface hydroxyl group.[2–4] The Ce 3d XPS spectrum of the same sample is shown in **Figure 4.3c**. The complex XPS spectra are de-convoluted into $3d_{5/2}$ and $3d_{3/2}$ spin-orbital components (marked as u and v respectively) which relate with $Ce^{4+} \leftrightarrow Ce^{3+}$ electronic

transitions.[5] The four strong peaks having binding energies v (BE ~ 883.9 eV), u (900.5 eV), v'' (898.88 eV), u''' (918.5 eV) and one weak peak v' at 889.7 eV appeared due to Ce^{4+} metal cations. For the peak at BE~ 903.06 eV corresponds to Ce^{3+} cations, which are comparatively weaker than Ce^{4+} cations.[6–8] Therefore, there is co-existence of both Ce^{3+} and Ce^{4+} cations in Ce_{25}ZSM-5 catalyst.[3]

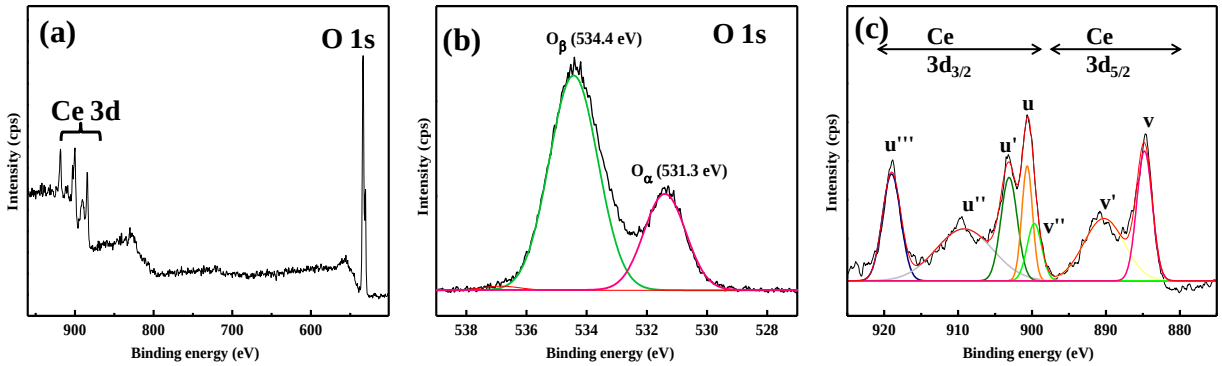

Figure 4.3: XPS (a) survey spectrum, (b) data of O 1s, and (c) Ce 3d of Ce_{25}ZSM-5.

4.2.4 EDS-elemental and FESEM analysis

The EDS spectra depict the elemental composition of modified zeolite by calculating the area under the peak of each element. The peaks of cerium in EDS spectra justifies the presence of cerium in the crystal lattice of zeolite (**Figure 4.4a)**. The presence of silica and alumina indicates the building blocks of actual zeolite were not interrupted. The uniform distribution of elements was confirmed by the color mapping of the sample. The uniform distribution of oxygen and cerium and that of other elements (Na, Si, Al) are shown in **Figure 4.4c-e**. The morphology of the adsorbent was studied by FESEM analysis. The FESEM images ensure that the surface of the catalyst is rough and porous with flattened irregular-shaped structures. In **Figure 4.5b**, the powdered cerium modified zeolite agglomerates are seen which are formed due to interconnections of the individual grains.

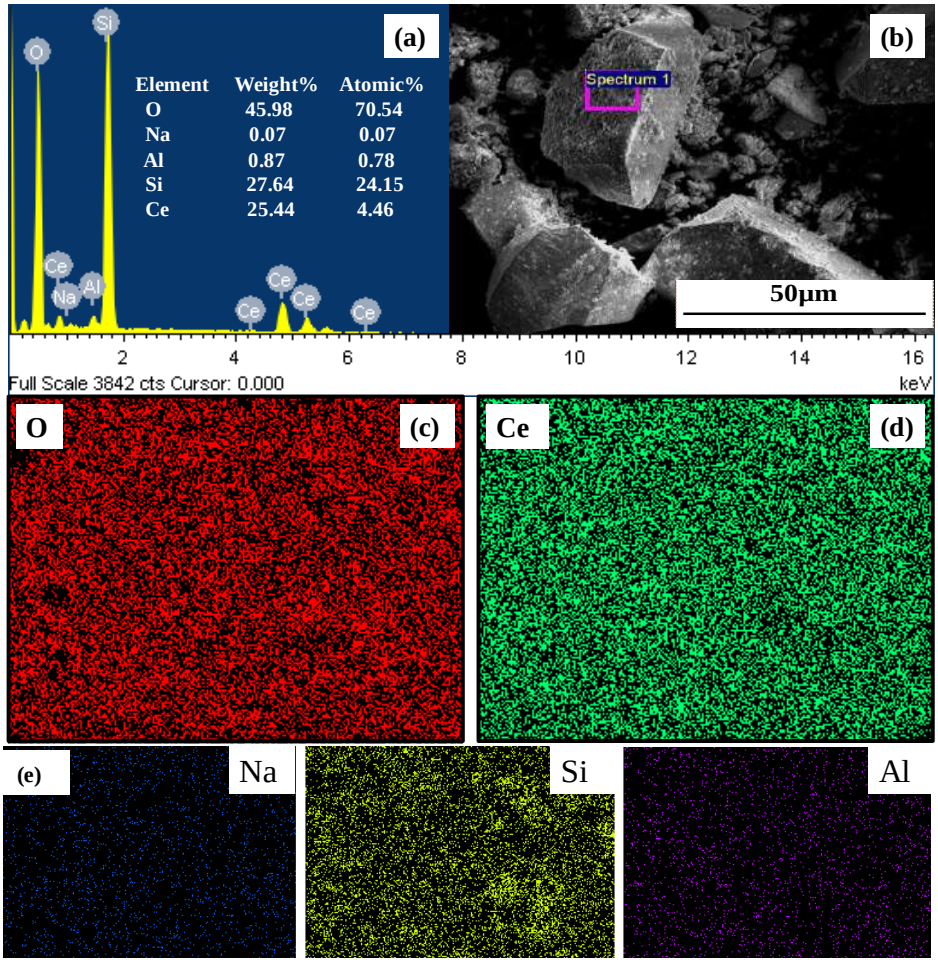

Figure 4.4: (a, b) EDS spectra and SEM image, (c-e) elemental mapping showing the elemental distribution of O, Ce, Na, Si, and Al in Ce_{25}ZSM-5.

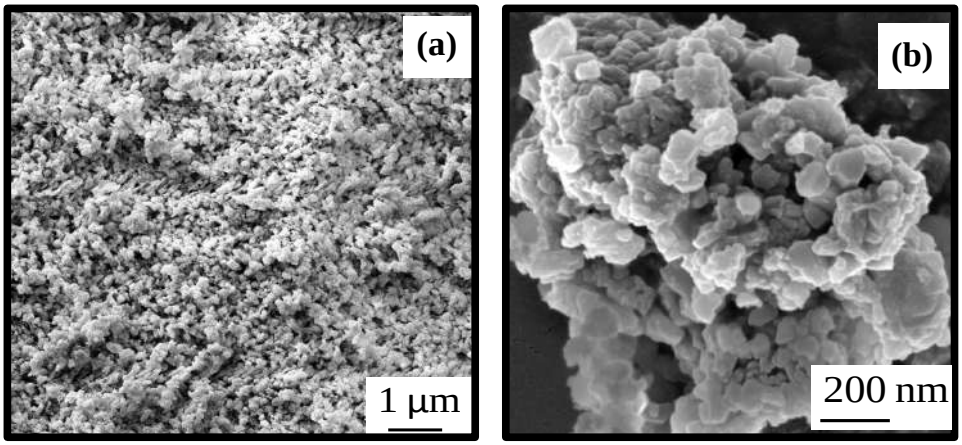

Figure 4.5: (a, b) FESEM images of Ce_{25}ZSM-5 at different scales.

4.2.5 HR-TEM analysis

The Ce_{25}ZSM-5 zeolite adsorbent was characterized by HRTEM analysis to study the insight distribution of cerium crystallites. The sample was comprised of zeolite H-ZSM-5 with the dispersion of cerium onto zeolite and shows characteristic diffraction contrast (**Figure 4.6a, b)**. This analysis shows that the white particles shown in the figure are cerium oxides present in the crystal. The Ce_{25}ZSM-5 zeolite is having crystalline grains and the particle size of 12-18 nm is observed.

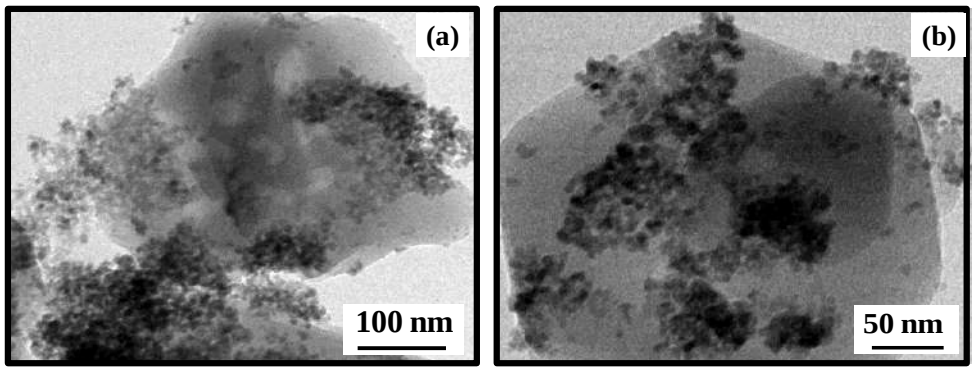

Figure 4.6: (a,b) HRTEM images of Ce_{25}ZSM-5 at different scales.

4.3 Fipronil adsorption performance

The stock solution of FIP pollutant was prepared by dissolving FIP in the solvent. The detailed adsorption mechanism is shown in **Figure 4.7**. The oxygen species present on the adsorbent surface with lone pair of electrons behave as negatively charged species and attracts the positively charged NH_3^+ group of FIP in acidic conditions as shown in **Figure 4.7**. So as a result, the electrostatic interactions are responsible and are regarded as the main driving force in most of the adsorption processes mainly for the surface modified adsorbents.[9] The modifications are done for improving the surface properties or charge to facilitate the adsorption.

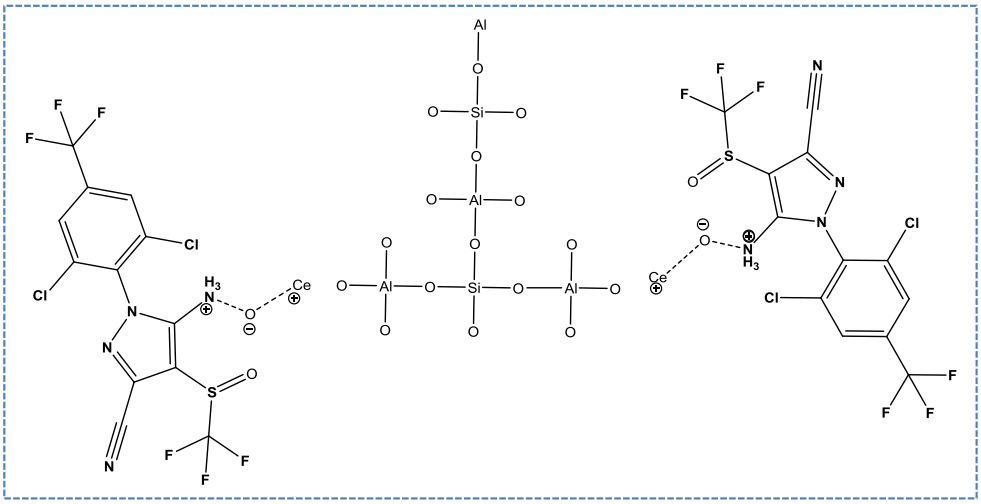

Figure 4.7: Plausible adsorption mechanism of FIP onto Ce_{25}ZSM-5 zeolite surface at acidic pH.

4.3.1 Effect of cerium loading

The cerium loading effect has been studied by varying the weight% of the cerium precursor salt by ion-exchange method and analyzing their adsorptive performances. The fabrication of the metals/metal oxide on the adsorbent bed was regarded as the promoter which increases its efficiency and stability.[10] The generated active sites were balanced by the charge balancing cationic species, the positively charged univalent hydrogen/sodium ions (H^+ or Na^+) were substituted by positively charged polyvalent cerium ions (e.g Ce^{4+}) and this results in increasing the acidity of the exchanged zeolite by enriching the surface with more number of active sites.[10,11] The ammonium form of ZSM-5 zeolite was modified with cerium salts (wt%: 5% to 30%) to form cerium modified zeolite. The removal efficiency of cerium modified zeolites for fipronil pollutants increases from 5 wt% to 25 wt% (47.08% - 79.40%) and there is a decline in removal efficiency (70.40%) for 30 wt% as depicted in **Figure 4.8.** The reason may be due to the decreased surface area of Ce_{30}-ZSM-5 and also the saturation of the active sites.

4.3.2 Effect of contact time

The effect of contact time on adsorption of FIP was investigated with a fixed FIP concentration of 600 mg/L over 1g/L of adsorbent (**Figure 4.9a)**. From this figure, it has been observed that FIP removal increased from 34% to 79.5% with an increase in contact time (40-120 min), and as a result adsorption capacity also increases. The adsorption of FIP was quick at an initial time due to the availability of the number of vacant active sites on the surface of

Ce_{25}ZSM-5, which facilitates decontamination of wastewater.[9] The maximum adsorption is achieved in 120 min. After a long time interval (>120 min), adsorption equilibrium is attained which leads to steady removal of FIP. Therefore, 2 h contact time was used for analyzing the equilibrium and thermodynamic parameters.

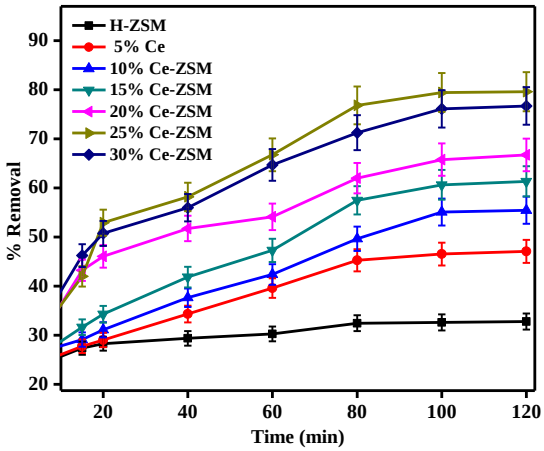

Figure 4.8: Removal efficiency of FIP with different cerium modified zeolite.

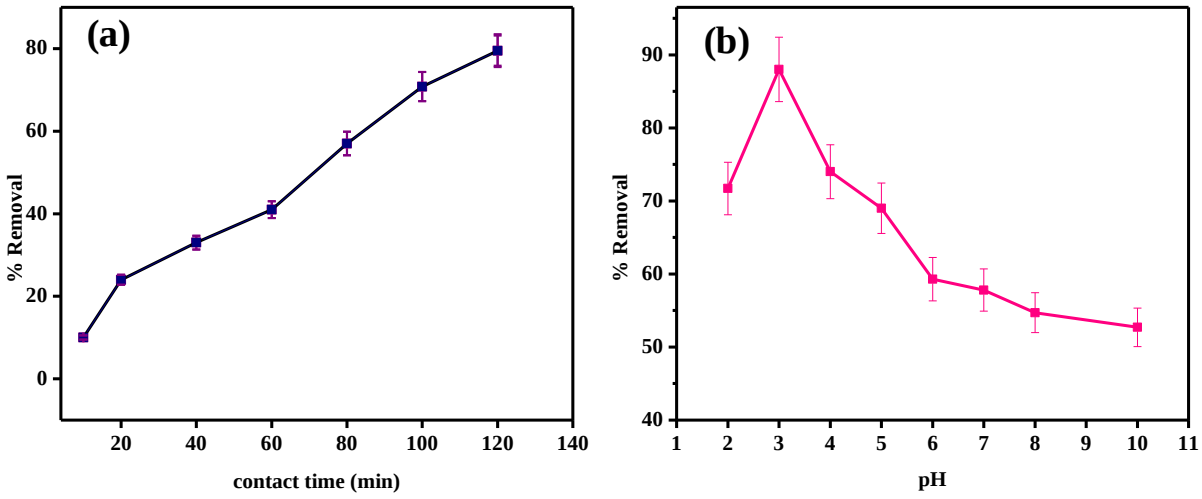

Figure 4.9: Effect of (a) contact time, and (b) pH on FIP adsorption by Ce_{25}ZSM-5.

4.3.3 Effect of pH

Adsorption of EDCs in the surface of modified zeolite mainly depends on the pH of the solution as fluctuations in pH can affect the states of the ionic species in the solution.[12,13] Removal of EDCs by zeolite was analyzed in the range of pH 2-10. The pH values of the EDC

solutions were maintained by using 0.2 M HCl and 0.2 M NaOH solution. Adsorptive removal of FIP increased (from 72.59 to 88.04%) with an increase of solution pH from 2 to 3 because, the positively charged H^+ ions lead to electrostatic attraction with the adsorbent anionic oxygen and positively charged FIP moiety, which becomes advantageous for adsorption phenomena. The later decrease (from 75 to 53.48%) in the pH range of 4-10 is due to deprotonation of the FIP adsorbate which weakens the electrostatic force between the surface of Ce_{25}ZSM-5 and FIP pesticide. This trend was consistent with previous research on the adsorptive removal of EDCs over nano zeolite.[14] The maximum percentage removal (88.04%) was obtained at pH 3 of the solution (**Figure 4.9b**).

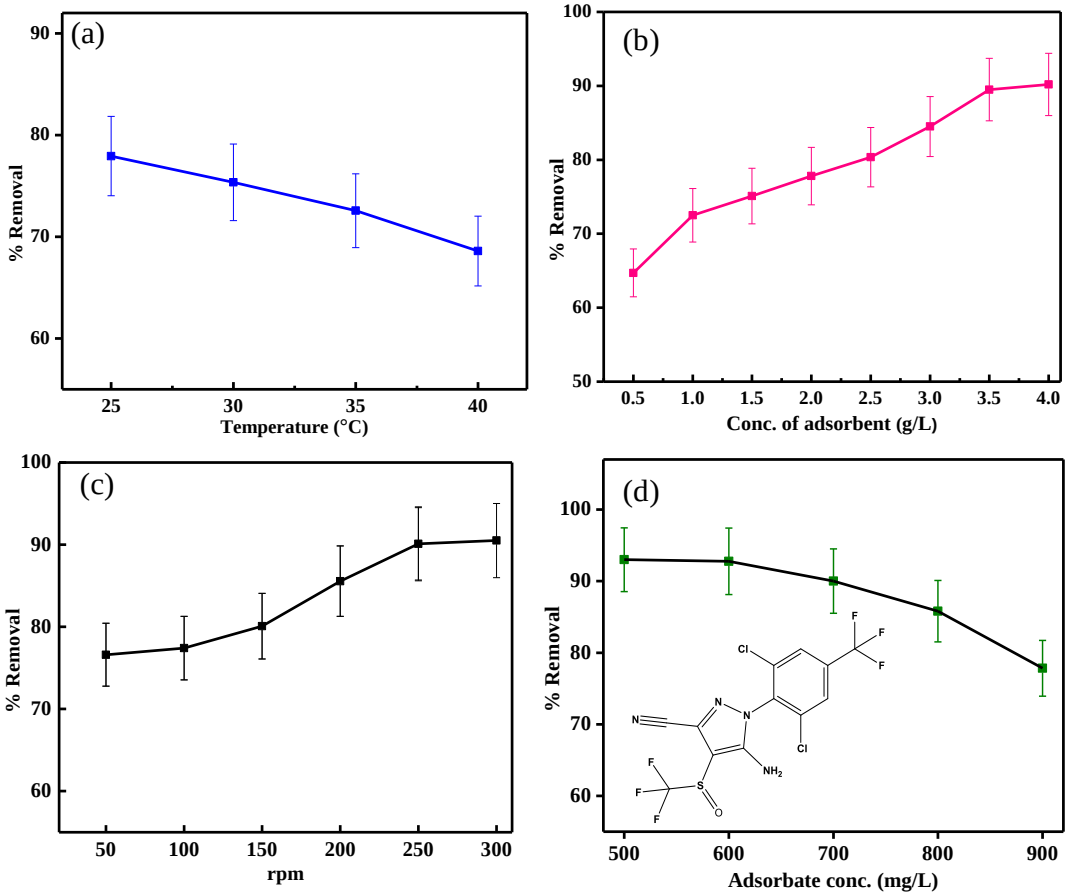

Figure 4.10: Plot for (a) the effect of temperature [adsorbent amount: 1g/L; time: 2h], (b) the effect of adsorbent concentration (g/L) [pH: 3, temp: 25 °C; time: 2h], (c) the effect of rpm [adsorbent amount: 3.5 g/L, temp: 25 °C; time: 2h, pH: 3], and (d) the effect of adsorbate conc. [adsorbent amount: 3.5 g/L, rpm: 250, temp: 25 °C; time: 2 h, pH: 3] (inset contains FIP structure).

4.3.4 Effect of temperature

The effect of temperature on adsorption of FIP onto modified HZSM-5 was studied over a range of temperatures from 25 to 40°C while other parameters remain constant (**Figure 4.10a).** The adsorption of FIP decreases with an increase in temperature, which indicates that low room temperature, facilitates the adsorption process, and adsorption of FIP onto Ce_{25}ZSM-5 is exothermic at room temperature. The maximum percentage removal (>75%) of FIP was observed at 25°C as the molecules attained adequate energy at this temperature so that they can interact with the sorption sites available on the adsorbent surface. At higher temperatures, the electrostatic interaction between the EDC and the active sites destabilizes which shifts the adsorption equilibrium towards the desorption phenomenon.[9] Therefore, 25°C temperature was taken in all further adsorption experiments.

4.3.5 Effect of adsorbent dose

The adsorbent dose of Ce_{25}-ZSM-5 material was examined for the removal of FIP by conducting a series of batch experiments with optimized 600 ppm FIP concentration for 120 min. The Ce_{25}-ZSM-5 concentration was varied from 0.5 g/L to 4.0 g/L. The increase in % removal of FIP was observed till 3.5 g/L that is 90.1% and then it becomes constant as shown in **Figure 4.10b**. This increase may be due to the presence of a high surface area and the availability of a larger number of active sites for adsorption.

4.3.6 Effect of stirring speed

The effect of agitation speed on the removal efficacy of EDC on cerium modified HZSM-5 was observed at pH 3, 3.5g/L concentration of Ce_{25}ZSM-5, and temperature of 25°C for 2 h. It is found that there is an increase in the removal efficiency with the increase in agitation speed from 50-300 rpm, and the maximum % removal observed was 90.5%, which is shown in **Figure 4.10c**. As the rotation speed becomes high, the probability of contact between the adsorbate and adsorbent increases, which facilitates EDC molecule to overcome the film diffusion resistance. From this study, the optimum agitation speed was found to be 250 rpm and after that, almost saturation is attained.

4.3.7 Effect of pollutants concentration

The initial adsorbate (FIP) concentration was varied and its % adsorptive removal was investigated as shown in **Figure 4.10d**. From the graph, it has been seen that with an increase in the concentration (600-900 mg/L) of the pollutant, the % adsorption removal decreases from 92.97% to 77.83%. The reason may be the rapid attainment of the equilibrium due to enhanced driving force with increased FIP pollutant concentration and also the saturation of the sites occurs which are available for adsorption. Therefore, 600 mg/L concentration of FIP pollutant was considered as an optimized concentration because higher % adsorptive removal was observed at this concentration. The high adsorption capacity of Ce-ZSM-5 was found to be 598.80 mg/g. The structure of FIP is shown in **Figure 4.10d** in the inset.

4.4 Adsorption kinetic study

To study the adsorption process of FIP on cerium modified zeolite, different kinetic models like Pseudo-first order, Pseudo-second order, Elovich model, and intra-particle diffusion model were investigated (in **Figure 4.11a-d**). According to the interpreted data, the Pseudo-second order model was the best fitted with a higher regression coefficient than other kinetic models, which confirmed that chemisorption dominated the adsorption process.[12] The calculated kinetic parameters for FIP adsorption are reported in **Table 4.2.**

Table 4.2: Kinetic model parameters for adsorption of EDC – fipronil.

S. No.	Kinetic model	Parameters	Values for FIP
1.	Pseudo-first order	k_1 (min^{-1})	0.0308
		q_e (mg/g)	479.48
		R^2	0.942
2.	Pseudo-second order	k_2 (g/mg.min)	5.927×10^{-5}
		q_e (mg/g)	588.235
		R^2	0.994
3.	Elovich	a (mg/g.min)	47.622
		b (g/mg)	0.00796
		R^2	0.985
4.	Intra-particle diffusion	k_i ($mg/g.min^{0.5}$)	34.529
		C_i (mg/g)	113.155
		R^2	0.981

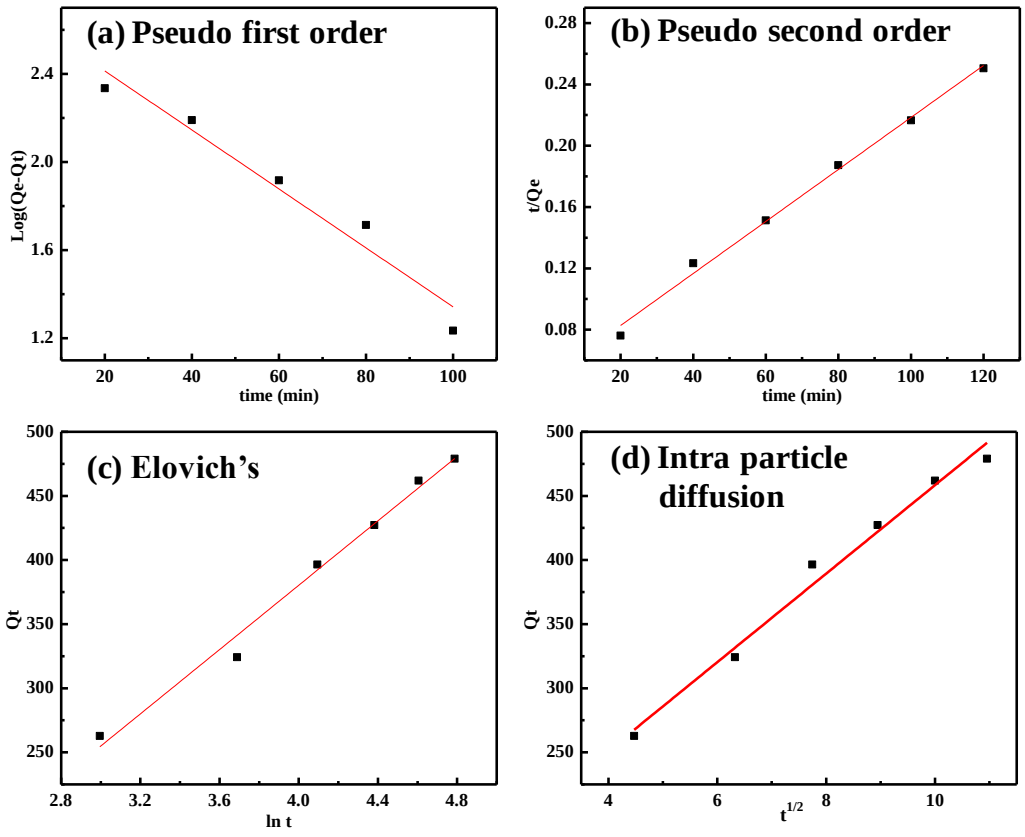

Figure 4.11: Linear fit plots for kinetic models; (a) Pseudo first-order model, (b) Pseudo-second order model, (c) Elovich's model, and (d) Intra-particle diffusion model.

4.5 Adsorption isotherm study

Adsorption isotherm exhibits an appropriate explanation for the adsorption process and efficiency of the adsorbent. Adsorption isotherms evaluate the correlation between the amount of adsorbate (FIP pollutant) molecule that is scattered on the surface of the adsorbent and the concentration of the adsorbate in a liquid solution at equilibrium. The isotherms (**Figure 4.12a-f**) were derived from the experimental data and fitted with the standard adsorption isotherms such as Langmuir, Freundlich, Harkins-Jura, Halsey, and Dubbin-Radushkevich (D-R) isotherm models.[15] The accuracy of the adsorption isotherms was estimated by the value of R^2 (Pearson correlation coefficient). The Langmuir adsorption isotherm was found to fit the best with the highest R^2 value suggesting that in the majority, there was monolayer adsorption of FIP pollutant at the adsorbent surface. The Adsorption isotherm parameters for the Langmuir, Freundlich,

Harkins-Jura, Halsey, and Dubbin-Radushkevich (D-R) isotherm models were listed in **Table 4.3**.

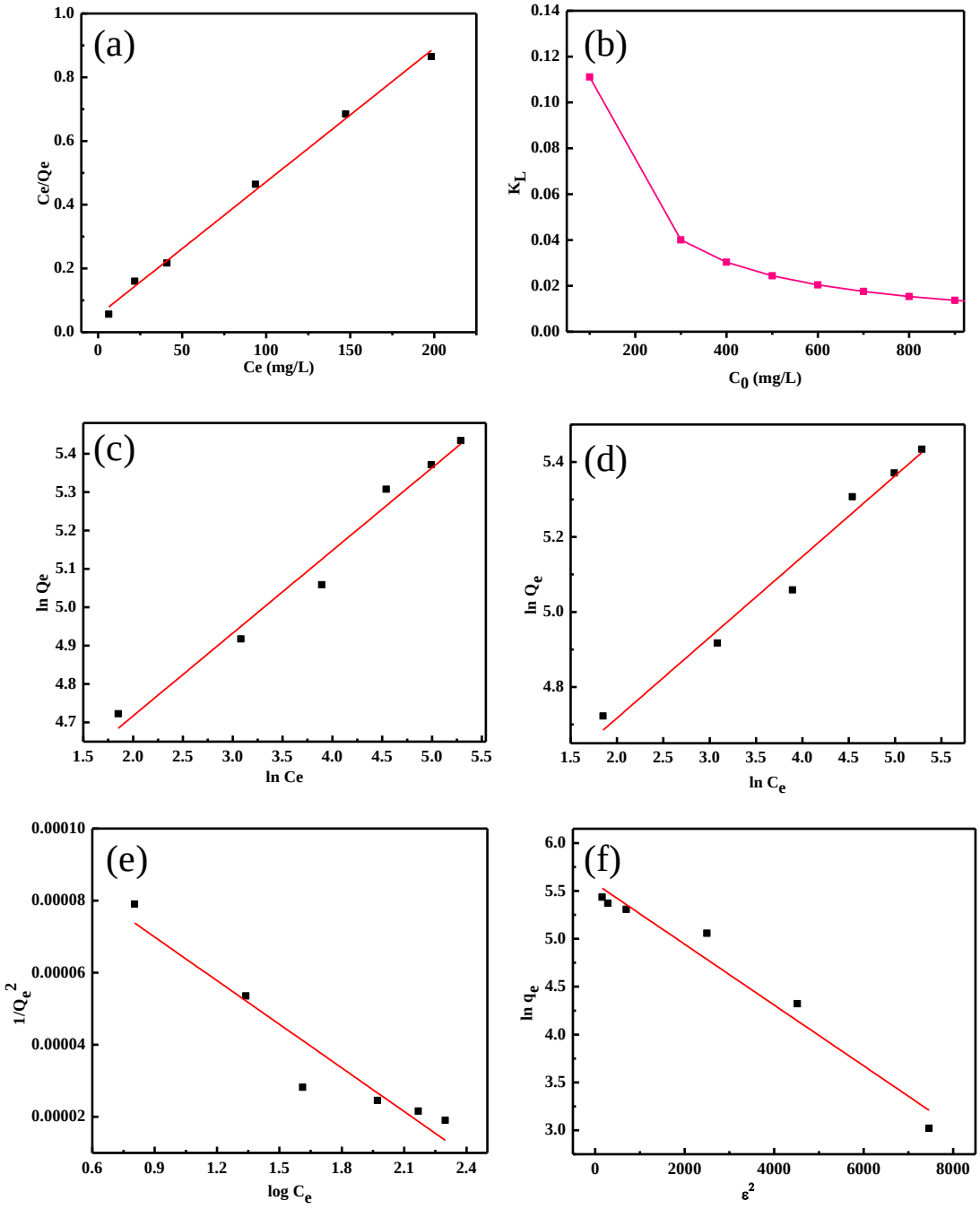

Figure 4.12: Linear fit adsorption isotherm plots for (a) Langmuir isotherm, (b) plot for the parameter of equilibrium R_L, (c) Freundlich isotherm, (d) Halsey model, (e) Harkins-Jura model, and (f) D-R model.

Table 4.3: Model parameters of equilibrium adsorption isotherm for FIP.[16,17]

S. No.	Equilibrium model	Parameters	Values for FIP
1.	Langmuir isotherm	Q_m (mg/g)	238.095
		K_L (L/mg)	0.07998
		R^2	0.9958
2.	Freundlich isotherm	K_F [(mg/g.(L/mg)]$^{1/n}$	72.698
		1/n	0.2154
		R^2	0.972
3.	Harkins-Jura	A	24783.15
		B	2.627
		R^2	0. 8934
4.	Halsey	1/n	-4.643
		K (mg/L)	2.275×10^{-9}
		R^2	0.9719
5.	Dubbin-Radushkevich	Q_S (mg/g)	264.532
		B [(mol/J)^2]	3.17×10^{-4}
		R^2	0.9529

4.6 Thermodynamic study

The thermodynamic parameters such as a change in Gibbs free energy (ΔG°), change in entropy (ΔS°), and change in enthalpy (ΔH°) for the adsorption process were estimated. The values of ΔG° were calculated from the slope and intercept values of the graph in **Figure 4.13**, at four different temperatures (298, 303, 308, and 313 K), at which the adsorption experiments were carried out.

Table 4.4: Thermodynamic parameters for FIP adsorption on Ce_{25}ZSM-5 at different temperatures.

Temperature (K)	Gibbs free energy change, ΔG (kJ/mol)	Enthalpy change, ΔH (J/mol)	Entropy change, ΔS (J/mol K)	R^2
298	-7.20	-2.237	24.171	0.9687
303	-7.32			
308	-7.44			
313	-7.56			

The negative values of ΔG° in **Table 4.4**, indicates that the adsorption process was spontaneous and thermodynamically stable.[13,18] The positive value of ΔS° reveals that the adsorbent was having more affinity towards FIP and there is increased randomness at the solid-

liquid interface during the adsorption process. The negative value of ΔH° depicts that the adsorption process was exothermic.[9,19] The comparative % removal of different materials for different pollutants is tabulated in **Table 4.4** and here it could be concluded that the cerium modified adsorbent could be employed as a good adsorbent for toxic pollutants.

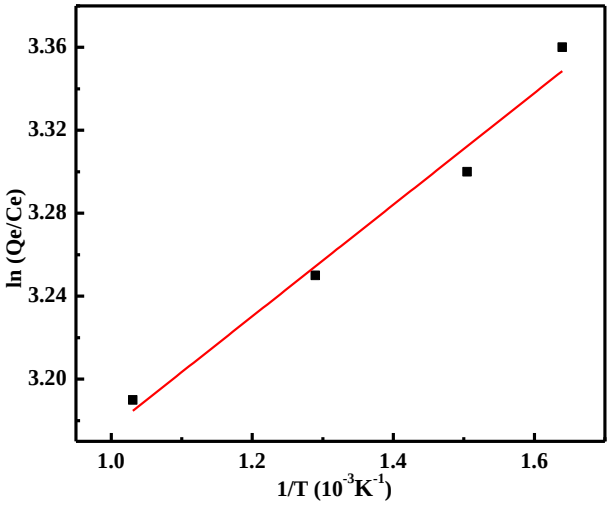

Figure 4.13: Plot of ln(q_e/C_e) versus 1/T for FIP adsorption on Ce_{25}ZSM-5 zeolite.

4.7 Reusability

For monitoring the adsorbent viability for further potential application, it must be evaluated not only by adsorptive capacity but also by regeneration and reusability.

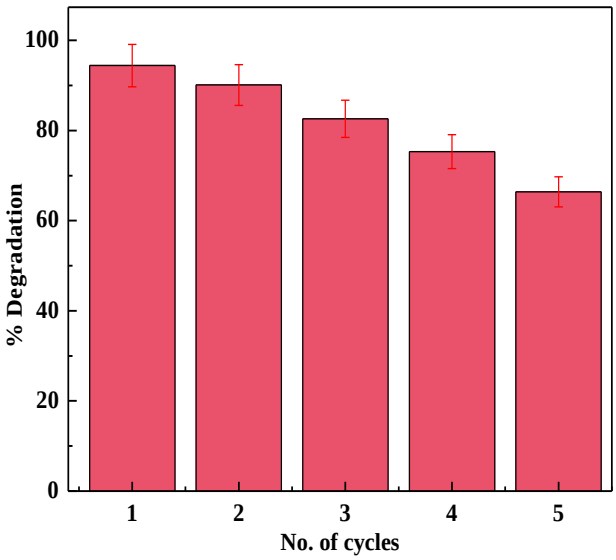

Figure 4.13: Reusability studies of Ce_{25}ZSM-5 adsorbent

In literature, it has been accounted for regeneration methods by using dilute HCl, NaCl, and NaOH, followed by stirring (for 1 hour at room temperature) and drying at 60°C. The initial efficiency of the adsorbent Ce_{25}ZSM-5 was more than 90% and then it decreases to 66.4% after five cycles of regeneration by using HCl, NaOH, and NaCl as the eluent respectively.[20] The data shows that Ce_{25}ZSM-5 can be easily regenerated and has recycling ability after multiple cycles.

4.8 Conclusions

The adsorbent was prepared by modification of cerium onto H-ZSM-5 zeolite by simple ion-exchange method for the removal of FIP pesticide from the aqueous solution. The adsorbent was prepared by refluxing with the cerium salt of different concentrations (wt%) ranging from 5% to 30%. The zeolite modified with 25% cerium salt solution was found to be the best adsorbent for FIP removal. The various parameters like time, pH, adsorbent dose, pesticide concentration, temperature, and stirring speed were optimized by carrying out batch adsorption experiments. The Langmuir adsorption isotherm was best fitted according to the equilibrium data which indicates the monolayer adsorption. The kinetic data for the adsorption experiment explores that the adsorption rate is fast and fitted best in a pseudo-second-order model. The thermodynamic studies reveal that the adsorption process was spontaneous and exothermic in nature.

References

(1) Thakur, R.; Barman, S.; Kumar Gupta, R. Synthesis of Cumene by Transalkylation over Modified Beta Zeolite: A Kinetic Study. *Brazilian J. Chem. Eng.* **2016**, *33* (4), 957–967. https://doi.org/10.1590/0104-6632.20160334s20150333.

(2) Hughes, A. E.; Gorman, J. D.; Patterson, P. J. K.; Carter, R. Unusual Peak Shifts in the Core Levels of CeO2 Films Deposited on Si(100). *Surf. Interface Anal.* **1996**, *24* (9), 634–640.s https://doi.org/10.1002/(SICI)1096-9918(19960916)24:9<634::AID-SIA160>3.0.CO;2-N.

(3) Dou, B.; Lv, G.; Wang, C.; Hao, Q.; Hui, K. S. Cerium Doped Copper/ZSM-5 Catalysts Used for the Selective Catalytic Reduction of Nitrogen Oxide with Ammonia. *Chem. Eng. J.* **2015**, *270*, 549–556. https://doi.org/10.1016/j.cej.2015.02.004.

(4) Mullins, D. R.; Overbury, S. H.; Huntley, D. R. Electron Spectroscopy of Single Crystal and Polycrystalline Cerium Oxide Surfaces. *Surf. Sci.* **1998**, *409* (2), 307–319. https://doi.org/10.1016/S0039-6028(98)00257-X.

(5) Zhang, F.; Wang, P.; Koberstein, J.; Khalid, S.; Chan, S. W. Cerium Oxidation State in Ceria Nanoparticles Studied with X-Ray Photoelectron Spectroscopy and Absorption near Edge Spectroscopy. *Surf. Sci.* **2004**, *563* (1–3), 74–82. https://doi.org/10.1016/j.susc.2004.05.138.

(6) Damyanova, S.; Pawelec, B.; Arishtirova, K.; Huerta, M. V. M.; Fierro, J. L. G. Study of the Surface and Redox Properties of Ceria-Zirconia Oxides. *Appl. Catal. A Gen.* **2008**, *337* (1), 86–96. https://doi.org/10.1016/j.apcata.2007.12.005.

(7) Guo, J.; Wu, D.; Zhang, L.; Gong, M.; Zhao, M.; Chen, Y. Preparation of Nanometric CeO_2-ZrO_2-Nd_2O_3 Solid Solution and Its Catalytic Performances. *J. Alloys Compd.* **2008**, *460* (1–2), 485–490. https://doi.org/10.1016/j.jallcom.2007.05.088.

(8) Fan, J.; Wu, X.; Yang, L.; Weng, D. The SMSI between Supported Platinum and CeO2–ZrO_2–La_2O_3 Mixed Oxides in Oxidative Atmosphere. *Catal. Today* **2007**, *126* (3–4), 303–312. https://doi.org/10.1016/j.cattod.2007.06.005.

(9) Goyal, N.; Bulasara, V. K.; Barman, S. Removal of Emerging Contaminants Daidzein and Coumestrol from Water by Nanozeolite Beta Modified with Tetrasubstituted Ammonium Cation. *J. Hazard. Mater.* **2018**, *344* (February), 417–430. https://doi.org/10.1016/j.jhazmat.2017.10.051.

(10) Thakur, R.; Barman, S.; Gupta, R. K. Kinetic Investigation in Transalkylation of 1,2,4 Trimethylbenzene with Toluene over Rare Earth Metal-Modified Large Pore Zeolite. *Chem. Eng. Commun.* **2017**, *204* (2), 254–264. https://doi.org/10.1080/00986445.2016.1263620.

(11) Thakur, R.; Barman, S.; Halder, G. Surface Modification of Nanocrystalline Zeolite X and Its Application as Catalyst in Synthesis of Cumene in a Packed Bed Flow Reactor: A Kinetic Study. *Int. J. Chem. React. Eng.* **2018**, *16* (2). https://doi.org/10.1515/ijcre-2017-0023.

(12) Sharma, M.; Hazra, S.; Basu, S. Kinetic and Isotherm Studies on Adsorption of Toxic Pollutants Using Porous ZnO@SiO_2 Monolith. *J. Colloid Interface Sci.* **2017**, *504*, 669–679. https://doi.org/10.1016/j.jcis.2017.06.020.

(13) Agarwal, S.; Tyagi, I.; Gupta, V. K.; Ghasemi, N.; Shahivand, M.; Ghasemi, M. Kinetics, Equilibrium Studies and Thermodynamics of Methylene Blue Adsorption on Ephedra Strobilacea Saw Dust and Modified Using Phosphoric Acid and Zinc Chloride. *J. Mol. Liq.* **2016**, *218*, 208–218. https://doi.org/10.1016/j.molliq.2016.02.073.

(14) Goyal, N.; Barman, S.; Bulasara, V. K. Quaternary Ammonium Salt Assisted Removal of Genistein and Bisphenol S from Aqueous Solution by Nanozeolite NaY: Equilibrium, Kinetic and Thermodynamic Studies. *J. Mol. Liq.* **2016**, *224*, 1154–1162. https://doi.org/10.1016/j.molliq.2016.10.088.

(15) Xu, M.; Zhang, Y.; Zhang, Z.; Shen, Y.; Zhao, M.; Pan, G. Study on the Adsorption of Ca^{2+}, Cd^{2+} and Pb^{2+} by Magnetic Fe_3O_4 Yeast Treated with EDTA Dianhydride. *Chem. Eng. J.* **2011**, *168* (2), 737–745. https://doi.org/10.1016/j.cej.2011.01.069.

(16) Zhao, Y.; Li, W.; Liu, Z.; Liu, J.; Zhu, L.; Liu, X.; Huang, K. Renewable Tb/Eu-Loaded Garlic Peels for Enhanced Adsorption of Enrofloxacin: Kinetics, Isotherms, Thermodynamics, and Mechanism. *ACS Sustain. Chem. Eng.* **2018**, *6* (11), 15264–15272. https://doi.org/10.1021/acssuschemeng.8b03739.

(17) Othman, A.; Dumitrescu, E.; Andreescu, D.; Andreescu, S. Nanoporous Sorbents for the Removal and Recovery of Phosphorus from Eutrophic Waters: Sustainability Challenges and Solutions. *ACS Sustain. Chem. Eng.* **2018**, *6* (10), 12542–12561. https://doi.org/10.1021/acssuschemeng.8b01809.

(18) Ma, J.; Zhuang, Y.; Yu, F. Equilibrium, Kinetic and Thermodynamic Adsorption Studies of Organic Pollutants from Aqueous Solution onto CNT/C@Fe/Chitosan Composites. *New J. Chem.* **2015**, *39* (12), 9299–9305. https://doi.org/10.1039/c5nj01876e.

(19) Sharma, M.; Choudhury, D.; Hazra, S.; Basu, S. Effective Removal of Metal Ions from Aqueous Solution by Mesoporous MnO_2 and TiO_2 Monoliths: Kinetic and Equilibrium Modelling. *J. Alloys Compd.* **2017**, *720*, 221–229. https://doi.org/10.1016/j.jallcom.2017.05.260.

(20) Niu, J.; Jia, X.; Zhao, Y.; Liu, Y.; Zhong, W.; Zhai, Z.; Li, Z. Adsorbing Low Concentrations of Cr(VI) onto CeO_2@ZSM-5 and the Adsorption Kinetics, Isotherms and Thermodynamics. *Water Sci. Technol.* **2018**, *77* (9), 2327–2340. https://doi.org/10.2166/wst.2018.157.

Chapter 5: Photoactive porous g-C_3N_4/H-ZSM-5 nano-composite for endocrine-disrupting compound and toxic dye degradation

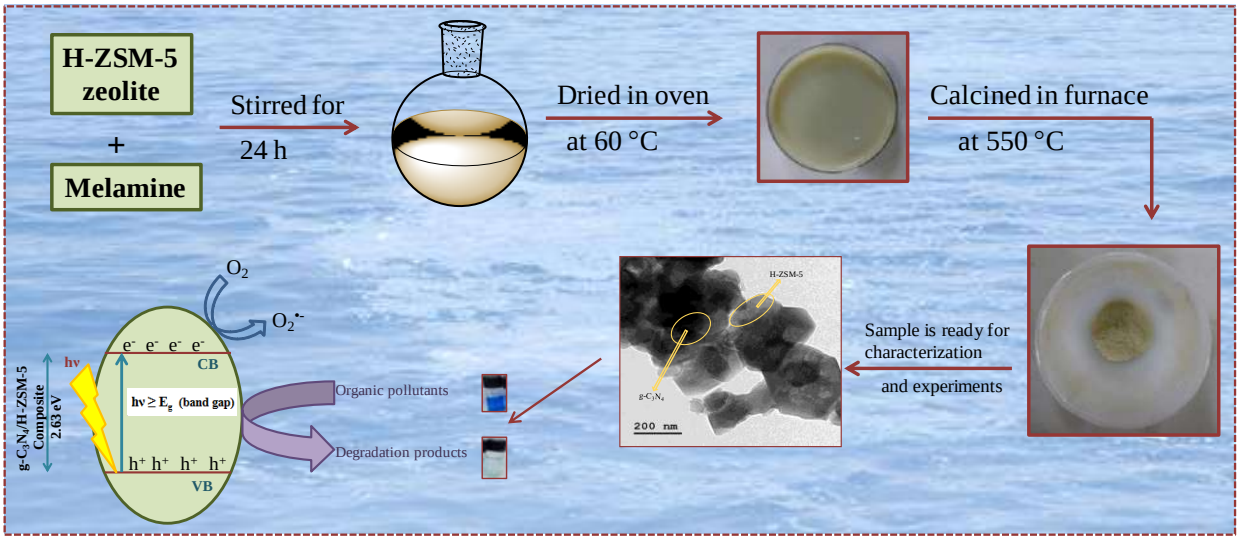

Highlights

- The g-C_3N_4/H-ZSM-5 composite was synthesized by the facile calcination method.
- Fipronil and Methylene blue were degraded to test the photocatalytic activity.
- Maximum photodegradation was obtained by optimizing reaction conditions.
- A scavenger study was performed to find the responsible species for degradation.

5.1 Preparation of g-C_3N_4/H-ZSM-5 composite

About 2.5g of calcined H-ZSM-5 zeolite was taken along with 2.5 g melamine in 50 ml of distilled water. The mixture of zeolite and melamine was stirred for 24 h. Then the slurry was allowed to re-crystallize by drying at 60°C in an oven for 12 h. Then the re-crystallized material was put in the furnace for 2h (10°C/min ramp) at 550°C temperature. The light brownish yellow colored powder was formed after calcination which confirmed the formation of the g-C_3N_4/H-ZSM-5 composite.[1] The scheme for the synthesis of the g-C_3N_4/H-ZSM-5 composite is shown in **Scheme 5.1**.

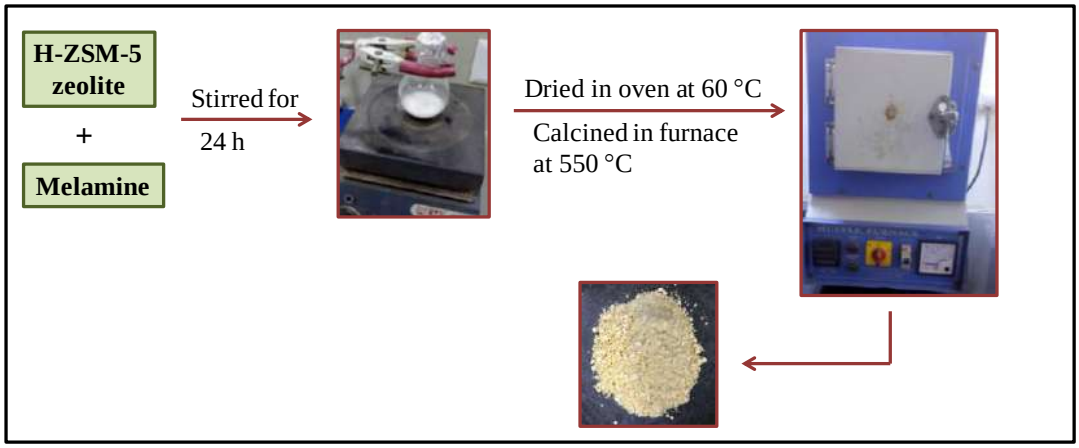

Scheme 5.1: Steps for the synthesis of the g-C_3N_4/H-ZSM-5 composite.

5.2 Characterization of the prepared photocatalyst

5.2.1 XRD analysis

The purity and crystallinity of the synthesized g-C_3N_4/H-ZSM-5 composite were checked by XRD data that is shown in **Figure 5.1a**. The 2θ values at 27.06° and 13.14° corresponded to (002) and (100) planes of crystal faces of g-C_3N_4,[2] that matched with the JCPDS card no 87–1526.[3] The characteristic XRD peaks of H-ZSM-5 zeolite observed at 2θ = 13.88°,14.81°,15.8°,17.69°, 19.26°, 20.75°, 23.16°, 23.90°, 24.46°, 29.28°, 29.93°, 36.15°, 37.54°, 45.05°, and 45.53°, that corresponds to diffraction planes of (102), (301), (202), (400), (312), (113), (332), (303), (133), (352), (630), (800), (352), (10 0 0) and (0 10 0) listed in JCPDS card no 44-0003.[4] Availability of both types (g-C_3N_4 and H-ZSM-5) of peaks in the g-C_3N_4/H-ZSM-5 composite confirms the successful incorporation of g-C_3N_4 into crystalline H-ZSM-5 zeolite. The XRD diffraction pattern of pristine g-C_3N_4 is shown in **Figure 5.1b**. Though the

characteristic peaks of H-ZSM-5 zeolite were not shifted much, confirms that g-C_3N_4 does not disturb the lattice of the H-ZSM-5 zeolite structure.

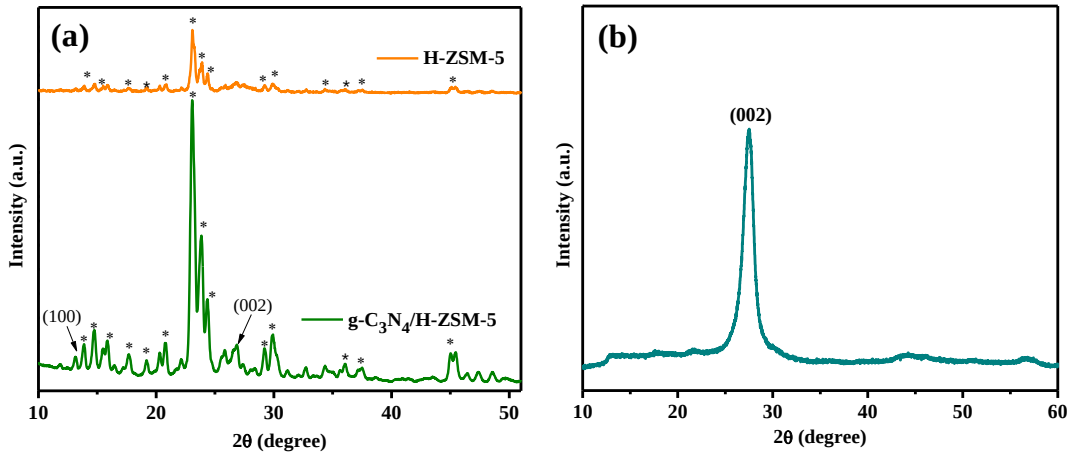

Figure 5.1: XRD pattern of (a) g-C_3N_4, (b) H-ZSM-5, and g-C_3N_4/H-ZSM-5 composite.

5.2.2 BET analysis

The surface area and pore size analysis of g-C_3N_4, H-ZSM-5, and g-C_3N_4/H-ZSM-5 composite were studied by N_2 adsorption-desorption isotherm and BJH pore size distribution, shown in **Figure 5.2a,b**.

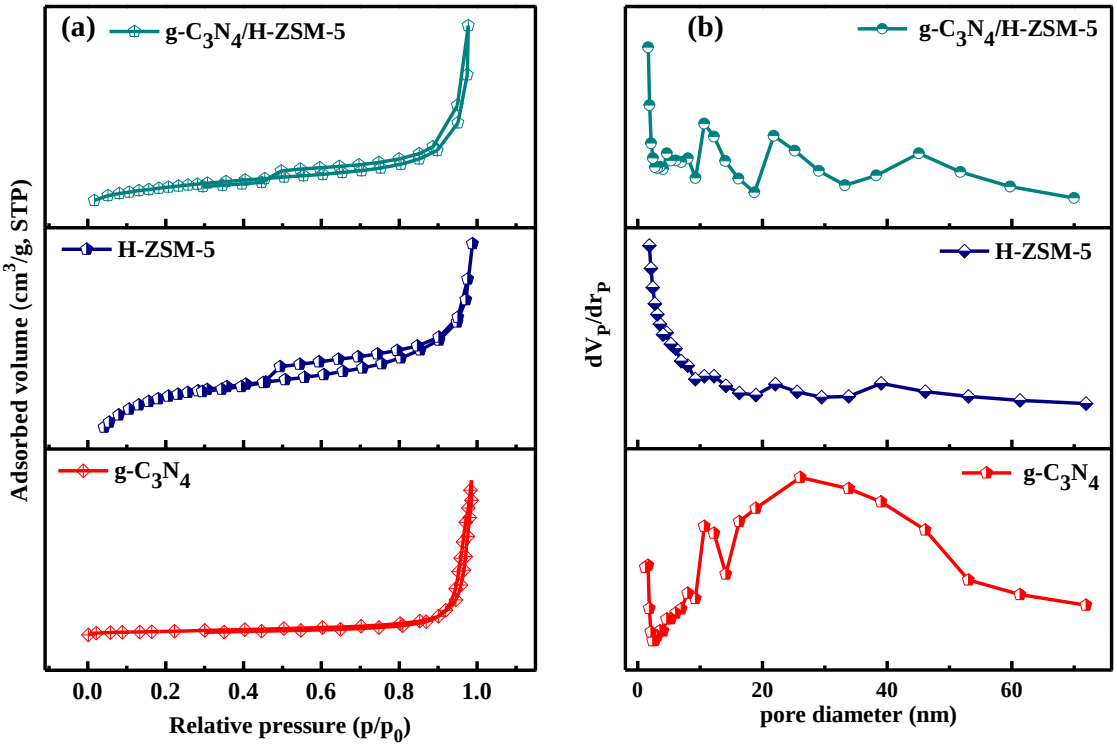

Figure 5.2: (a) N_2 adsorption-desorption isotherms, and (b) pore size distribution curves.

The BET surface areas of g-C_3N_4, H-ZSM-5, and g-C_3N_4/H-ZSM-5 composite were observed to be ~ 88, 417, and 172 m^2/g, respectively as tabulated in **Table 5.1**. This shows that the composite is having a high surface area for eliminating the organic pollutants.[5] The g-C_3N_4 is having a lesser surface area than the composite, so the composite gives better photocatalytic properties than pristine g-C_3N_4. The BJH plot confirms the presence of both micropores and mesopores, which indicates a good sign for the adsorption as well as for the photodegradation process.

Table 5.1: The comparison of surface area, pore size, and pore volume of H-ZSM-5, g-C_3N_4 and g-C_3N_4/H-ZSM-5 composite.

Sample	Surface area (m^2/g)	Mean pore diameter (nm)	Micropore volume (cm^3/g^{-1})	Mesopore volume (cm^3/g^{-1})
H-ZSM-5	417	2.57	0.170	0.114
g- C_3N_4	88	20.37	0.005	0.425
g-C_3N_4/H-ZSM-5	172	4.25	0.064	0.118

5.2.3 XPS analysis

The XPS survey spectrum of the g-C_3N_4/H-ZSM-5 composite is shown in **Figure 5.3a**. The presence of C and N elements in the composite suggests that incorporation of g-C_3N_4 into the H-ZSM-5 zeolite structure was successfully taken place (**Figure 5.3a-c**). In the high-resolution spectrum of carbon (C) 1s, the peak at 284.09 eV corresponds to adventitious carbon C=C (sp^2 hybridized)[1,6] and the major peak observed at 287.65 eV assigned to C-N-C and C-(N_3) groups in the g-C_3N_4/H-ZSM-5 composite.[7,8] The less intense peak at 293.47 eV assigned to one of the carbon species present in tri-s-triazine ring linked to terminal groups like uncondensed –NH_2.[9] The high-resolution peak of N 1s was deconvoluted into 3 peaks namely at 398.14 eV for C=N-C (sp^2 hybridized nitrogen),[10,11] second at 399.71 eV which is due to amino-functional moieties attached with tertiary nitrogen (N-(C3) and C-N-H) and the third deconvoluted peak at 403.75 eV which is weak and assigned to π excitation in g-C_3N_4/H-ZSM-5 composite due to g-C_3N_4.[10,12]

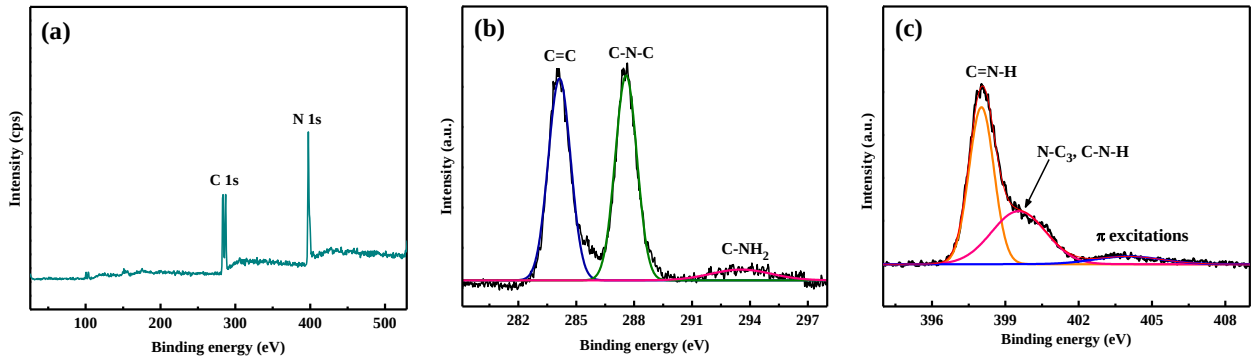

Figure 5.3: (a) XPS survey, (b) deconvoluted peaks of Carbon, and (c) Nitrogen of g-C_3N_4/H-ZSM-5 composite.

5.2.4 EDS and elemental mapping analysis

The EDS analysis has the peaks of carbon and nitrogen which depicts that the formation of g-C_3N_4 has been successfully taken place.

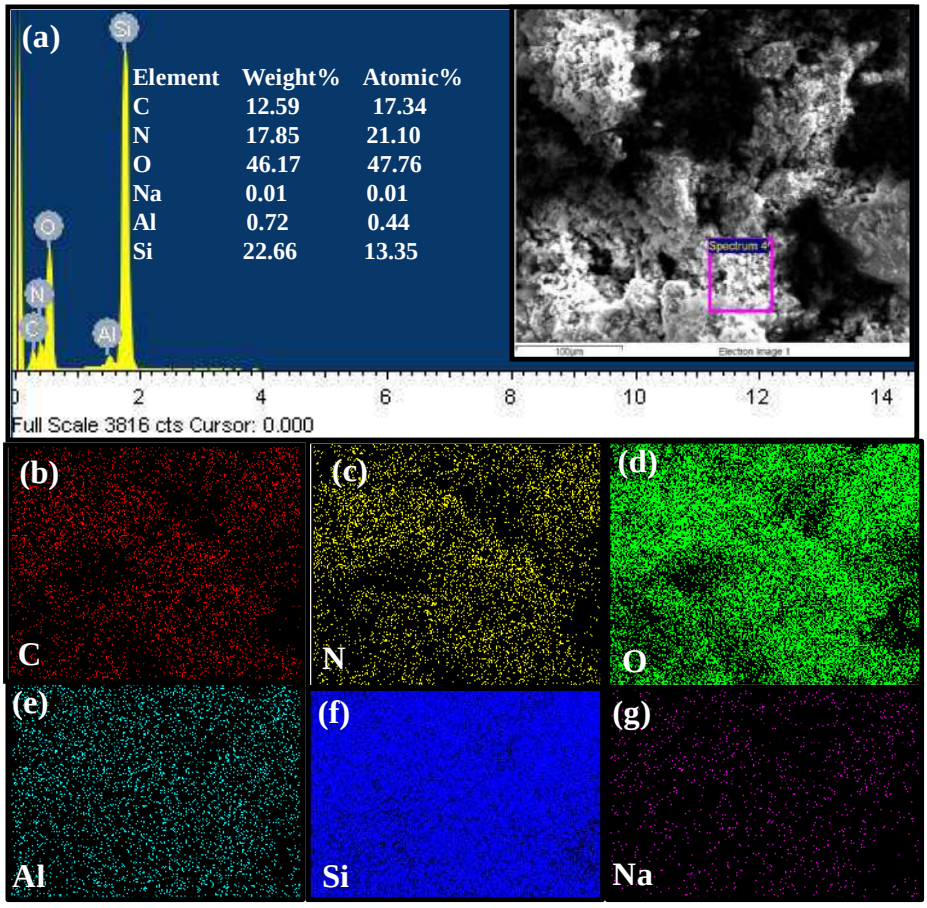

Figure 5.4: (a) EDS spectrum and SEM micrograph with elemental mappings of (b) Carbon and (c) Nitrogen of the g-C_3N_4/H-ZSM-5 composite.

The SEM image in **Figure 5.4a** indicates that the surface of the g-C_3N_4/H-ZSM-5 composite is rough and porous, and the EDS data tells us about the weight percent of the elements present in the composite. The available elements C, N, O, Si, Al, and Na are having 12.59, 17.85, 46.17, 22.66, 0.72, and 0.01 wt% present in the composite. The color mapping analysis of C and N indicate the presence of g-C_3N_4 while O, Si, Al, and Na appeared for the H-ZSM-5 zeolite. The results of elemental mapping shown in **Figure 5.4b-g** suggest that there is a homogeneous distribution of carbon, nitrogen, oxygen, and other elements for the synthesized g-C_3N_4/H-ZSM-5 composite.

5.2.5 FESEM and HRTEM analysis

The FESEM images in **Figure 5.5a,b** depicts that the surface of the g-C_3N_4/H-ZSM-5 composite was not smooth which means it has irregularity/roughness on the surface of the catalyst and possesses pores like mesopores and micropores.

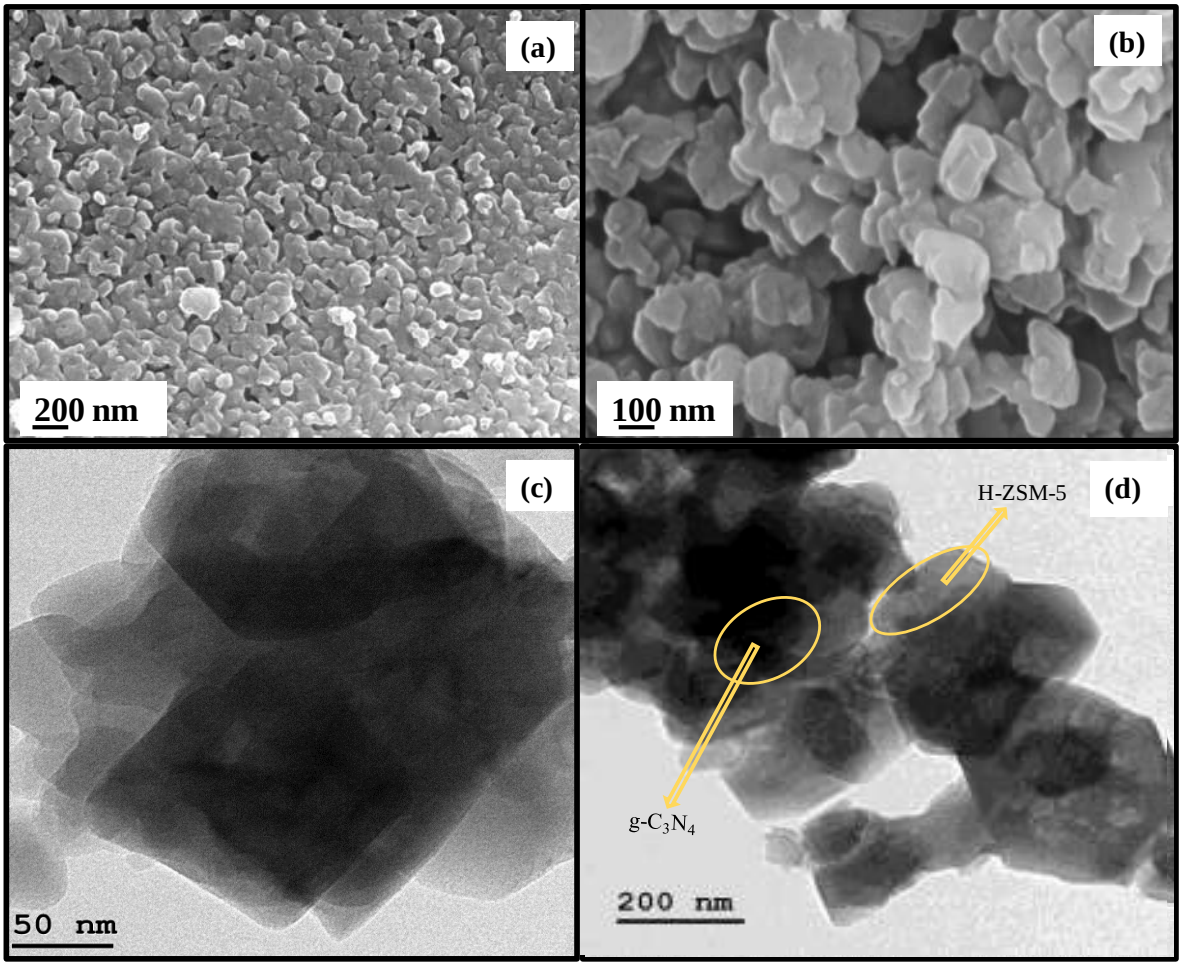

Figure 5.5: (a, b) FESEM images, and (c, d) HRTEM images of g-C_3N_4/H-ZSM-5 composite.

In the high-resolution image of the g-C_3N_4/H-ZSM-5 composite (**Figure 5.5c,d**), it is observed that there are irregular plate-like structures that may lead to the increased surface area of the catalyst, and further helps in the elimination of organic pollutants. The HRTEM images indicate the layered structure of g-C_3N_4 with the crystalline structure of the H-ZSM-5 zeolite as shown in **Figure 5.5d**.

5.2.6 Optical properties

The photoluminescence (PL) analysis was done by PL emission spectra used to elaborate the efficacy of charge carrier scavenging, transfer, or separation and for studying the role of photogenerated electron-hole pairs in the g-C_3N_4/H-ZSM-5 composite and g-C_3N_4 material. In general, the less intense peak of the PL spectra reveals (lower the recombination rate) a longer lifetime and high separation of photo-induced electrons and holes.[13–15] The PL of g-C_3N_4 and g-C_3N_4/H-ZSM-5 composite was performed at an excitation wavelength of 365 nm as shown in **Figure 5.6a**. The g-C_3N_4/H-ZSM-5 nanocomposite shows its emission peak at 428 nm which corresponds to green emission.[16] The PL spectra of pure H-ZSM-5 zeolite indicate that the observed peak was broad and highly intense at the same excitation wavelength as shown in **Figure 5.6b**. The PL intensity of the g-C_3N_4/H-ZSM-5 composite was much lesser than that of pure g-C_3N_4 material. It indicates that the H-ZSM-5 zeolite was perfectly incorporated into the g-C_3N_4 matrix and the rate of recombination of electron-hole pairs is decreased on the surface of the g-C_3N_4/H-ZSM-5 composite.

The optical properties like bandgap and light absorption range were examined by diffused reflectance spectroscopy (DRS). By drawing tangent, in **Figure 5.6c,** the excitation absorption peak was observed for g-C_3N_4/H-ZSM-5 composite at 480 nm. The graph indicates that the composite absorbs light in the visible region which indicates that g-C_3N_4/H-ZSM-5 composite is visible light active material. The optical band gap (E_g) was calculated by using **Equation 5.1:**

$$(\alpha h\nu)^{1/2} = A(h\nu - E_g) \quad (5.1)$$

Where α represents the absorption coefficient, A is constant, hν signifies the photon energy and E_g is the optical bandgap.[1] The energy gap value of as-synthesized g-C_3N_4/H-ZSM-5 composite is shown in **Figure 5.6d**. Tauc's plot suggests that the bandgap of the g-C_3N_4/H-ZSM-5 composite is 2.63 eV.[16]

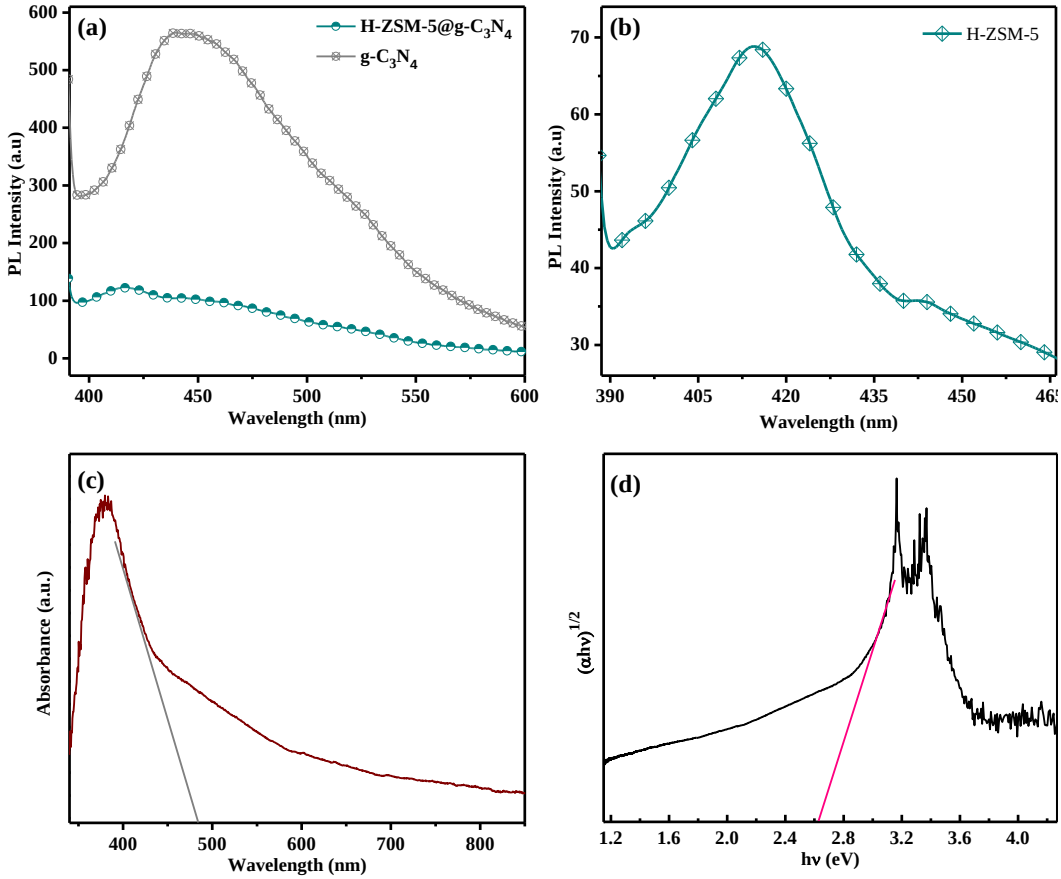

Figure 5.6: (a) Photoluminescence spectra of g-C_3N_4, g-C_3N_4/H-ZSM-5 composite and (b) H-ZSM-5 zeolite, (c) UV Visible diffuse reflection spectra, and (d) tauc plot of g-C_3N_4/H-ZSM-5 composite.

5.3 Photocatalytic degradation of MB and FIP

To analyze the photocatalytic behavior of the g-C_3N_4/H-ZSM-5 composite, the photodegradation experiments were carried out with organic pollutants i.e. MB dye and FIP pesticide in the different light sources (UV, visible, and sunlight). In the photodegradation experiment, the initial concentration of MB and FIP were about 5 mg/L and 600 mg/L, respectively. The time taken for the adsorption-desorption equilibrium of MB and FIP was 40 min and 50 min, respectively in the dark conditions. After attaining equilibrium, the experiment was continued for 120-140 min in the visible light source for the degradation purpose.

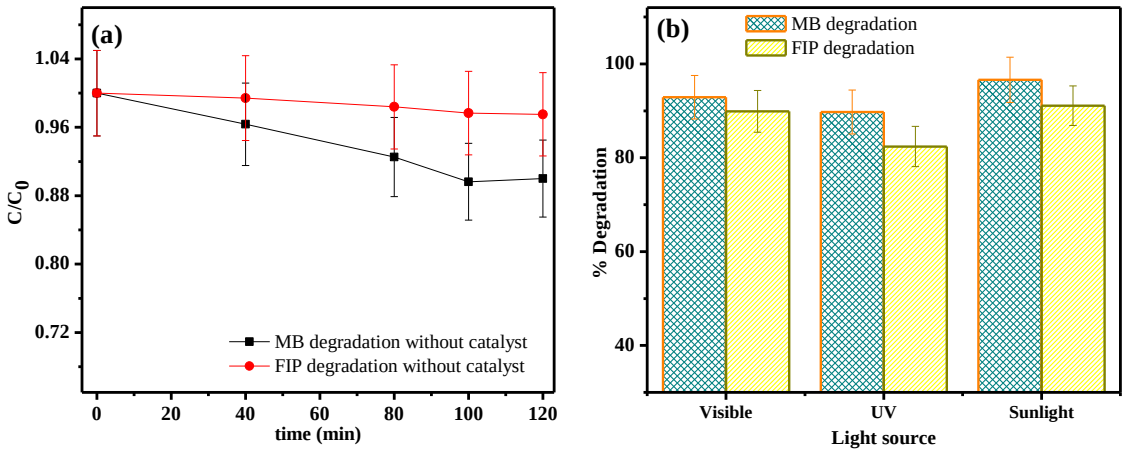

Figure 5.7: (a) The C/C_0 graph of the MB and FIP degradation without catalyst, (b) effect of various light sources for MB and FIP degradation.

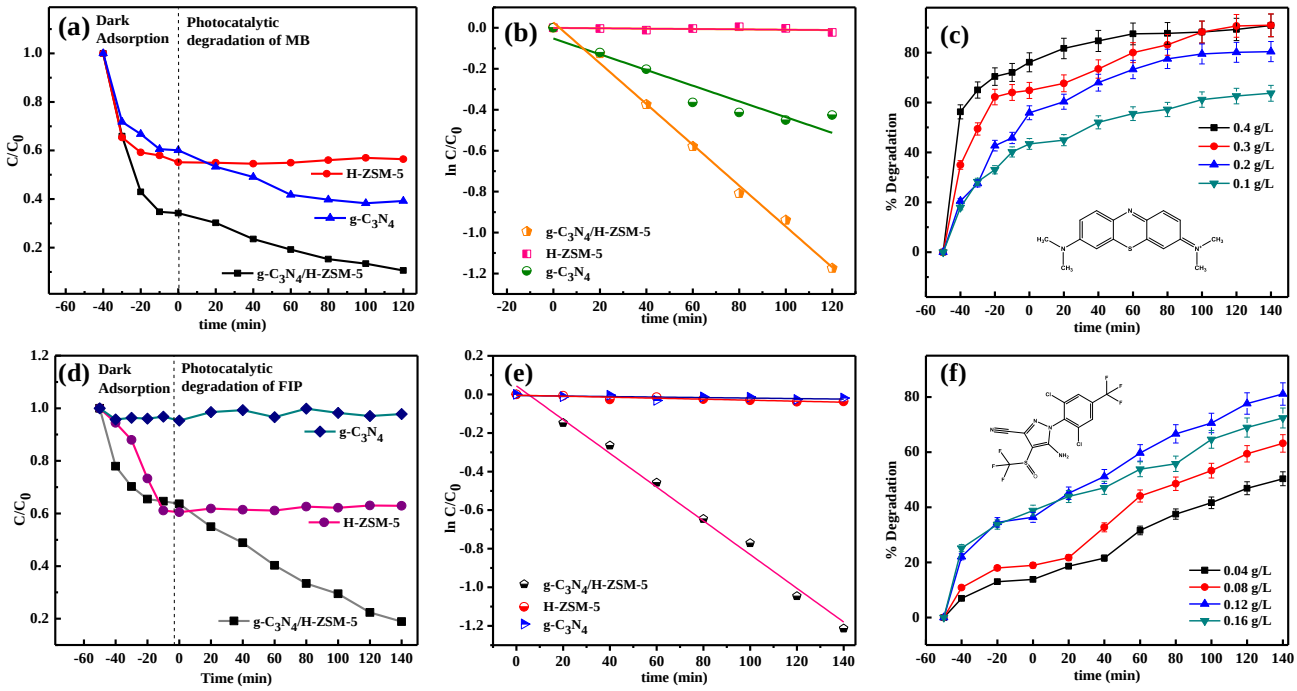

Figure 5.8: Photocatalytic degradation of MB [pH 7.5 (natural pH of MB), time 120 min]: (a) C/C_0, (b) ln C/C_0, of g-C_3N_4/H-ZSM-5 composite [0.3 g/L], g-C_3N_4 [0.15 g/L] and H-ZSM-5 [0.15 g/L], (c) effect of catalyst dose [0.1 g/L – 0.4 g/L], and photocatalytic degradation of FIP [pH 5.5, time 140 min]: (d) C/C_0, (e) ln C/C_0 of g-C_3N_4/H-ZSM-5 composite [0.12 g/L], g-C_3N_4 [0.06 g/L] and H-ZSM-5 [0.06 g/L] (f) effect of catalyst dose [0.04 g/L – 0.16 g/L].

The degradation experiment without photo-catalyst was also studied in which the dye/pesticide was kept under illumination with a visible light source for 120 min/140 min. The absorbance value for both MB and FIP remains almost constant which indicates that for the degradation of the dye and pesticide, g-C_3N_4/H-ZSM-5 photo-catalyst is highly required (**Figure 5.7a**). For comparison purposes, the degradation experiment of MB and FIP was also carried out in UV light and sunlight at optimum conditions (**Figure 5.7b**). The degradation experiments were carried out under direct solar irradiation in the 4th week of October 2018 and the 3rd week of April 2019 for MB and FIP degradation respectively. The sunlight intensity was measured with the Pyranometer (LICOR) instrument, USA - Solar radiation (Watt per square meter) with an average solar flux (~ 706 W/m^2) for MB and (495-920 W/m^2) FIP degradation.

The absorbance value of MB and FIP decreases with an increase in the illuminating time at their corresponding maximum wavelengths. The kinetic studies of MB and FIP with g-C_3N_4/H-ZSM-5 were shown in **Figure 5.8a-f**, which indicates that these pollutants MB and FIP were almost completely degraded with high rate constants of 0.00997 and 0.00875 min^{-1} respectively. The rate constants, light intensity, and reaction conditions for MB and FIP degradation by H-ZSM-5, g-C_3N_4, and g-C_3N_4/H-ZSM-5 composite are given in **Table 5.2**. The degradation efficiency of MB was ~90% and FIP was ~80% at normal room temperature and natural pH with optimum photocatalyst dose.

Table 5.2: Rate constants for the degradation of MB and FIP.

Sample	Light intensity	Conditions	Rate constants	
		Dose, pH, and time	MB (min^{-1})	FIP (min^{-1})
H-ZSM-5	125 W/m^2	0.15 g/L, natural pH 7.5, 120 min – MB	0.000088	0.00026
g- C_3N_4			0.0034	0.00013
g-C_3N_4/H-ZSM-5		0.06 g/L, natural pH 5.5, 140 min – FIP	0.00997	0.00875

5.3.1 Effect of catalyst dose

The effect of catalyst dose on photodegradation was investigated to evaluate the optimum amount of photocatalyst required for the degradation of organic pollutants. Experiments were carried out over different catalyst doses such as 0.1, 0.2, 0.3, and 0.4 g/L for the degradation of MB **(Figure 5.8c)** and 0.04, 0.08, 0.12, and 0.16 g/L for degradation of FIP as shown in **Figure**

5.8f. From the performed experiments, it has been observed that, on increasing the concentration of the catalyst the degradation efficiency of the organic pollutants increases. But at higher concentrations, some saturation occurred due to the opacity of the solution. Therefore, the optimized catalyst (g-C_3N_4/H-ZSM-5) dose i.e. 0.3 g/L for MB degradation and 0.12 g/L for FIP at an optimal time interval of 120 min and 140 min, respectively.

5.3.2 Effect of pH

The pH is a major factor that controls the photocatalytic mechanism as it can influence the surface charge of the photocatalyst. To study the effect of pH on the photocatalytic degradation of organic pollutants (MB and FIP) onto g-C_3N_4/H-ZSM-5 composite, the degradation experiments were carried out from pH 1 to 11 at 25 ± 2 °C. The pH of the organic pollutants (MB and FIP) was maintained by adding an aqueous solution of 0.2 M NaOH and 0.2 M HCl into the pollutant solutions. From **Figure 5.9a**, it is observed that the degradation efficiency of MB decreases at acidic pH and increases at basic pH, however, for FIP, a reverse trend was observed (degradation efficiency was maximum at acidic pH). The maximum degradation efficiency for MB (~90%) was observed at basic pH (pH 9) and this phenomenon is well explained by the studies of pH_{pzc} studies. The pH_{pzc} value for the composite of g-C_3N_4/H-ZSM-5 was determined and it was at pH 7.8 (**Figure 5.9b**),[16] which indicates that the surface of the g-C_3N_4/H-ZSM-5 composite can be negatively charged at pH > pH_{zpc} (i.e., pH>7.8) and become positively charged at pH<pH_{zpc} (i.e., pH<7.8). So at higher basic pH (pH>7.8), there will be an electrostatic attraction between the negative surface of the photocatalyst and cationic dye, MB.[17] Whereas the maximum photodegradation of FIP occurred at acidic pH (pH<7.8), suggests the electrostatic attractions between the positively surface of the photocatalyst and anionic pesticide, FIP.[18,19] Therefore, for the % degradation of FIP and MB pollutant, pH 4 and pH 9 were found to be highest at optimum conditions of time and dose i.e. 140 min, 0.12 g/L for FIP, and 120 min, 0.3 g/L for MB degradation.

5.3.3 Role of illuminating area

The role of the illuminating surface area for the photodegradation of MB was also studied under visible light irradiation (**Figure 5.9c**). It has been observed that the degradation efficiency increases with an increase in the illuminating area, as the area of organic pollutant which has been exposed to the visible light source is more. The distance of organic pollutants from the

visible light source was kept constant i.e., 10 cm away from the light source while performing the illuminating area experiments.

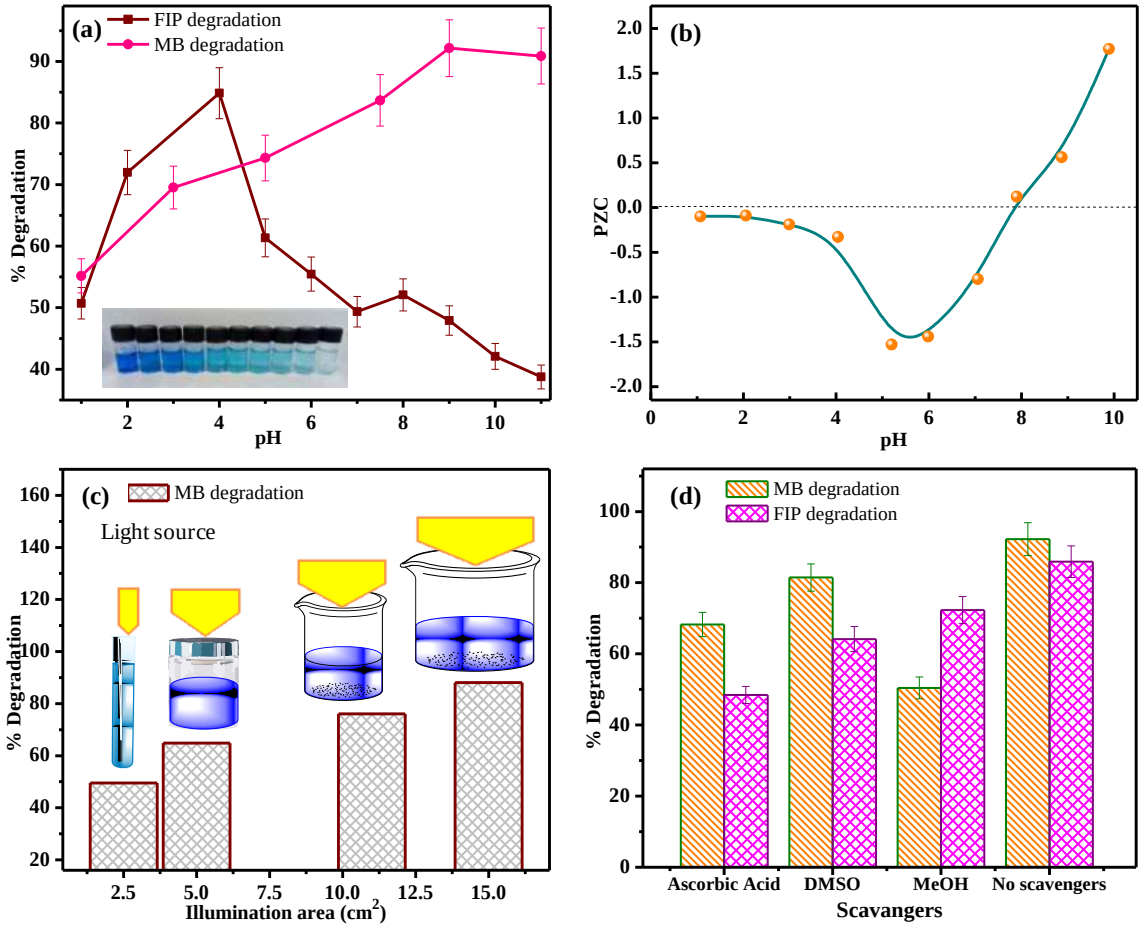

Figure 5.9: (a) Effect of pH on MB and FIP degradation [conditions: catalyst dose 0.3 g/L], (b) pH_{PZC} studies by g-C_3N_4/H-ZSM-5 photocatalyst, (c) effect of illumination area on MB degradation, and (d) effect of scavengers on MB and FIP degradation [concentration of scavengers: 10 mM (ascorbic acid, DMSO and MeOH), catalyst dose 0.3 g/L and 0.12 g/L for MB and FIP respectively].

5.3.4 Scavengers and reusability studies

To investigate the detailed plausible mechanism of organic pollutant degradation and to find out the main active species during photocatalysis, different scavengers were used to quench the corresponding active species. The scavengers used were: ascorbic acid for $O_2^{\bullet -}$ radicals, DMSO for scavenging e^-, and methyl alcohol for $^{\bullet}OH$ radicals.[20–22] The concentrations of

scavengers were also varied from 1mM to 20 mM (1mM, 10mM, and 20 mM) and it has been observed that, at 1 mM, the % degradation was decreased in each case compared with no scavenger condition. From **Figure 5.10a**, it has been investigated that there was also a significant decrease in % degradation of pollutant at 10 mM concentration however, at 20 mM, no significant difference was observed in % degradation. Therefore, to study the trapping experiment, 10 mM of scavengers were taken as an optimum dose. As shown in **Figure 5.9d**, with the addition of ascorbic acid, DMSO, and methanol as scavengers, the degradation of MB was reached approximately 71%, 81%, and 50%, respectively in 120 min with catalyst dose 0.3 g/L. However, in the absence of a scavenger, ~92% degradation was observed. From the experimental data, it is evident that MB degradation by g-C_3N_4/H-ZSM-5 composite is less affected by the addition of DMSO and ascorbic acid while majorly affected by methyl alcohol. That signifies that methanol inhibits the MB degradation and thereby $^{\bullet}OH$ radical is the major responsive species. In the same Figure, in the case of FIP, % degradation obtained due to the addition of ascorbic acid, DMSO, and methanol scavengers were ~ 48%, 64%, and 72%, respectively in 140 min with catalyst dose 0.12 g/L. While in the absence of scavenger, % degradation was ~86% at optimum conditions (time 140 min, dose 0.12 g/L) with g-C_3N_4/H-ZSM-5 composite. The experimental data (**Figure 5.9d**) shows that ascorbic acid majorly affects the rate of photodegradation of FIP as compared to DMSO and methanol, which confirms that, superoxide radical ($O_2^{\bullet-}$) is the major radical species for the degradation of FIP. So, the attained results suggested that $^{\bullet}OH$ and $O_2^{\bullet-}$ radical species were chiefly responsible for the photodegradation mechanism of MB and FIP pollutants, respectively.[23,24]

The experimental study on the reusability of the g-C_3N_4/H-ZSM-5 composite was also performed as one of the major post photodegradation issues, which is also necessary to test the stability and practical application of the photocatalyst. The stability and reusability of the g-C_3N_4/H-ZSM-5 composite were checked for four consecutive cycles with the photocatalytic degradation of MB. As shown in **Figure 5.10b**, the activity of the photocatalyst was found to be ~70% after 4 cycles which indicates that the catalyst can be reused several times and the catalyst is highly stable.

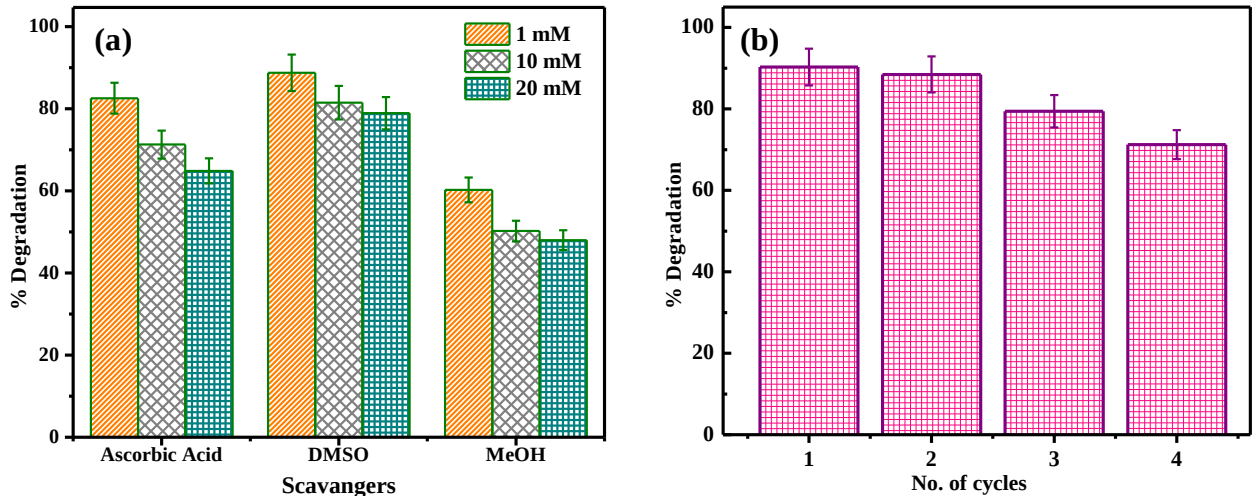

Figure 5.10: (a) Effect of scavengers concentration (1mM to 20 mM) on MB degradation, and (b) reusability studies of g-C_3N_4/H-ZSM-5 composite.

5.4 Plausible Mechanism for the photocatalytic reaction

In the plausible mechanism, the photocatalyst g-C_3N_4/H-ZSM-5 composite absorbs the visible light photons that direct the excitation of an electron from the valence band to the conduction band and create a hole (h^+) in the valence band. The electrons reached the conduction band react with the available dissolved molecular oxygen (O_2) present on the surface of the composite and generates superoxide anion radical.[20]

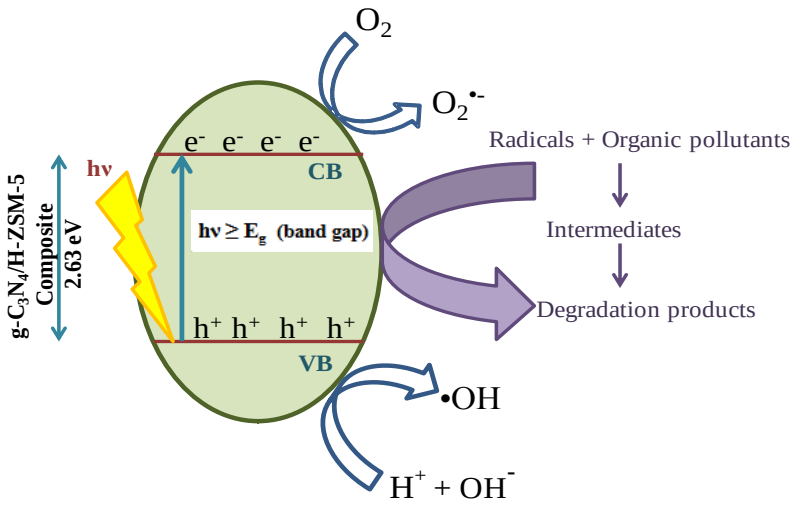

Scheme 5.2: Plausible photocatalytic degradation mechanism of pollutants by g-C_3N_4@zeolite composite.

The produced superoxide radical species i.e. $O_2^{\bullet -}$ promotes the direct oxidation of the pollutants. Also, the photo-generated holes (h^+) of the conduction band react with H_2O to give rise to $^{\bullet}OH$ radical and H^+ ion. These, hydroxyl and superoxide radicals were concluded to be responsible species for the photodegradation of MB and FIP pollutants. The following mechanism may be responsible for the photocatalytic degradation of organic pollutants MB and FIP (**Equation 5.2-5.6**) as described in **Scheme 5.2**.

$$g\text{-}C_3N_4/H\text{-}ZSM\text{-}5 \xrightarrow{h\nu} e^-_{(CB)} + h^+_{(VB)} \quad (5.2)$$

$$e^-_{(CB)} + O_2 \xrightarrow{h\nu} O_2^{\bullet -} \quad (5.3)$$

$$h^+_{(VB)} + H_2O \rightarrow H_2O^+ \rightarrow {}^{\bullet}OH + H^+ \quad (5.4)$$

$$H_2O \rightarrow OH^- + H^+ \quad (5.5)$$

$$h^+ + OH^- \rightarrow {}^{\bullet}OH \quad (5.6)$$

$^{\bullet}OH + O_2^{\bullet -}$ + Dye/Pesticide → degraded or mineralized products

From the studies, it is evident that the very small amount of g-C_3N_4/H-ZSM-5 composite was sufficient to degrade toxic dye and pesticide very efficiently under visible/sunlight irradiation. Therefore, this prepared catalyst can be used as an alternative photocatalyst for the degradation purposes of toxic pollutants.

5.5 Conclusions

The composite of g-C_3N_4/H-ZSM-5 was successfully synthesized from Melamine and H-ZSM-5 zeolite. The photocatalytic degradation experiments of MB and FIP were carried out to investigate the activity of the prepared composite. The composite, g-C_3N_4/H-ZSM-5 was characterized by XRD, BET, HRTEM, FESEM, EDS, and XPS analysis. The bandgap of the g-C_3N_4/H-ZSM-5 composite was calculated by Tauc's plot which lies in the visible range of the solar spectrum. The surface area of the composite is greater than the pure pristine g-C_3N_4 which leads to better degradation of the pollutants. Under visible light and sunlight irradiation, the photodegradation of MB and FIP by the g-C_3N_4/H-ZSM-5 composite was greater than that of g-C_3N_4 alone. The degradation mechanism was proposed and discussed in terms of energy band and radicals.

References

(1) Mishra, A.; Mehta, A.; Kainth, S.; Basu, S. Effect of G-C_3N_4 Loading on TiO_2/Bentonite Nanocomposites for Efficient Heterogeneous Photocatalytic Degradation of Industrial Dye under Visible Light. *J. Alloys Compd.* **2018**, *764*, 406–415. https://doi.org/10.1016/j.jallcom.2018.06.089.

(2) Gogoi, G.; Keene, S.; Patra, A. S.; Sahu, T. K.; Ardo, S.; Qureshi, M. Hybrid of G-C_3N_4 and MoS_2 Integrated onto $Cd_{0.5}Zn_{0.5}S$: Rational Design with Efficient Charge Transfer for Enhanced Photocatalytic Activity. *ACS Sustain. Chem. Eng.* **2018**, *6* (5), 6718–6729. https://doi.org/10.1021/acssuschemeng.8b00512.

(3) Yuan, X.; Zhou, C.; Jin, Y.; Jing, Q.; Yang, Y.; Shen, X.; Tang, Q.; Mu, Y.; Du, A. K. Facile Synthesis of 3D Porous Thermally Exfoliated G-C_3N_4 Nanosheet with Enhanced Photocatalytic Degradation of Organic Dye. *J. Colloid Interface Sci.* **2016**, *468*, 211–219. https://doi.org/10.1016/j.jcis.2016.01.048.

(4) De Rivas, B.; Sampedro, C.; Ramos-Fernández, E. V.; López-Fonseca, R.; Gascon, J.; Makkee, M.; Gutiérrez-Ortiz, J. I. Influence of the Synthesis Route on the Catalytic Oxidation of 1,2-Dichloroethane over CeO_2/H-ZSM5 Catalysts. *Appl. Catal. A Gen.* **2013**, *456*, 96–104. https://doi.org/10.1016/j.apcata.2013.02.026.

(5) Mousavi, M.; Habibi-Yangjeh, A. Magnetically Recoverable Highly Efficient Visible-Light-Active g-C_3N_4/Fe_3O_4/Ag_2WO_4/AgBr Nanocomposites for Photocatalytic Degradations of Environmental Pollutants. *Adv. Powder Technol.* **2018**, *29* (1), 94–105. https://doi.org/10.1016/j.apt.2017.10.016.

(6) Bakshi, M. S.; Thakur, P.; Sachar, S.; Kaur, G.; Banipal, T. S.; Possmayer, F.; Petersen, N. O. Aqueous Phase Surfactant Selective Shape Controlled Synthesis of Lead Sulfide Nanocrystals. *J. Phys. Chem. C* **2007**, *111* (49), 18087–18098. https://doi.org/10.1021/jp075477c.

(7) Monga, D.; Basu, S. Enhanced Photocatalytic Degradation of Industrial Dye by G-C_3N_4 /TiO_2 Nanocomposite: Role of Shape of TiO_2. *Adv. Powder Technol.* **2019**, *30* (5), 1089–1098. https://doi.org/10.1016/j.apt.2019.03.004.

(8) Rather, R. A.; Singh, S.; Pal, B. A C_3N_4 Surface Passivated Highly Photoactive Au-TiO2 Tubular Nanostructure for the Efficient H_2 Production from Water under Sunlight Irradiation. *Appl. Catal. B Environ.* **2017**, *213*, 9–17. https://doi.org/10.1016/j.apcatb.2017.05.002.

(9) Wang, Z.; Xu, Q.; Meng, T.; Ren, T.; Chen, D. Preparation and Characterization of CdS/TiO_2 –Mt Composites with Enhanced Visible Light Photocatalytic Activity . *Energy Environ. Focus* **2018**, *4* (2), 149–156. https://doi.org/10.1166/eef.2015.1150.

(10) Li, H.; Zhou, L.; Wang, L.; Liu, Y.; Lei, J.; Zhang, J. In Situ Growth of TiO_2 Nanocrystals on G-C_3N_4 for Enhanced Photocatalytic Performance. *Phys. Chem. Chem. Phys.* **2015**, *17* (26), 17406–17412. https://doi.org/10.1039/c5cp02554k.

(11) Cao, Y.; Li, Q.; Wang, W. Construction of a Crossed-Layer-Structure MoS_2/g-C_3N_4 Heterojunction with Enhanced Photocatalytic Performance. *RSC Adv.* **2017**, *7* (10), 6131–6139. https://doi.org/10.1039/c6ra26925g.

(12) Li, Z.; Jiang, G.; Zhang, Z.; Wu, Y.; Han, Y. Phosphorus-Doped g-C_3N_4 Nanosheets Coated with Square Flake-like TiO_2: Synthesis, Characterization and Photocatalytic Performance in Visible Light. *J. Mol. Catal. A Chem.* **2016**, *425*, 340–348. https://doi.org/10.1016/j.molcata.2016.10.020.

(13) Li, K.; Huang, Z.; Zeng, X.; Huang, B.; Gao, S.; Lu, J. Synergetic Effect of Ti^{3+} and Oxygen Doping on Enhancing Photoelectrochemical and Photocatalytic Properties of TiO_2/g-C_3N_4 Heterojunctions. *ACS Appl. Mater. Interfaces* **2017**, *9* (13), 11577–11586. https://doi.org/10.1021/acsami.6b16191.

(14) Zhang, Z.; Liu, K.; Feng, Z.; Bao, Y.; Dong, B. Hierarchical Sheet-on-Sheet $ZnIn_2S_4$/g-C_3N_4 Heterostructure with Highly Efficient Photocatalytic H_2 Production Based on Photoinduced Interfacial Charge Transfer. *Sci. Rep.* **2016**, *6* (1), 19221. https://doi.org/10.1038/srep19221.

(15) Ge, L.; Zuo, F.; Liu, J.; Ma, Q.; Wang, C.; Sun, D.; Bartels, L.; Feng, P. Synthesis and Efficient Visible Light Photocatalytic Hydrogen Evolution of Polymeric G-C_3N_4 Coupled with CdS Quantum Dots. *J. Phys. Chem. C* **2012**, *116* (25), 13708–13714. https://doi.org/10.1021/jp3041692.

(16) Prakash, K.; Karuthapandian, S.; Senthilkumar, S. Zeolite Nanorods Decorated G-C_3N_4 Nanosheets: A Novel Platform for the Photodegradation of Hazardous Water Contaminants. *Mater. Chem. Phys.* **2019**, *221*, 34–46. https://doi.org/10.1016/j.matchemphys.2018.09.026.

(17) Gürses, A.; Doğar, Ç.; Yalçin, M.; Açikyildiz, M.; Bayrak, R.; Karaca, S. The Adsorption Kinetics of the Cationic Dye, Methylene Blue, onto Clay. *J. Hazard. Mater.* **2006**, *131* (1–3), 217–228. https://doi.org/10.1016/j.jhazmat.2005.09.036.

(18) Xu, J.; Wang, L.; Zhu, Y. Decontamination of Bisphenol A from Aqueous Solution by Graphene Adsorption. *Langmuir* **2012**, *28* (22), 8418–8425. https://doi.org/10.1021/la301476p.

(19) Goyal, N.; Barman, S.; Bulasara, V. K. Quaternary Ammonium Salt Assisted Removal of Genistein and Bisphenol S from Aqueous Solution by Nanozeolite NaY: Equilibrium, Kinetic and Thermodynamic Studies. *J. Mol. Liq.* **2016**, *224*, 1154–1162. https://doi.org/10.1016/j.molliq.2016.10.088.

(20) Wang, D.; Duan, Y.; Luo, Q.; Li, X.; An, J.; Bao, L.; Shi, L. Novel Preparation Method for a New Visible Light Photocatalyst: Mesoporous TiO_2 Supported Ag/AgBr. *J. Mater. Chem.* **2012**, *22* (11), 4847–4854. https://doi.org/10.1039/c2jm14628b.

(21) Islam Molla, M. A.; Tateishi, I.; Furukawa, M.; Katsumata, H.; Suzuki, T.; Kaneco, S. Evaluation of Reaction Mechanism for Photocatalytic Degradation of Dye with Self-Sensitized TiO_2 under Visible Light Irradiation. *Open J. Inorg. Non-metallic Mater.* **2017**,

07 (01), 1–7. https://doi.org/10.4236/ojinm.2017.71001.

(22) Pelaez, M.; Falaras, P.; Likodimos, V.; O'Shea, K.; de la Cruz, A. A.; Dunlop, P. S. M.; Byrne, J. A.; Dionysiou, D. D. Use of Selected Scavengers for the Determination of NF-TiO_2 Reactive Oxygen Species during the Degradation of Microcystin-LR under Visible Light Irradiation. *J. Mol. Catal. A Chem.* **2016**, *425*, 183–189. https://doi.org/10.1016/j.molcata.2016.09.035.

(23) Mittal, M.; Gupta, A.; Pandey, O. P. Role of Oxygen Vacancies in Ag/Au Doped CeO_2 Nanoparticles for Fast Photocatalysis. *Sol. Energy* **2018**, *165*, 206–216. https://doi.org/10.1016/j.solener.2018.03.033.

(24) Zhang, C.; Li, Y.; Shuai, D.; Shen, Y.; Xiong, W.; Wang, L. Graphitic Carbon Nitride (g-C_3N_4)-Based Photocatalysts for Water Disinfection and Microbial Control: A Review. *Chemosphere* **2019**, *214*, 462–479. https://doi.org/10.1016/j.chemosphere.2018.09.137.

Chapter 6: Adsorptive removal of fipronil by CeO_2 modified zeolites, and their structural properties

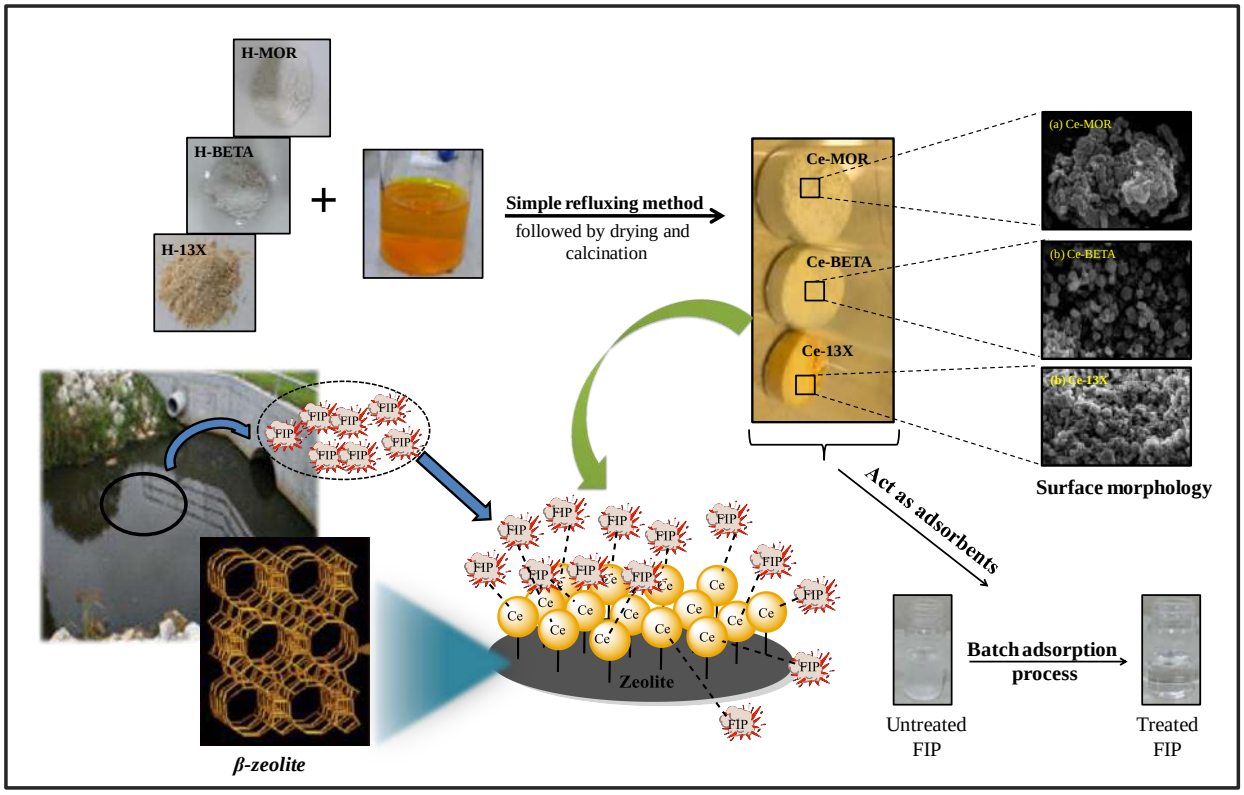

Highlights

- BETA, MOR and 13X zeolites modified with cerium by ion-exchange method.
- Adsorption mediated experiments possess high removal efficiency of FIP insecticide.
- Ce-BETA zeolite possesses a maximum adsorption capacity of 632 mg/g than others.
- Langmuir adsorption isotherm and Pseudo second order kinetics fit properly.
- Fipronil adsorption was a spontaneous and exothermic process.

6.1 Preparation of cerium modified adsorbents

The specific adsorbent was prepared with large pore zeolites such as Beta, Mordenite, and 13X zeolites by modifying with rare earth metal cerium. The cerium-modified zeolites (Ce-zeolites) were used to eliminate noxious FIP pollutants. Firstly, 13X zeolite gets converted into ammonium-form by refluxing with NH_4NO_3 solution at 363K for 6h[1] then calcined at 623K, and repeated 3 times. After washing and drying, the H-form of 13X zeolite was ready for use. Commercial ammonium mordenite (H-MOR), ammonium beta (H-BETA), H-13X zeolite were refluxed individually with 25 wt% of ammonium cerium (IV) nitrate aqueous solution in a refluxing system at 375K for 24h and designated as Ce-MOR, Ce-BETA, and Ce-13X respectively.[2] The prepared adsorbents were then washed 3-4 times by distilled water and crystallized in an oven at 393K for 14h and then placed in a furnace for 4h at 723K to eradicate the unwanted ions.[3] The general procedure of zeolite modification is schematically depicted in **Scheme 6.1**.

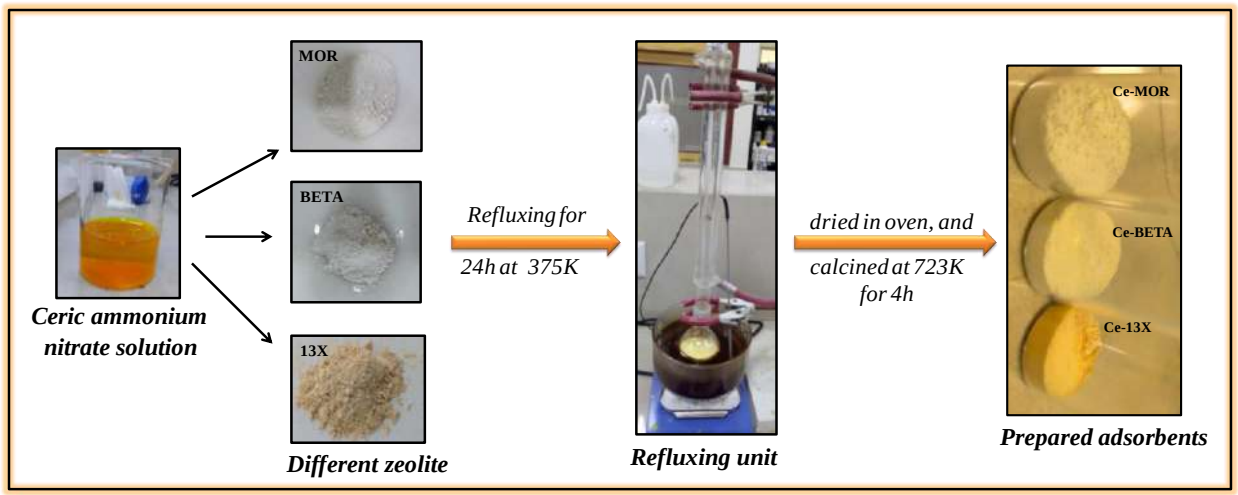

Scheme 6.1: Schematic representation of prepared Ce-zeolites (Ce-MOR, Ce-BETA, Ce-13X).

6.2 Characterization of adsorbents

6.2.1 XRD analysis

The XRD patterns of freshly prepared zeolite were shown in **Figure 6.1**. The peaks of CeO_2 in the XRD spectrum of Ce-MOR, Ce-BETA, and Ce-13X zeolites, indicate that the cerium modification was productively materialized over the surface of the zeolite. The XRD patterns of different unmodified/pure zeolites and corresponding Ce-zeolites were shown in **Figure 6.1**. The peaks of cerium oxide are marked with the asterisk symbol (*) in XRD spectra

of modified zeolites and the rest of the peaks match with the corresponding parent zeolite. The 2θ values of marked peaks of CeO_2 were matched with JCPDS No. 34-0394 which corresponds to the crystalline fcc (face-centered cubic) phase of cerium oxide and these values for Ce-BETA are 28.62°, 33.32°, 47.53°, 56.25°, 69.40°, 76.77°, and 79.08° corresponds to (111), (200), (220), (311), (400), (331), and (420), respectively. However, Ce-MOR peaks are approximately at 2θ = 28.47°, 33.32°, 47.49°, 56.16°, 69.68°, 76.77°, and 78.98° for the planes of (111), (200), (220), (311), (400), (331), and (420), respectively. The peaks of Ce-13X zeolite with their corresponding planes are 28.64° (111), 33.33° (200), 47.53° (220), 56.28° (311), 69.40° (400), 76.67° (331), and 78.98° (420). The average crystallite size (D) of cerium oxide (CeO_2) was determined from the four intense XRD peaks of CeO_2. The 'D' was evaluated using the Debye-Scherrer formula, written in **Equation 6.1**:

$$D = \frac{0.9\,\lambda}{\beta\,cos\theta} \tag{6.1}$$

Where 'λ' is the wavelength of Cu Kα radiations used for the XRD analysis, 'β' is the full width at half maximum (FWHM), and 'θ' is the angle of diffraction for (111), (200), (220), and (311), planes in case of Ce-BETA, Ce-MOR, and Ce-13X zeolite.[2,4] According to this formula, the average crystallite size of CeO_2 was found to be 6.67 nm, 6.42 nm, and 4.48 nm for Ce-BETA, Ce-MOR, and Ce-13X zeolite, respectively. This result depicts that the CeO_2 incorporated into the different zeolites was within the nanometer range.

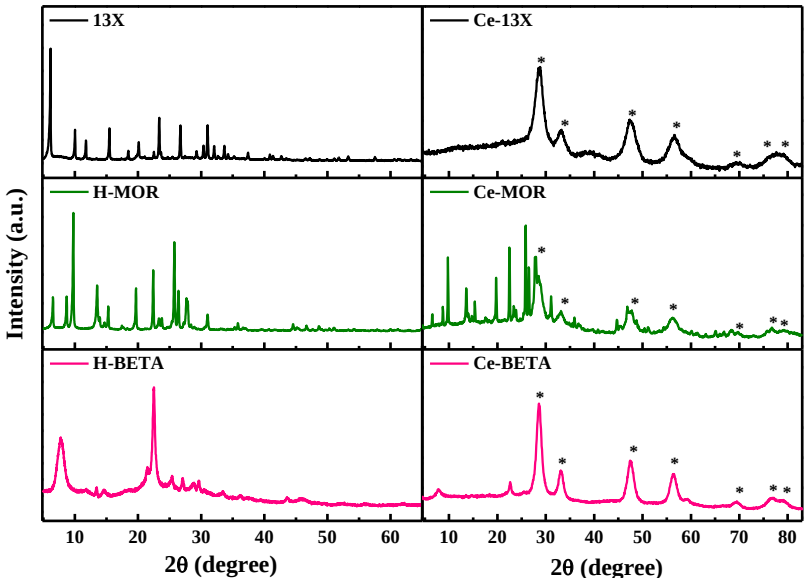

Figure 6.1: XRD pattern of zeolites (13X, H-MOR, H-BETA), and Ce-modified zeolites (Ce-13X, Ce-MOR, Ce-BETA).

6.2.2 N_2 adsorption-desorption isotherms

Figure 6.2a depicts the N_2 adsorption-desorption isotherms for H-MOR, H-BETA, H-13X zeolite, whereas isotherms for Ce-zeolites (Ce-MOR, Ce-BETA, Ce-13X) were shown in **Figure 6.2b**. Ce-BETA exhibits type-IV isotherm along with a hysteresis loop of H2-type,[5] which signifies the presence of mesopores in Ce-BETA. While other modified and unmodified zeolites (Ce-MOR, Ce-13X, H-MOR, H-BETA, H-13X) also possess a hysteresis loop followed by type-IV isotherm. The mesopores present in the modified zeolite are contributing to better adsorption of organic pollutants. It is well explained based on the surface area, as Ce-BETA having a higher surface area that results in maximum %adsorptive removal compared to other adsorbents. The BET surface area (S.A.) of Ce-MOR, Ce-BETA, and Ce-13X were obtained to be 320, 343, and 126 m^2/g, respectively, and tabulated in **Table 6.1**. The Ce-BETA adsorbent posses higher pore volume which leads to maximum FIP removal. The BJH plots for the Ce-zeolites were shown in the insets of **Figure 6.2b**.

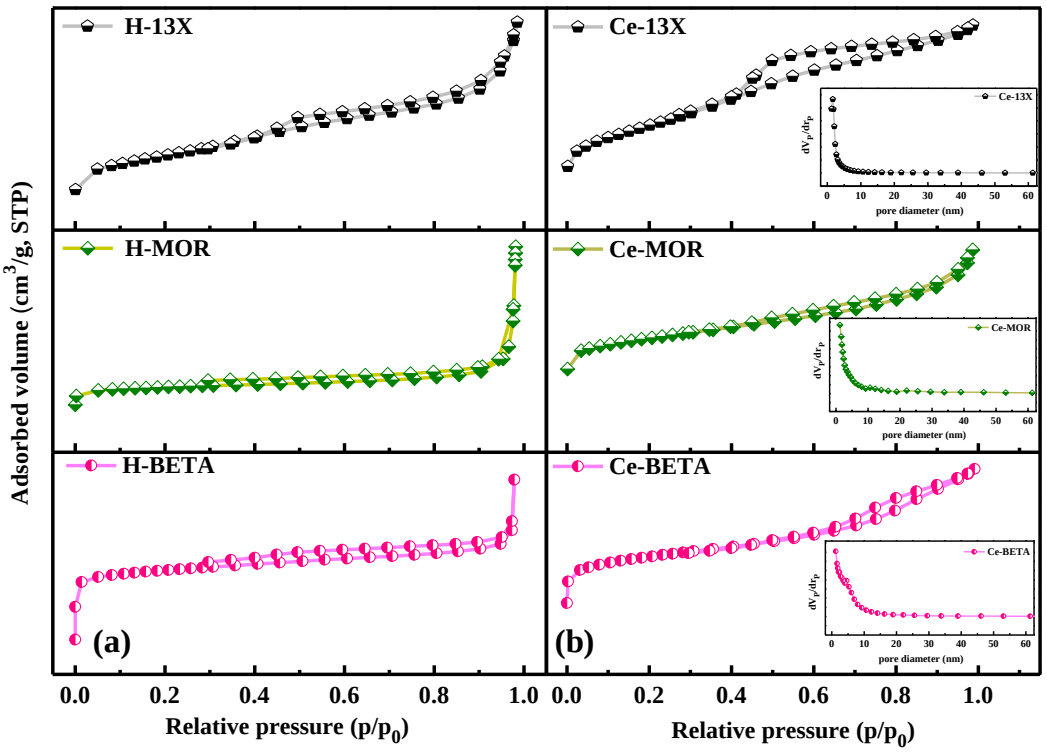

Figure 6.2: Nitrogen adsorption-desorption BET loops of (a) H-13X, H-MOR, H-BETA; (b) Ce-13X, Ce-MOR, Ce-BETA (insets contains BJH plots).

Table 6.1: Surface properties of the various adsorbents.

Adsorbents	BET surface area (m^2/g)	Total pore volume (cm^3/g)	Mean pore diameter (nm)
H-MOR	500	0.289	2.68
H-BETA	693	0.476	4.49
13X	475	0.280	6.63
Ce-MOR	320	0.258	3.23
Ce-BETA	343	0.283	3.29
Ce-13X	126	0.127	4.01
After adsorption Ce-BETA	328	0.241	2.93

6.2.3 SEM-EDS analysis

The SEM (Scanning Electron Microscope) of Ce-zeolites in **Figure 6.3a-c** shows rough surfaces of different morphologies. Ce-MOR (**Figure 6.3a**) has an elongated structure with irregular and agglomerated crystals. However, Ce-BETA (**Figure 6.3b**) shows the regular distribution of uniform and small spherical kinds of crystals which comprise enormous porosity and roughness on its surface. The SEM analysis of Ce-13X zeolite (**Figure 6.3c**) confirms the existence of large crystals and porous nature as compared to another two modified zeolites (Ce-MOR, Ce-BETA). Gives the idea of the smaller the size of the crystal with roughness, the higher will be the surface area. From the SEM analysis, the particle size of modified BETA zeolite was observed in the range of 0.6-0.9 μm.[6] While in the case of Ce-MOR and Ce-13X zeolite the particle sizes ranged between 0.1-0.4 μm and 2-4 μm, respectively. From this characterization, it can be summarized that Ce-BETA is found to be highly porous having uniform shaped crystals with a higher surface area which gives maximum absorption.

The EDS spectra determine the composition of Ce-MOR, Ce-BETA, and Ce-13X zeolite in Figure 6.3d-f respectively. The peaks of various elements confirmed the presence of aluminum (Al), silicon (Si), oxygen (O), and cerium (Ce) in Ce-zeolites. After evaluating the regions under the peaks of individual elements, the corresponding elemental composition can be determined. The peaks of cerium in the EDS spectrum also support that the modification takes place in the crystal lattice of different zeolites.

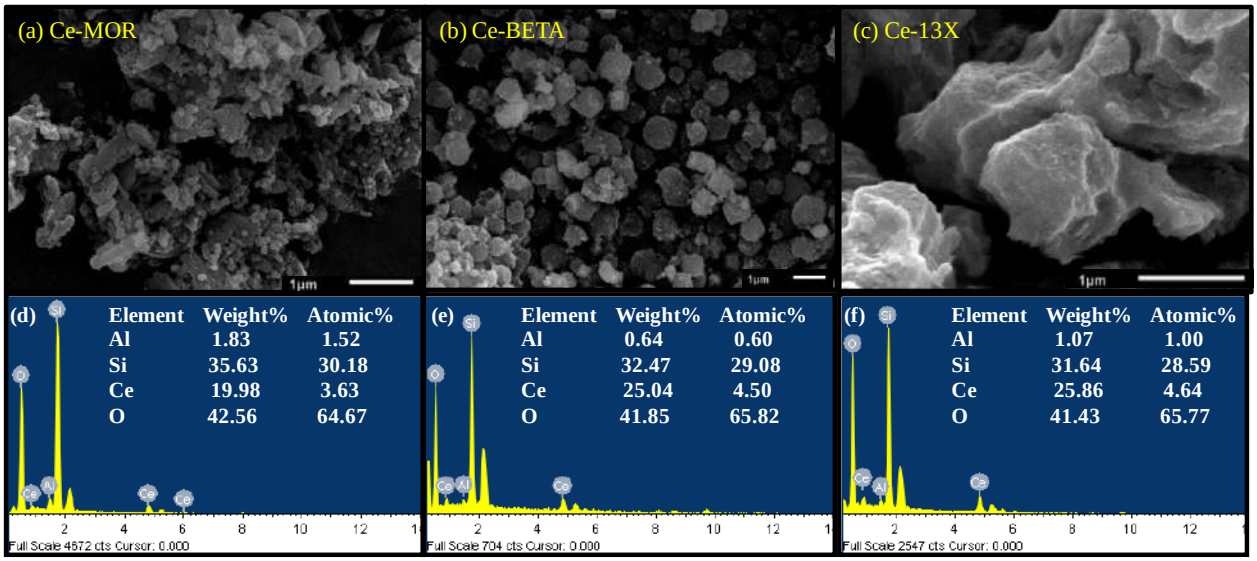

Figure 6.3: SEM-EDS results of (a,d) Ce-MOR, (b,e) Ce-BETA, and (c,f) Ce-13X zeolite.

The peaks of Si and Al are present in the EDS spectrum, which confirms that the basic composition of parent zeolites remains intact even after the modifications. This also revealed that the ion-exchange method doesn't affect the framework of zeolite which promotes the adsorption process. To authenticate the homogenous scattering of the cerium and oxygen in the zeolite, elemental color mapping of Al, Si, Ce, and O elements was done and shown in **Figure 6.4**.

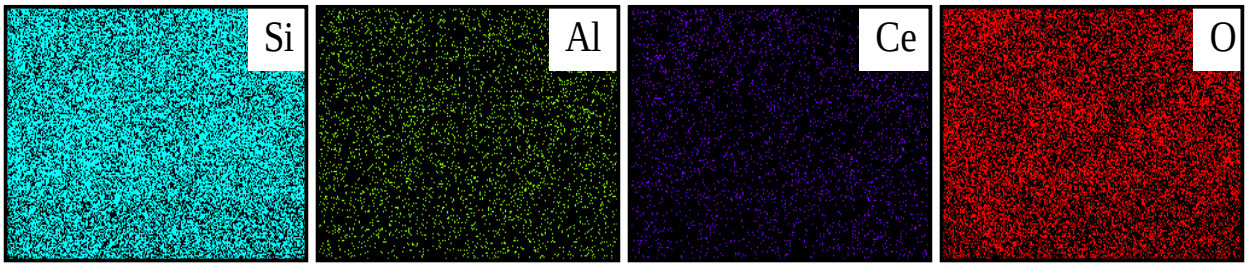

Figure 6.4: Elemental mapping of Ce-BETA showing the elemental distribution of Si, Al, Ce, and O.

6.2.4 HR-TEM analysis

HR-TEM measures the diffraction intensities quantitatively by CMOS (Complementary Metal Oxide Semiconductor) camera and analyzes the structural frameworks (d-spacing and planes) of zeolite as well as materials incorporated in their micropores. In the present work, the HRTEM image (Figure 4) shows the surface morphology and fabrication of CeO_2 (darker area)

over the zeolite framework and also describes the mesoporous nature of the prepared material. The cerium oxide particles are spherical with a darker area in **Figure 6.5a**. The d-spacing values were calculated from **Figure 6.5b (**inset contains the magnified view**)** that corresponds to (111), (200), (220), (311) planes and these planes are also in conformity with the XRD data as described in section 3.1.2. The mentioned values and planes are shown in **Figure 6.5b** and calculated from SAED (Selected Area Electron Diffraction) pattern (**Figure 6.5c**) following the JCPDS No. 34-0394,[7] which indicates the successful fabrication of cerium oxide particles over the zeolite.

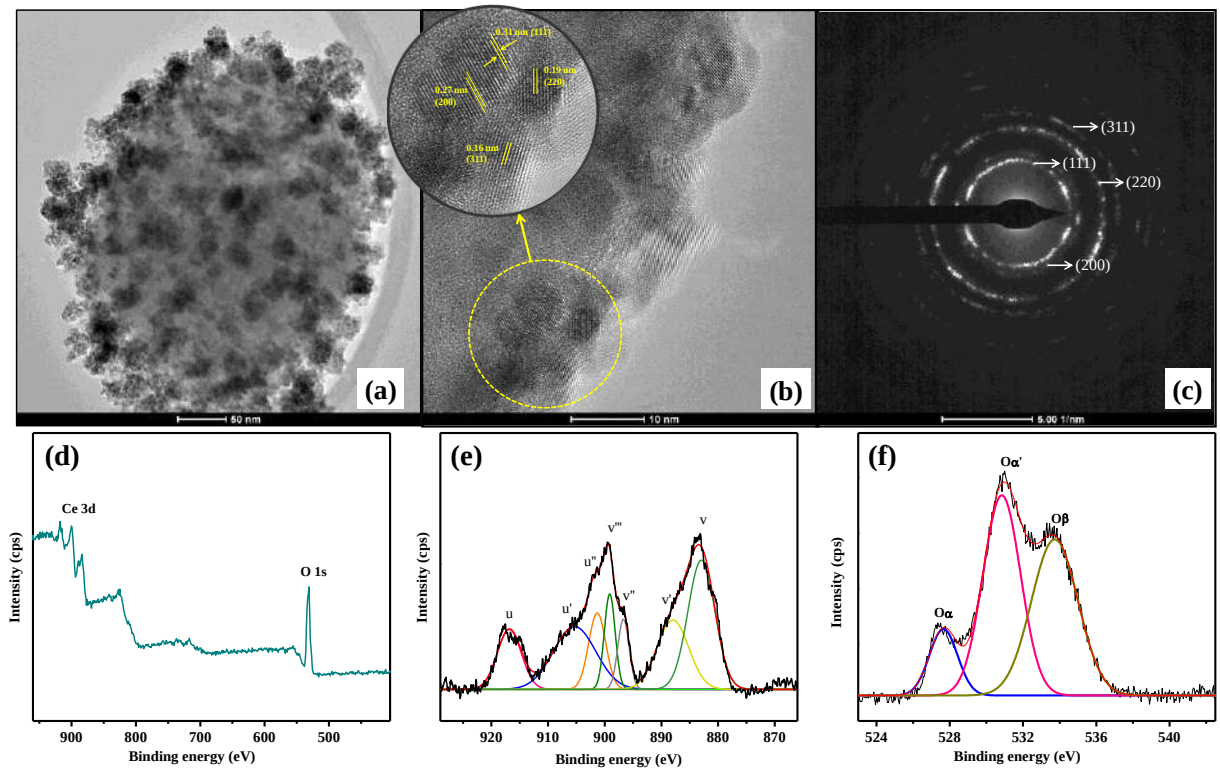

Figure 6.5: HR-TEM analysis (a) of Ce-BETA zeolite (b) cerium particle distribution (inset contains d-spacing and lattice fringes) (c) SAED pattern of CeO_2; XPS analysis (d) survey spectrum of Ce-BETA zeolite, (e) Cerium (Ce 3d), (f) Oxygen (O 1s) elements.

6.2.5 XPS analysis

XPS technique was adopted to study the chemical oxidation states of cerium present in the Ce-BETA zeolite. The survey spectrum depicted in **Figure 6.5d** includes the peaks of cerium and oxygen. This complex spectrum of cerium can be deconvoluted into seven

components that were produced by the splitting: Ce $3d_{3/2}$ and Ce $3d_{5/2}$ and other states after reduction (**Figure 6.5e**). The region of the Ce 3d spectrum is grouped linearly to show various oxidation states of cerium oxides. The XPS peaks positioned at 916.9, 901.3, 897.6, 888.7, 882.9 eV are ascribed for the Ce^{4+} oxidation state and designated as spin-orbital splitting peaks [8]. The sub-peaks were labeled as u, v, v', u" and v" for Ce(IV) with an initial electronic configuration of $3d^{10}$ $4f^{0}$. Whereas the Ce^{3+} oxidation state is described by the two peaks whose values are 904.7 and 899.2 eV. These two sub-peaks are labeled as u' and v'" with $3d^{10}4f^{1}$ initial electronic configuration.[9] This data suggests that the cerium exists in two oxidation states with mixed valance states of Ce(IV) and Ce(III) in Ce-BETA zeolite. The amount of Ce^{4+} and Ce^{3+} was calculated from the **Equations** (**6.1** and **6.2**) as follows:

Ce(IV) = u+v+v'+u"+v"

Ce(III) = u'+v'"

$$\mathrm{Ce(IV)} = \frac{\mathrm{Ce(IV)}}{\mathrm{Ce(IV)} + \mathrm{Ce(III)}} \mathrm{x100\%} \qquad (6.1)$$

$$\mathrm{Ce(III)} = \frac{\mathrm{Ce(III)}}{\mathrm{Ce(IV)} + \mathrm{Ce(III)}} \mathrm{x100\%} \qquad (6.2)$$

The weight % calculated was 71.10% and 28.29% for Ce(IV) and Ce(III), respectively. This concludes that Ce-BETA zeolite contains cerium in +4 oxidation state (CeO_2).[10,11] Moreover, the spectrum of oxygen (O 1s) containing 3 peaks (**Figure 6.5f**), one of which explains lattice oxygen (O^{2-}) of binding energy value ~527.8 eV (denoted by O_α),[12] another two peaks are allotted to exteriorly adsorbed oxygen (on the surface) represented by O_α' (~530.9 eV) which belongs to defect metal oxide or surface hydroxyl-type species, along with O_β (~533.7 eV) which referred to chemisorbed water molecules.[11]

6.3 Insecticide FIP adsorption performance

6.3.1 Effect of initial FIP concentration

To investigate the results of different concentrations of insecticide (FIP) over Ce-zeolites, experiments were carried out within 600-1000 ppm FIP solution. The %removal of fipronil was decreased from 64.2% to 45.4% for Ce-BETA; 60.4% to 42.7% for Ce-MOR and 48.5% to 33.6% for Ce-13X, with increased concentrations **(Figure 6.6a)**. At 1000 ppm

concentration, there was early attainment of equilibrium as the driving force created at this concentration made the accessible adsorption sites of adsorbents saturated by FIP molecules. It is evident from the figure that Ce-zeolites have maximum %removal at 600 ppm of FIP solution and was chosen as optimum concentration.

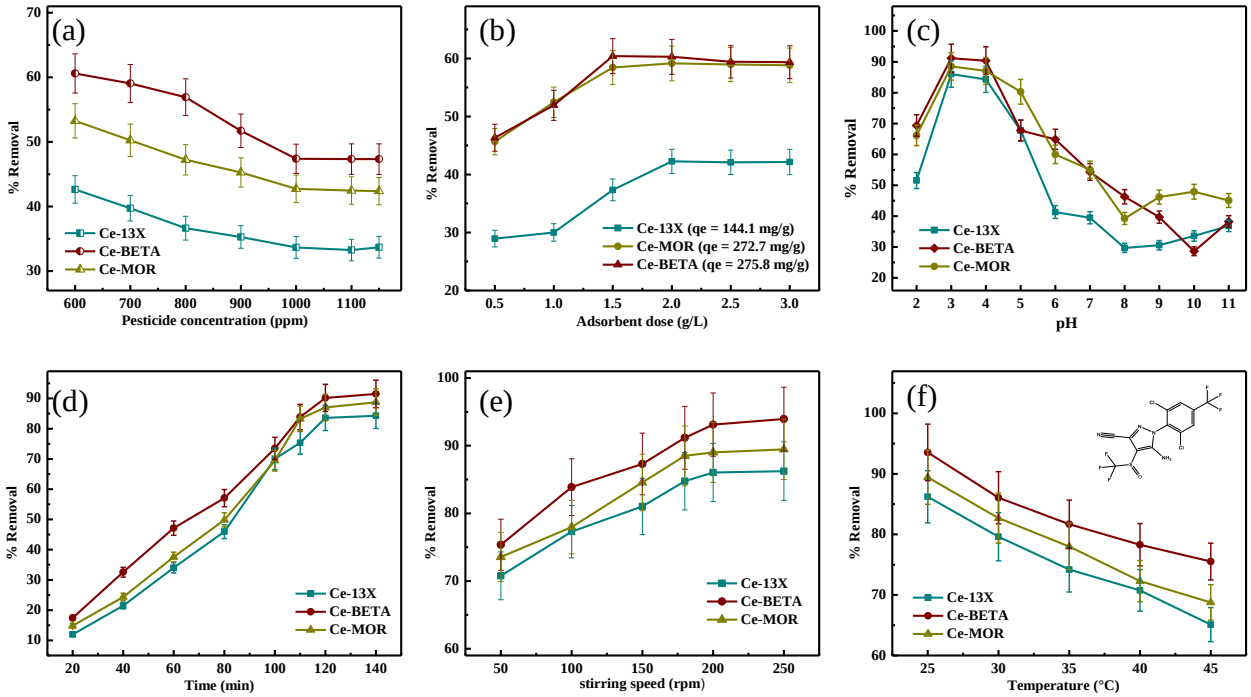

Figure 6.6: Plots for the effects of: (a) FIP conc [150min, adsorbent conc:2g/L], (b) Ce-zeolites (adsorbents) dose(g/L) [FIP conc:600ppm, 150min], (c) pH [dose:1.5-2.0g/L, 600 ppm], (d) contact time [1.5-2.0g/L, pH3, temp:25°C, 600ppm] (e) stirring speed [1.5-2.0g/L, 140min, pH3], (f) temperature [1.5-2.0g/L, 140min, pH3, rpm:250] (inset contains FIP structure).

6.3.2 Effect of adsorbent dose

The effects of doses of adsorbents were explored by shaking the contents for 150 min. In the case of Ce-BETA and Ce-MOR (in **Figure 6.6b**), the %removal of FIP was 60% and 58% respectively at 1.5g/L of adsorbent dose, afterward, it becomes almost steady. Whereas, Ce-13X zeolite gave 42% removal at 2g/L of adsorbent dose. This indicates that with increased adsorbent dose there is more accessibility of porous area with a higher number of exchangeable sites that gave higher %removal. Whereas after equilibrium attainment, the FIP molecules were unable to get adsorbed on all vacant adsorption sites due to turbidity arises in the medium,[13] so the above-mentioned doses were selected as optimal amount.

6.3.3 Effect of pH

Removal of EDCs by adsorption is majorly based on the pH of the pollutant's solution.[13] The adsorption of FIP over Ce-zeolites was investigated in the series of pH2-pH11 for 150 min. The pH range was chosen from 2-11 because above this range that is at extreme basic conditions the dissolution of Al and Si starts occurring.[14] And at very acidic conditions silica undergoes precipitation that will lead to the zeolite framework distortion.[15] From **Figure 6.6c**, the %removal of FIP on Ce-zeolites decreases as pH increases which are similar to our previous studies.[2] The maximum adsorption for FIP removal by Ce-zeolites observed in acidic medium (pH~3). Because at this acidic pH the FIP-adsorbent interaction increases, as a result, elimination of FIP pollutant increases.[16] The pH has a significant role in influencing the chemistry of the Ce-zeolites adsorbents. The PZC (zero point charge) value of Ce-BETA zeolite adsorbent was found to be in the range of 4.1-4.5 experimentally (**Figure 6.7**) following the PZC values of CeO_2 and beta zeolite,[13,17] the adsorbent act as a positive surface below this value and can easily attract negatively charged pollutant. While the adsorbent acts as a negative surface above this value and can attract positively charged pollutants which leads to electrostatic interactions. Therefore for maximum FIP removal, acidic pH (3-4) was chosen as optimum pH.

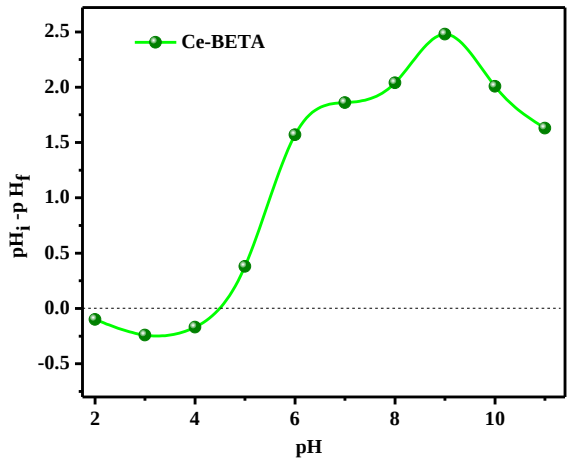

Figure 6.7: The PZC study of Ce-BETA adsorbent.

6.3.4 Effect of time of contact

To know the adsorptive competence of different adsorbents, the effects of contact time were investigated over Ce-zeolites (**Figure 6.6d**) from 0 to 140 min. The contact time was divided into 3 stages. From (0-80 min) initial stage, the graph rises constantly and reaches ~58%

removal. From (80-120 min) second stage, the graph increases drastically leading to the highest removal of ~90% removal. At the final stage above 120 min, there is not as such increase in % removal which indicates the attainment of the equilibrium state.[18] The %removal of FIP increases with an increase in the contact time of adsorbent with FIP pollutant. The Ce-zeolite significantly attains equilibrium in 120-140 min, which was following our previous study [2]. For Ce-BETA and Ce-MOR with 1.5g/L and Ce-13X with 2g/L dose, the adsorption reaches equilibrium within 140 min. So, the optimum adsorption time was confined to 140 min for Ce-zeolites. This effect was studied at optimum pH3, FIP concentration 600 ppm, and corresponding adsorbent dose.

6.3.5 Effect of stirring speed

The stirring speed was varied to investigate its effect on the %removal of FIP over Ce-zeolites. The adsorption tests were executed at optimum conditions like pH3, dose: 2g/L, time: 140 min for Ce-13X and Ce-BETA, and Ce-MOR dose: 1.5g/L. The stirring speed parameter was studied in the range of 50-250 rpm. **Figure 6.6e** shows that %removal increases with the increase in stirring speed and it rises to the speed of 200 rpm but above this speed, removal decreases. With a higher rotation rate the possibility of interaction of pollutant species with Ce-zeolite adsorbent increases that eases FIP moieties to conquer the film diffusion resistance.[13,19] At 250 rpm, there is no significant increase in %removal because of the non-accessibility of active channels for FIP molecules to interact. Therefore, 200 rpm was considered as optimal shaking speed.

6.3.6 Effect of temperature

The effect of temperature for FIP removal on Ce-zeolites is shown in **Figure 6.6f**. The experiments were performed in the series from 25 -45°C at optimum conditions (i.e. initial concentration: 600ppm, Ce-zeolite dose: 1.5-2g/L, pH3, time of contact: 140 minutes, stirring rate: 200 rpm). With an increase in temp, FIP removal decreases that indicates the exothermic nature of the adsorption process. The maximum %removal (adsorption capacity 420 mg/g) was achieved at 25°C which depicts that FIP molecules got sufficient energy at 25°C to be adsorbed at vacant sites of porous zeolite adsorbents. At higher temperatures, the electrostatic interactions of FIP molecules with adsorption channels got destabilizes because adsorption equilibrium alters towards the desorption process. Therefore, 25°C temperature was optimized for this adsorption experiment.

6.4 Adsorption kinetics

To explore the adsorption process a variety of kinetic models like pseudo-first-order,pseudo-second-order[20], and Elovich models were tried for fitting the kinetic records and depicted in **Figure 6.8a-c**. These kinetic parameters of these kinetic models are tabulated in **Table 6.2**. From the analysis of calculated values, the pseudo-second-order model was found to be the finest model amidst other kinetic models assuring that chemisorption is more favored in this adsorption.[21]

6.5 Adsorption isotherms

Adsorption isotherms reveal the efficacy of the Ce-BETA and their binding efficiency towards FIP molecules which is a significant factor for the adsorption procedure to occur. The binding affinity in the form of adsorption capacity is obtained by fitting the data in various isotherms like Langmuir,[22] Freundlich, Temkin, Harkins-Jura, Halsey, and Dubbin-Radushkevich.[20,21,23]

Table 6.2: Values of kinetic models and adsorption isotherms for fipronil adsorption on Ce-BETA zeolite.

Types	Model name	Parameters	Values
Kinetic models	pseudo-first-order	k_1 (1/min)	0.0168
		q_e ($mg.g^{-1}$)	476.705
	pseudo-second-order	k_2 ($g.mg^{-1}.min^{-1}$)	2.055×10^{-6}
		q_e ($mg.g^{-1}$)	1374
	Elovich model	a ($mg.g^{-1}.min^{-1}$)	10.583
		b ($g.mg^{-1}$)	0.006307
Equilibrium Isotherms	Langmuir	Q_m ($mg.g^{-1}$)	714.286
		K_L ($L.mg^{-1}$)	0.0173
	Freundlich	K_F $[(mg/g.(L/mg)]^{1/n}$	34.198
		1/n	0.5
	Temkin	B_T	0.0033
		K_T ($L.mg^{-1}$)	4.347
		β ($J.mol^{-1}$)	7.51×10^{5}
	Harkins-Jura	A	9.74×10^{4}
		B	2.52048
	Halsey isotherm	1/n	-0.44671
		K ($mg.L^{-1}$)	0.4052
	D-R model	Q_S ($mg.g^{-1}$)	558.112
		B $[(mol/J)^2]$	2.11×10^{-5}

The accurateness of these adsorption isotherms was being determined through R^2 values (Pearson correlation coefficient). With an enhancement in the initial pollutant concentration C_0, the R_L value decreases ($0<R_L<1$) which corresponds to favorable adsorption over Ce-zeolites. The isotherm fitting follows the order: Langmuir > D-R model > Temkin > Halsey > Freundlich > Harkins-Jura. The values of the adsorption isotherms are tabulated in **Table 6.2**.

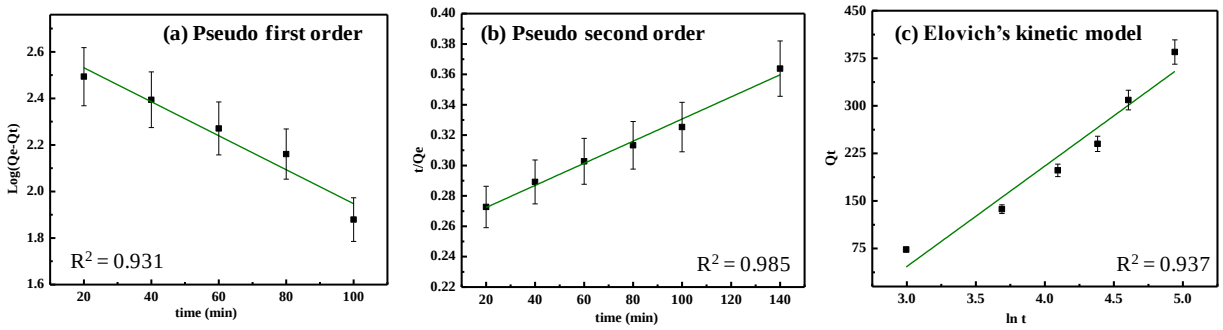

Figure 6.8: Linear fitted plots of kinetic models; (a) pseudo-first-order, (b) pseudo-second-order, and (c) Elovich's model.

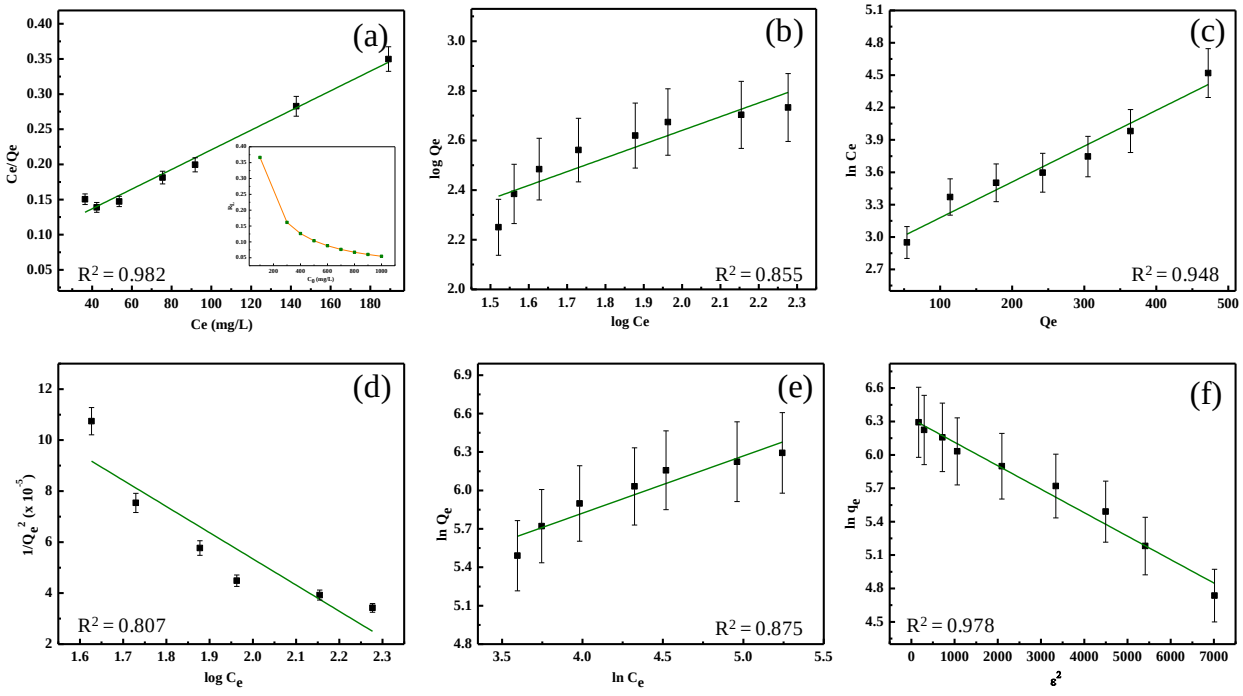

Figure 6.9: Linearly fitted adsorption isotherm plots for (a) Langmuir (inset R_L plot), (b) Freundlich, (c) Temkin, (d) Harkins-Jura, (e) Halsey, and (f) D-R model.

Temkin isotherm elaborates B_T as the heat of adsorption and expressed by formula $B_T = RT/\beta$; where 'β' denotes the maximum bond energy whose value was found to be very high i.e. 751 kJ/mol (from **Table 6.2**), higher than 40 kJ/mol which suggests chemical adsorption.[24] The Dubinin–Radushkevich (D-R) model implies a hypothesis; no uniform surface is available for stable adsorption in conformity with Polanyi's potential theory.[13] The mean adsorption energy 'E' was found to be 24.33kJ/mol which indicates chemisorptions.[18,25] The Langmuir isotherm fitted best with a higher R^2 value, suggests that there is a monolayer formation of adsorbate over the Ce-BETA adsorbent. However, D-R isotherm also fitted, indicating that the adsorbent surface is not completely uniform, which supports that the zeolite surface is rough and nonuniform.

6.6 Thermodynamic study

Thermodynamic parameters, $\Delta G°$, $\Delta S°$, and $\Delta H°$ were determined to know the adsorption process in removing FIP by Ce-zeolite.[23] The data of $\Delta H°$ and $\Delta S°$ were determined from the plot of $\ln(q_e/C_e)$ versus 1/T (**Figure 6.10**).[26] The $\Delta G°$ values of FIP adsorption on Ce-BETA were estimated for temperatures: 298K, 303K, 308K, 313K, and 318K and found to be negative (**Table 6.3**) which signifies that the process was spontaneous and thermodynamically stable.[27] The negative values of $\Delta S°$ suggest that the FIP molecules are less randomly oriented at the solid-solute interface in the adsorbed state with a reduced degree of freedom as expected.[28] And the negative value of $\Delta H°$ reveals that the adsorption method is exothermic and more favorable.[13]

Table 6.3: Values of thermodynamic parameters.

Temperature (K)	$\Delta G°$ (kJ/mol)	$\Delta H°$ (kJ/mol)	$\Delta S°$ (kJ/mol K)	R^2
298	-22.51			
303	-21.75	-67.41	-0.151	0.98
308	-20.99			
313	-20.25			
318	-19.49			

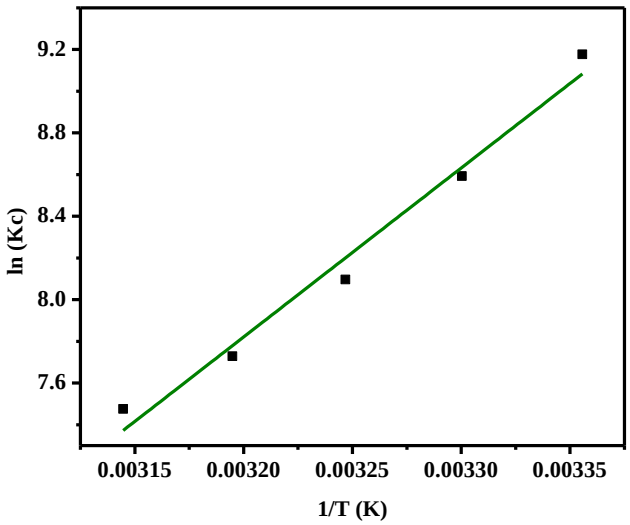

Figure 6.10: Plot of ln(K_c) versus 1/T.

6.7 Comparative studies

Zeolite 13X is a faujasite type of zeolite with a 3-dimensional structure. It is comprised of an alumino-silicate tetrahedral structure with beta-cage as a structural basic unit and adjacent to this there is a 6-angle prism connection to form a molecular sieve. The positions of SI, SI', SII, and SIII (**Figure 6.11a**) are available in 13X zeolite.[29] Whereas, Mordenite zeolite (**Figure 6.11b**) comprised of 3 different cavities, 12-membered ringed structure, oval shape 8-membered side ring channels, and link cavity channels. Probable positions of cations over the zeolite framework were categorized and suggested that the cation occupies primarily Mortier positions i.e. β-sites and α-sites.[30] However, the β-zeolite (**Figure 6.11c**) is a large pore-sized zeolite with a 3-D complex framework structure. Its complex porous network has interconnected channels of 12-membered ring cavities that form large openings for many applications.[31] It is composed of 3 polymorphic structural forms (A, B, C).

The positions of Al/Si substitutions in the zeolite structure are significant for the stability of the cation (metal) position in exchanged frameworks.[30] The beta zeolite has a comparatively high ratio of Si/Al (~13) as compared to 13X zeolite. The faujasite type X zeolite has 1.0-1.5 (Si/Al ratio) while Mordenite also having a relatively higher Si/Al ratio. With this low value of Si/Al ratio, the 13X zeolite leads to deactivation in the company of the water

medium.[32] This ratio increases the stability of the zeolite in the acidic stream and also promotes higher metal loadings.[33] From this, it can be concluded that 13X zeolite has uniform micropores with unique super-cage type structures in its framework[34] with less stability in acidic medium whereas mordenite and beta zeolite have large pore structures with higher adsorption application in the water medium. Therefore, Ce-BETA and Ce-MOR gave more than 90% removal, whereas Ce-13X gave somehow less removal than these zeolites.

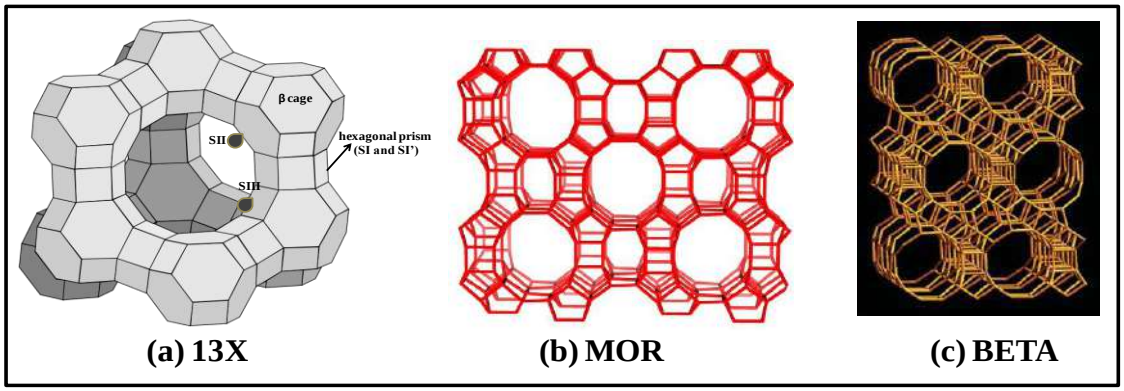

Figure 6.11: Zeolitic framework structures of (a) 13X, (b) MOR[35], and (c) BETA zeolite.[31]

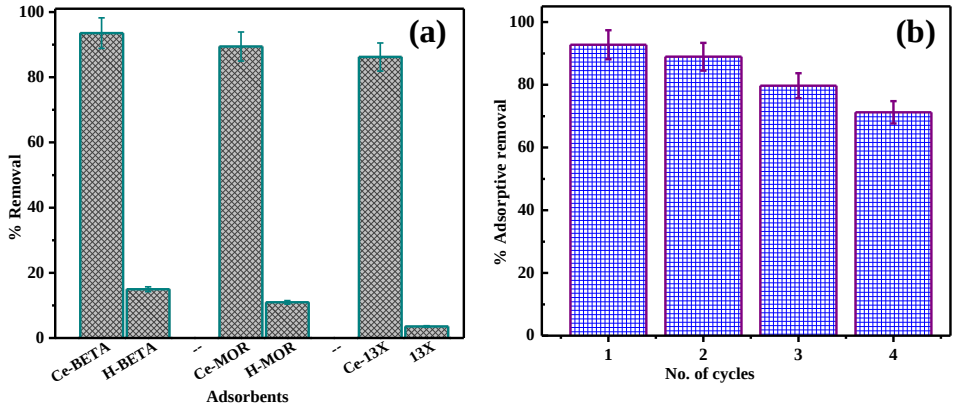

Figure 6.12: (a) Comparative study of modified as well as unmodified zeolites, and (b) reusability studies of Ce-BETA zeolite.

The comparison was conducted with modified (Ce-zeolites) and unmodified zeolite (H-MOR, H-BETA, H-13X) adsorbents. Ce-BETA, Ce-MOR, Ce-13X zeolites gave 94%, 90%, 86% whereas H-BETA, H-MOR, 13X only 13.8%, 10%, 3.2% of FIP removal (**Figure 6.12a**) respectively. The exchange of H^+ by Ce^{3+} (metal ions) brings strong interactions between the

adsorbent surface and organophosphate pollutant (FIP).[36,37] This leads to the conclusion that there was a crucial need to modify zeolites with cerium to enhance their adsorption efficiency for better FIP removal.

6.8 Regeneration and reusability of cerium modified zeolites

The washing method was adopted for the regeneration of exhausted adsorbents to reuse them after one cycle. The exhausted adsorbents were thoroughly washed with the different eluents (80-100% ethanol and 0.1-1.0 M NaCl solutions) for reusability[38] and centrifuged for 40 minutes at 6000 rpm (298 K) followed by drying in an oven for 12h at temperature 353 K. Best solvent (95% ethanol) was considered for further washings to give maximum %removal (~71%) of FIP pollutant. Before reuse (Ce-13X, Ce-BETA, and Ce-MOR), the regenerated adsorbent was ultrasonicated for 5-10 min for better efficiency. Reusability studies were performed up to 4 cycles and it was observed that the %removal of FIP decreased to 86% compared with the first cycle (reusability bar graph is shown in **Figure 6.12b**).

6.9 TOC analysis

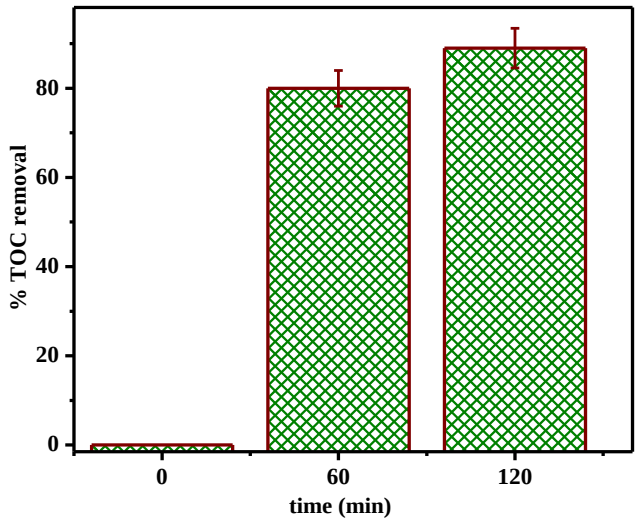

Figure 6.13: TOC analysis of synthetic wastewater at a different time interval.

The %TOC removal of synthetic wastewater was also determined at different time interval (**Figure 6.13**) and ~88% removal was observed after the treatment of 2h. The initial

concentration of FIP pollutants was taken as reported in literature[39] for TOC analysis. And TOC analysis was taken at 0 min, 60 min, and 120 min time intervals.

6.10 Conclusion

Ammonium forms of zeolites (H-BETA, H-MOR, H-13X) were modified with cerium by ion-exchange method to adsorb fipronil. The Ce-zeolites were proved to have much higher adsorption capacities than their H-form zeolites. The comparative studies of adsorption parameters were carried out and Ce-BETA zeolite was observed to be the best (94% removal) one because of its higher surface area, rough morphology and high Si/Al ratio lead to higher zeolite stability. Ce-MOR also has ~90% removal due to its high Si/Al ratio that promotes more metal loading which finally helps in the adsorption process. Langmuir isotherm and pseudo-second-order model signifying monolayer adsorption with a faster adsorption rate. The negative $\Delta G°$ value confirms that the FIP adsorption was spontaneous and exothermic. The high adsorption that occurred may be due to electrostatic or chemical interaction. Moreover, the comparison studies of modified and unmodified zeolites were done which proves the need for modification of adsorbents for better FIP removal.

References

(1) Thakur, R.; Barman, S. A Comparative Study on Catalytic Performance of Modified Nanocrystalline and Microcrystalline Zeolite X for Synthesis of Cumene by Transalkylation of 1,4-Diisopropylbenzene with Benzene. *Kinet. Catal.* **2016**, *57* (5), 592–601. https://doi.org/10.1134/S0023158416050189.

(2) Rathi, A.; Basu, S.; Barman, S. Adsorptive Removal of Fipronil from Its Aqueous Solution by Modified Zeolite HZSM-5: Equilibrium, Kinetic and Thermodynamic Study. *J. Mol. Liq.* **2019**, *283*, 867–878. https://doi.org/10.1016/j.molliq.2019.02.140.

(3) Thakur, R.; Barman, S.; Kumar Gupta, R. Synthesis of Cumene by Transalkylation over Modified Beta Zeolite: A Kinetic Study. *Brazilian J. Chem. Eng.* **2016**, *33* (4), 957–967. https://doi.org/10.1590/0104-6632.20160334s20150333.

(4) Ma, R.; Jahurul Islam, M.; Amaranatha Reddy, D.; Kim, T. K. Transformation of CeO2 into a Mixed Phase CeO_2/Ce_2O_3 Nanohybrid by Liquid Phase Pulsed Laser Ablation for

Enhanced Photocatalytic Activity through Z-Scheme Pattern. *Ceram. Int.* **2016**, *42* (16), 18495–18502. https://doi.org/10.1016/j.ceramint.2016.08.186.

(5) Deng, C.; Zhang, J.; Dong, L.; Huang, M.; Li, B.; Jin, G.; Gao, J.; Zhang, F.; Fan, M.; Zhang, L.; Gong, Y. The Effect of Positioning Cations on Acidity and Stability of the Framework Structure of y Zeolite. *Sci. Rep.* **2016**, *6* (November 2015), 1–13. https://doi.org/10.1038/srep23382.

(6) Chandra Shekara, B. M.; Jai Prakash, B. S.; Bhat, Y. S. Dealumination of Zeolite BEA under Microwave Irradiation. *ACS Catal.* **2011**, *1* (3), 193–199. https://doi.org/10.1021/cs1000448.

(7) Ramasamy, V.; Mohana, V.; Rajendran, V. Characterization of Ca Doped CeO_2 Quantum Dots and Their Applications in Photocatalytic Degradation. *OpenNano* **2018**, *3*, 38–47. https://doi.org/10.1016/j.onano.2018.04.002.

(8) Wang, M.; Shen, M.; Jin, X.; Tian, J.; Li, M.; Zhou, Y.; Zhang, L.; Li, Y.; Shi, J. Oxygen Vacancy Generation and Stabilization in CeO_{2-x} by Cu Introduction with Improved CO_2 Photocatalytic Reduction Activity. *ACS Catal.* **2019**, *9* (5), 4573–4581. https://doi.org/10.1021/acscatal.8b03975.

(9) Huang, Z.; Zhang, J.; Li, P.; Xu, L.; Zhang, X.; Yuan, Y.; Xu, L. Tert -Butylation of Naphthalene by Tertiary Butanol over HY Zeolite and Cerium-Modified HY Catalysts. *Catal. Sci. Technol.* **2017**, *7* (20), 4700–4709. https://doi.org/10.1039/c7cy01227f.

(10) Zhang, G.; Wu, L.; Tang, A.; Ma, Y.; Song, G. L.; Zheng, D.; Jiang, B.; Atrens, A.; Pan, F. Active Corrosion Protection by a Smart Coating Based on a MgAl-Layered Double Hydroxide on a Cerium-Modified Plasma Electrolytic Oxidation Coating on Mg Alloy AZ31. *Corros. Sci.* **2018**, *139* (May), 370–382. https://doi.org/10.1016/j.corsci.2018.05.010.

(11) Shan, W.; Liu, F.; He, H.; Shi, X.; Zhang, C. A Superior Ce-W-Ti Mixed Oxide Catalyst for the Selective Catalytic Reduction of NO_x with NH_3. *Appl. Catal. B Environ.* **2012**, *115–116* (1), 100–106. https://doi.org/10.1016/j.apcatb.2011.12.019.

(12) Boningari, T.; Ettireddy, P. R.; Somogyvari, A.; Liu, Y.; Vorontsov, A.; McDonald, C. A.; Smirniotis, P. G. Influence of Elevated Surface Texture Hydrated Titania on Ce-Doped Mn/TiO2 Catalysts for the Low-Temperature SCR of NO_x under Oxygen-Rich Conditions. *J. Catal.* **2015**, *325*, 145–155. https://doi.org/10.1016/j.jcat.2015.03.002.

(13) Goyal, N.; Bulasara, V. K.; Barman, S. Removal of Emerging Contaminants Daidzein and Coumestrol from Water by Nanozeolite Beta Modified with Tetrasubstituted Ammonium Cation. *J. Hazard. Mater.* **2018**, *344* (February), 417–430. https://doi.org/10.1016/j.jhazmat.2017.10.051.

(14) Panagiotopoulou, C.; Kontori, E.; Perraki, T.; Kakali, G. Dissolution of Aluminosilicate Minerals and By-Products in Alkaline Media. *J. Mater. Sci.* **2007**, *42* (9), 2967–2973. https://doi.org/10.1007/s10853-006-0531-8.

(15) Gorrepati, E. A.; Wongthahan, P.; Raha, S.; Fogler, H. S. Silica Precipitation in Acidic Solutions: Mechanism, PH Effect, and Salt Effect. *Langmuir* **2010**, *26* (13), 10467–10474. https://doi.org/10.1021/la904685x.

(16) Li, T.; Lu, M.; Gao, Y.; Huang, X.; Liu, G.; Xu, D. Double Layer MOFs M-ZIF-8@ZIF-67: The Adsorption Capacity and Removal Mechanism of Fipronil and Its Metabolites from Environmental Water and Cucumber Samples. *J. Adv. Res.* **2020**, *24*, 159–166. https://doi.org/10.1016/j.jare.2020.03.013.

(17) Parthasarathy, P.; Narayanan, S. K. Effect of Hydrothermal Carbonization Reaction Parameters On. *Environ. Prog. Sustain. Energy* **2014**, *33* (3), 676–680. https://doi.org/10.1002/ep.

(18) Khadir, A.; Negarestani, M.; Ghiasinejad, H. Low-Cost Sisal Fibers/Polypyrrole/Polyaniline Biosorbent for Sequestration of Reactive Orange 5 from Aqueous Solutions. *J. Environ. Chem. Eng.* **2020**, *8* (4), 103956. https://doi.org/10.1016/j.jece.2020.103956.

(19) Singh, J.; Sharma, S.; Aanchal; Basu, S. Synthesis of Fe_2O_3/TiO_2 Monoliths for the Enhanced Degradation of Industrial Dye and Pesticide via Photo-Fenton Catalysis. *J. Photochem. Photobiol. A Chem.* **2019**, *376*, 32–42. https://doi.org/10.1016/j.jphotochem.2019.03.004.

(20) Sharma, M.; Singh, J.; Hazra, S.; Basu, S. Remediation of Heavy Metal Ions Using Hierarchically Porous Carbon Monolith Synthesized via Nanocasting Method. *J. Environ. Chem. Eng.* **2018**, *6* (2), 2829–2836. https://doi.org/10.1016/j.jece.2018.04.042.

(21) Sharma, M.; Hazra, S.; Basu, S. Kinetic and Isotherm Studies on Adsorption of Toxic Pollutants Using Porous $ZnO@SiO_2$ Monolith. *J. Colloid Interface Sci.* **2017**, *504*, 669–679. https://doi.org/10.1016/j.jcis.2017.06.020.

(22) Langmuir, I. The Adsorption of Gases on Plane Surfaces of Glass, Mica and Platinum. *J. Am. Chem. Soc.* **1918**, *40* (9), 1361–1403. https://doi.org/10.1021/ja02242a004.

(23) Sharma, J.; Sharma, M.; Basu, S. Synthesis of Mesoporous MgO Nanostructures Using Mixed Surfactants Template for Enhanced Adsorption and Antimicrobial Activity. *J. Environ. Chem. Eng.* **2017**, *5* (4), 3429–3438. https://doi.org/10.1016/j.jece.2017.07.015.

(24) Wang, N.; Chen, J.; Wang, J.; Feng, J.; Yan, W. Removal of Methylene Blue by Polyaniline/TiO_2 Hydrate: Adsorption Kinetic, Isotherm and Mechanism Studies. *Powder Technol.* **2019**, *347*, 93–102. https://doi.org/10.1016/j.powtec.2019.02.049.

(25) Inyinbor, A. A.; Adekola, F. A.; Olatunji, G. A. Kinetics, Isotherms and Thermodynamic Modeling of Liquid Phase Adsorption of Rhodamine B Dye onto Raphia Hookerie Fruit Epicarp. *Water Resour. Ind.* **2016**, *15*, 14–27. https://doi.org/10.1016/j.wri.2016.06.001.

(26) Sharma, M.; Choudhury, D.; Hazra, S.; Basu, S. Effective Removal of Metal Ions from Aqueous Solution by Mesoporous MnO_2 and TiO_2 Monoliths: Kinetic and Equilibrium Modelling. *J. Alloys Compd.* **2017**, *720*, 221–229.

https://doi.org/10.1016/j.jallcom.2017.05.260.

(27) Goyal, N.; Barman, S.; Bulasara, V. K. Efficient Removal of Bisphenol S from Aqueous Solution by Synthesized Nano-Zeolite Secony Mobil-5. *Microporous Mesoporous Mater.* **2018**, *259*, 184–194. https://doi.org/10.1016/j.micromeso.2017.10.015.

(28) Lu, X.; Deng, S.; Wang, B.; Huang, J.; Wang, Y.; Yu, G. Adsorption Behavior and Mechanism of Perfluorooctane Sulfonate on Nanosized Inorganic Oxides. *J. Colloid Interface Sci.* **2016**, *474*, 199–205. https://doi.org/10.1016/j.jcis.2016.04.032.

(29) Guo, Y.; Zhang, H.; Liu, Y. Desorption Characteristics and Kinetic Parameters Determination of Molecular Sieve by Thermogravimetric Analysis/Differential Thermogravimetric Analysis Technique. *Adsorpt. Sci. Technol.* **2018**, *36* (7–8), 1389–1404. https://doi.org/10.1177/0263617418772665.

(30) Mohammadzadeh Kakhki, R.; Karimian, A.; Hasan-nejad, H.; Ahsani, F. Zinc Oxide–Nanoclinoptilolite as a Superior Catalyst for Visible Photo-Oxidation of Dyes and Green Synthesis of Pyrazole Derivatives. *J. Inorg. Organomet. Polym. Mater.* **2019**, *29* (4), 1358–1367. https://doi.org/10.1007/s10904-019-01100-8.

(31) Smith, K.; El-Hiti, G. A. Use of Zeolites for Greener and More Para-Selective Electrophilic Aromatic Substitution Reactions. *Green Chem.* **2011**, *13* (7), 1579. https://doi.org/10.1039/c0gc00689k.

(32) Chibani, S.; Chebbi, M.; Lebègue, S.; Bučko, T.; Badawi, M. A DFT Investigation of the Adsorption of Iodine Compounds and Water in H-, Na-, Ag-, and Cu- Mordenite. *J. Chem. Phys.* **2016**, *144* (24), 244705. https://doi.org/10.1063/1.4954659.

(33) Nenoff, T. M.; Rodriguez, M. A.; Soelberg, N. R.; Chapman, K. W. Silver-Mordenite for Radiologic Gas Capture from Complex Streams: Dual Catalytic CH_3I Decomposition and I Confinement. *Microporous Mesoporous Mater.* **2014**, *200*, 297–303. https://doi.org/10.1016/j.micromeso.2014.04.041.

(34) Song, Z.; Liu, G.; He, D.; Pang, X.; Tong, Y.; Wu, Y.; Yuan, D.; Liu, Z.; Xu, Y. Acetylene Hydrochlorination over 13X Zeolite Catalysts at High Temperature. *Green Chem.* **2016**, *18* (22), 5994–5998. https://doi.org/10.1039/c6gc02291j.

(35) Mafra, L.; Vidal-Moya, J. A.; Blasco, T. Structural Characterization of Zeolites by Advanced Solid State NMR Spectroscopic Methods. In *Annual Reports on NMR Spectroscopy*; 2012; Vol. 77, pp 259–351. https://doi.org/10.1016/B978-0-12-397020-6.00004-0.

(36) Dehghani, M. H.; Niasar, Z. S.; Mehrnia, M. R.; Shayeghi, M.; Al-Ghouti, M. A.; Heibati, B.; McKay, G.; Yetilmezsoy, K. Optimizing the Removal of Organophosphorus Pesticide Malathion from Water Using Multi-Walled Carbon Nanotubes. *Chem. Eng. J.* **2017**, *310*, 22–32. https://doi.org/10.1016/j.cej.2016.10.057.

(37) Yaseen, M.; Ehsan, N.; Qamar, S. U. R.; Ali, A.; Khan, W. A.; Khan, A. Effect of Organophosphate Pesticide (Chlorpyrifos, Fipronil, and Malathion) on Certain Organs of

Rattus Rattus. *GSC Biol. Pharm. Sci.* **2019**, *6* (3), 011–015. https://doi.org/10.30574/gscbps.2019.6.3.0016.

(38) Zolfaghari, M.; Magdouli, S.; Tanabene, R.; Komtchou, S. P.; Martial, R.; Saffar, T. Pragmatic Strategy for the Removal of Ammonia from Gold Mine Effluents Using a Combination of Electro-Coagulation and Zeolite Cation Exchange Processes: A Staged Approach. *J. Water Process Eng.* **2020**, *37* (June), 101512. https://doi.org/10.1016/j.jwpe.2020.101512.

(39) Nthumbi, R. M.; Ngila, J. C. Electrospun and Functionalized PVDF/PAN Nanocatalyst-Loaded Composite for Dechlorination and Photodegradation of Pesticides in Contaminated Water. *Environ. Sci. Pollut. Res.* **2016**, *23* (20), 20214–20231. https://doi.org/10.1007/s11356-016-7136-9.

Chapter 7: C-dots@zeolite composite for antibiotic degradation and degraded products analysis

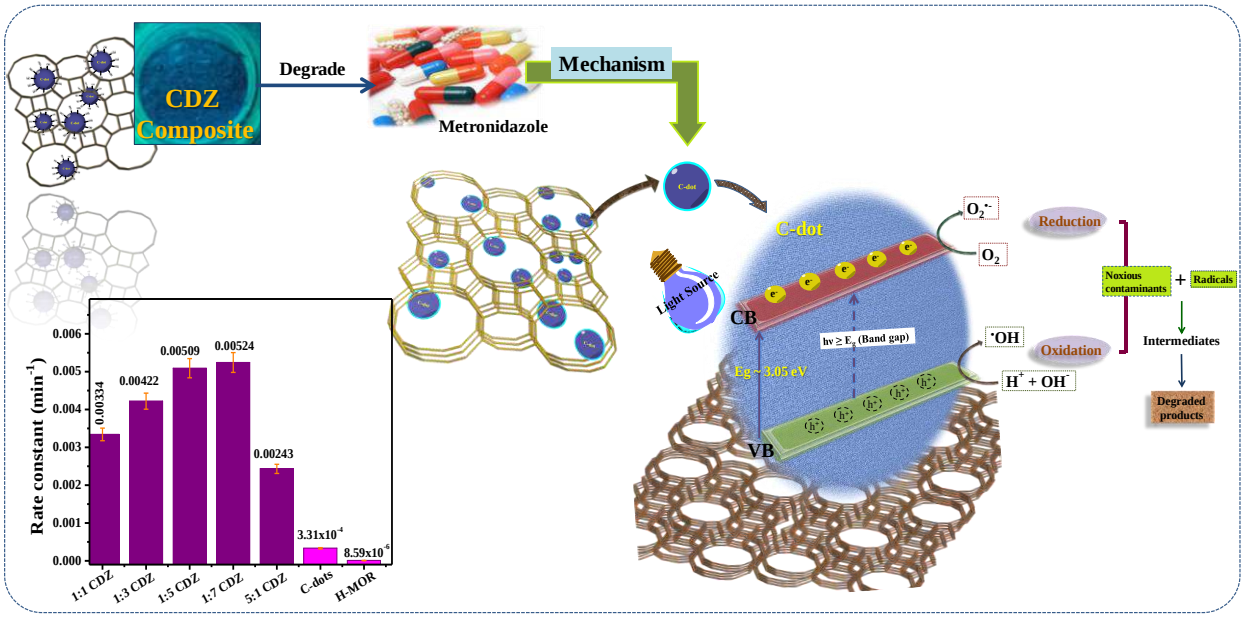

Highlights

- Extensively used antibiotics, industrial dye, and raw wastewater were degraded.
- Hydrothermal preparation of C-dots@zeolite (CDZ) (1:1, 1:3, 1:5, 5:1, 1:7) ratios.
- Photodegradation was compared under sunlight/UV/Visible lights.
- 1:5 CDZ efficiently degrade recalcitrant metronidazole (~79%) and RhB dye (~90%).
- Intermediate products were analyzed by GC-MS analysis.

7.1 Synthesis of photocatalyst

7.1.1 Synthesis of C-dots

The precursor catechol was dissolved in a specific amount of methanol (MeOH) and after complete dissolution, the transparent solution appeared. Now, shift that transparent solution to the Teflon-lined vessel of appropriate volume to get treated hydrothermally and tightened in the stainless steel container. Now, this hydrothermal container was kept at 180 °C temperature for 12 hours. The reaction was cooled at room temp, washed with PET ether, centrifuged, and dried to obtain C-dots powder.[1]

7.1.2 Synthesis of C-dots@zeolite composites

The series of five different CDZ composites were prepared by varying the weight ratios of C-dots: zeolite (1:1, 1:3, 1:5, 5:1, 1:7). The specific amount of precursor catechol and 200 mg of the zeolite were mixed in solvent and stirred for 6-7 h for homogenous distribution. Then the reaction mixture was kept in stainless steel hydrothermal at 180 °C temperature for 12 h. Then it was cooled to room temp, washed with PET ether, centrifuged, and dried to obtain powdered CDZ composite.[1] The general synthesis scheme for the CDZ composite was shown in **Scheme 7.1**.

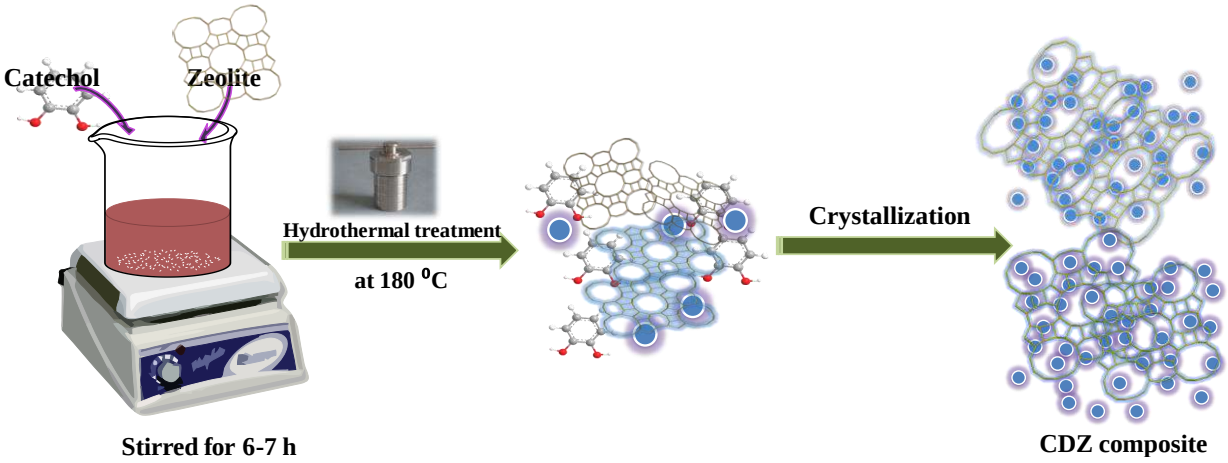

Scheme 7.1: Synthesis scheme for CDZ composite.

7.2 Characterization of photocatalyst

7.2.1 XRD analysis

The XRD pattern of C-dots, MOR zeolite, and CDZ are depicted in **Figure 7.1a**. The characteristic peaks were shown at 2Θ value of 6.55°, 8.70°, 9.76°, 13.51°, 15.29°, 19.67°, 22.42°, 25.75°, 26.42°, 27.68°, 31.00° for MOR which corresponded to (110), (020), (200), (111), (310), (330), (150), (202), (350), (132), (402) lattice planes of zeolite (JCPDS no. 430171), respectively. These spectra of composites revealed that they retained the zeolite framework structures even after the incorporation of C-dots. The XRD spectrum of C-dot (**inset of Figure 7.1a**) has a broad peak at 24.04° which corresponds to the (002) plane. The XRD peak of C-dot was merged with the peaks of zeolite in the case of CDZ nanocomposites. The broadness in the XRD spectrum confirmed the small size of the C-dots while sharp peaks indicated that the crystallinity of the zeolite was not disturbed.

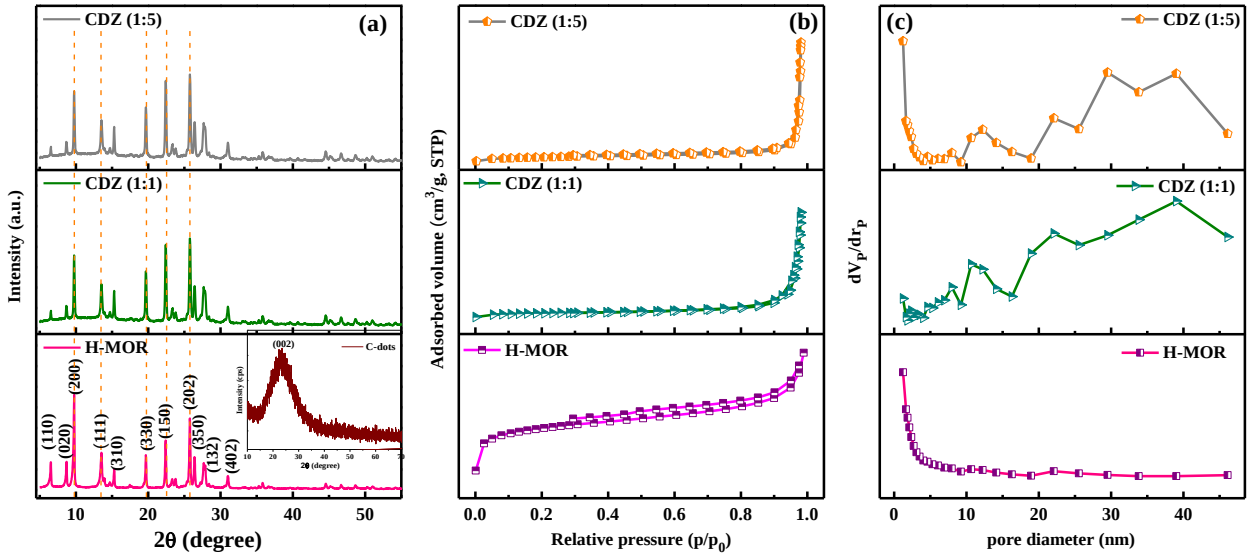

Figure 7.1: (a) XRD analysis (C-dots in inset), (b) BET analysis, and (c) BJH analysis of H-MOR, 1:1 CDZ, and 1:5 CDZ composites.

7.2.2 N_2 adsorption-desorption isotherms

The surface area analysis of as-prepared catalysts was done by N_2 adsorption-desorption isotherm. The specific surface area of 1:5 CDZ is 187 m^2/g, H-MOR (500 m^2/g), and other composites are tabulated in **Table 7.1**. The CDZ composites and H-MOR zeolite possess type-IV

isotherm (**Figure 7.1b**). The surface area was decreased due to the incorporation of non-porous C-dots into the porous zeolite framework. From the BJH plots (**Figure 7.1c**), it has been seen that after fabrication with C-dots the intensity of macro-pores increased in the ratio of 1:5 CDZ composites while in the case of H-MOR the macro-pores were comparatively less. The micro-pores are also available in the zeolite and prepared CDZ composites.[2]

Table 7.1: Surface properties of the prepared composites and zeolite material.

Catalyst	Surface area (m^2/g)	Total pore volume (cm^3/g)	Mean pore diameter (nm)
H-MOR	500	0.172	2.6
1:1 CDZ	78	0.156	24.8
1:3 CDZ	139	0.173	27.7
1:5 CDZ	187	0.244	33.4
5:1 CDZ	51	0.082	44.7
1:7 CDZ	189	0.198	35.6

7.2.3 XPS analysis

The XPS characterization technique revealed the chemical states of the present elements and their availability (oxygen, carbon, silicon, aluminum elements) in the as-prepared photocatalyst. The survey spectrum of the 1:5 CDZ composite possesses peaks of all the mentioned elements (O, C, Si, and Al) as shown in **Figure 7.2a**. The structural properties (bonds b/w the elements) of the CDZ composite were also predicted by XPS analysis, the peak of carbon was deconvoluted into 2 major peaks i.e., 284.63 eV and 286.05 eV which correspond to C-C/C=C and C-O (**Figure 7.2b**), respectively,[3,4] while the O 1s spectrum (**Figure 7.2c**) has the deconvoluted peaks at 530.8 eV and 532.68 eV confirming the presence of C=O/O-Al and Si-O/C-O-C in CDZ nanocomposite.[3,5,6]

7.2.4 SEM-EDS analysis

The morphological analysis was carried out with SEM characterizations. Based on the SEM-EDS data, it can be seen that the C-dots have been successfully fabricated into the zeolite framework. **Figure 7.2d** depicted the SEM image of 1:5 CDZ composite having aggregation of small particles with a rough surface. **Figure 7.2e** shows the elemental composition of the 1:5 CDZ composite, and the availability of carbon elements indicates the presence of C-dots in the

zeolite framework and distribution of C-dots over the zeolite. The % elemental composition from EDS analysis also gave an idea about the elements like carbon from the C-dots and total oxygen from the hydroxyl group of C-dots along with alumino-silicates of zeolite frameworks.

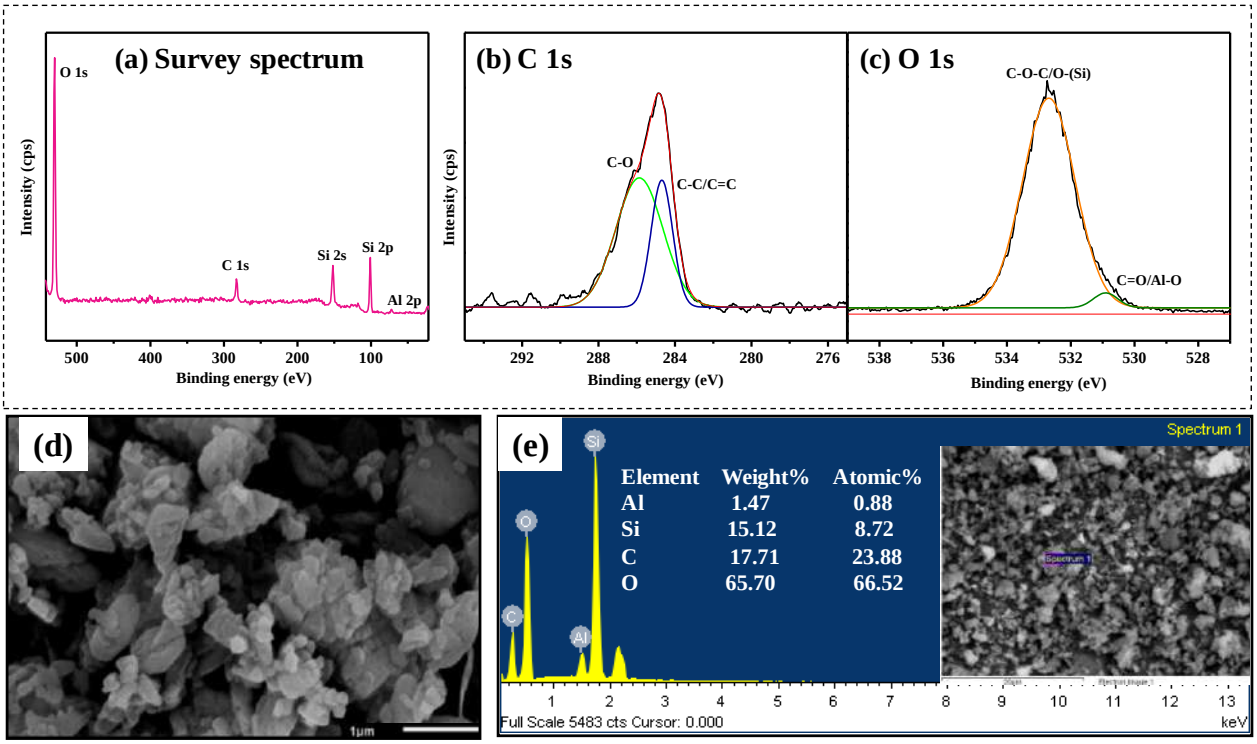

Figure 7.2: XPS analysis: (a) survey spectrum, (b) C 1s, (c) O 1s, (d) SEM analysis, (e) EDS spectrum with the elemental composition of Al, Si, C, and O of 1:5 CDZ composite.

7.2.5 HRTEM analysis

From HRTEM images, d-spacing values of C-dots, MOR zeolite, and 1:5 CDZ composite have been calculated using ImageJ software (**Figure 7.3**). **Figure 7.3a** indicated that the incorporation of C-dots has been successfully taken place inside the zeolite channels. The d-spacing value of C-dots was found to be 0.24 nm indicating the (224) plane as shown in **Figure 7.3a-b**. The CDZ composites have planes of both C-dots and MOR zeolite as shown in **Figure 7.3**. For MOR zeolite, 1.35, 1.02, 0.90, 0.65 nm d-spacing value with (110), (200), (310) and (330) planes were depicted in **Figure 7.3c-e**.[2]

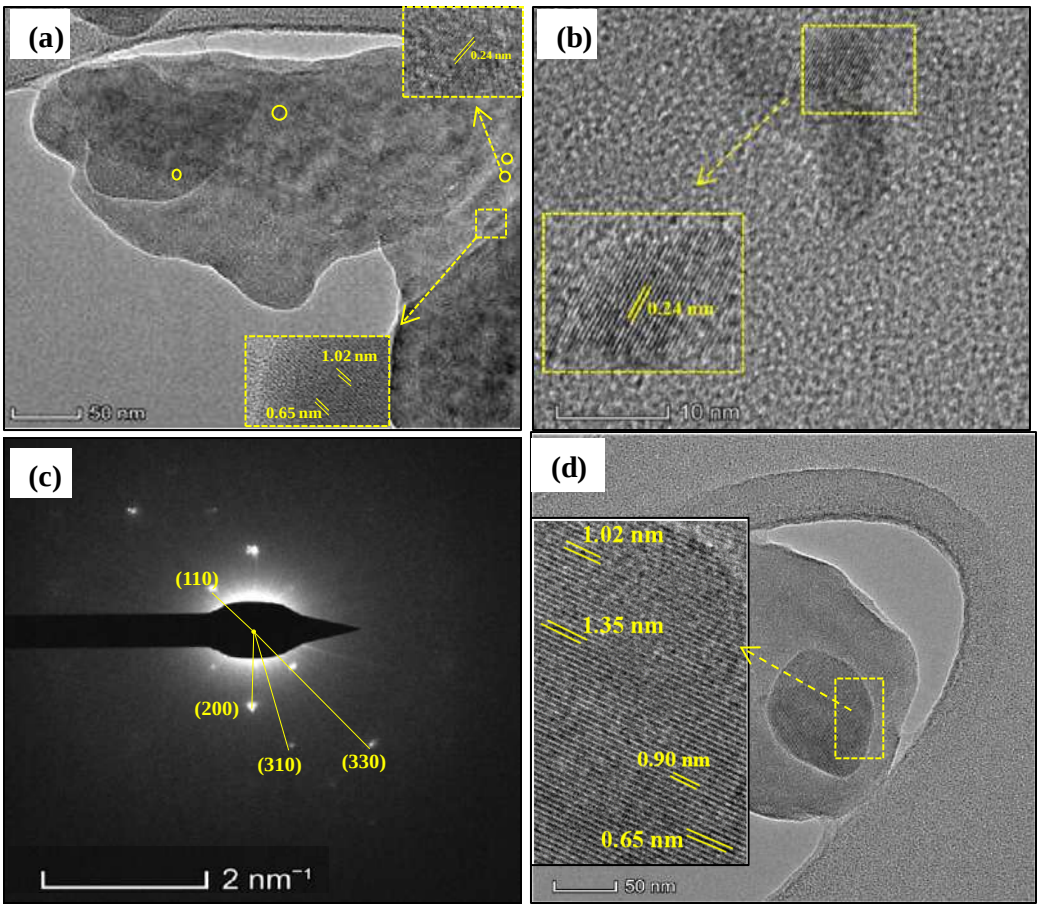

Figure 7.3: HRTEM image of (a) 1:5 CDZ composite, (b) C-dots with d-spacing values, (c) SAED analysis of 1:5 CDZ composite with corresponding planes, and (d) HRTEM analysis of zeolite (insets d-spacing).

7.2.6 Optical properties

For a composite to be an efficient photocatalyst, it must possess greater light-absorbing properties with a narrow bandgap, which results in decreased recombination of photoinduced e^- /h^+ pairs. The UV-DRS method was used to identify the absorption wavelength range of the 1:5 CDZ composite and C-dots. The highly intense absorbance bands of C-dots and CDZ composites (1:1, 1:3, 1:5, 5:1, 1:7) were lied in the 240-350 nm range, indicating them as a UV-active material (**Figure 7.4a**). In addition, Tauc's equation (**Equation 7.1**) was applied to calculate the bandgap energy of the synthesized materials.[7–9]

$$(\alpha h\nu)^{1/2} = h\nu - E_g \qquad (7.1)$$

The absorption coefficient, Plank constant, light frequency, and bandgap energy were designed by α, h, ν, and E_g, respectively. The bandgap energy of C-dots, 1:1, 1:3, 1:5, 5:1, 1:7 CDZ composites were found to be 3.78 eV, 3.30 eV, 3.22 eV, 3.05 eV, 3.43 eV, 3.19 eV, respectively as depicted in **Figure 7.4b**. The narrow bandgap of 1:5 CDZ composite implies the greater light-absorbing character due to the decline in recombination of electron/hole pairs which results in better photocatalytic efficiency than other composites.

The photoluminescence (PL) study suggested that the photocatalytic activity of the prepared composite is greatly dependent on the recombination rate of e^-/h^+ charged species. The PL data of the C-dots and CDZ (1:1, 1:3, 1:5, 5:1, 1:7) nanocomposite were recorded at the excitation wavelength of 310 nm as shown in **Figure 7.4c**. The lower intensity in the PL spectrum indicated the low recombination rate of electrons/holes which leads to better charge separation. The peak intensity of C-dots and other composites (1:1, 1:3, 5:1, 1:7) was higher as compared to 1:5 CDZ composite, indicating the lower recombination rate with better charge separation of electron/hole pairs and thereby gives better degradation efficiency than others. The reason for the better charge separation in the composite may be due to the formation of heterojunctions which lead to improved e^- transfer. At the surface of the zeolite in CDZ composite, the transfer of photo-induced electrons is improved due to the electrical conductance between the zeolite and C-dot surface. Therefore, the as-prepared 1:5 CDZ composite has suitable optical properties which made it an efficient photocatalyst that resulted in better photocatalytic activity.[7,9,10]

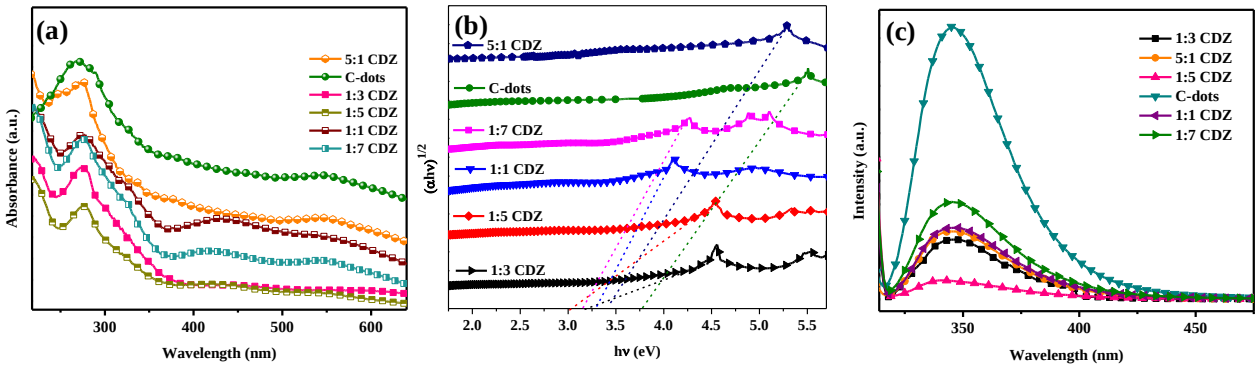

Figure 7.4: (a) UV-Visible DRS plot, (b) Tauc plot, and (c) PL-spectra of C-dots and CDZ (1:1, 1:3, 1:5, 5:1, 1:7) nanocomposite.

7.3 Photocatalytic degradation

Different ratios of CDZ (1:1, 1:3, 1:5, 5:1, 1:7) were inspected for their catalytic efficiency against the noxious contaminants (MET and RhB). The dose of CDZ photocatalyst was varied from 0.05-0.25 g/L, and poured into a specific volume of the contaminant solution of MET (10 ppm), and stirred for 40 min in dark conditions to accomplish the state of equilibrium for further degradation activity. The MET solution was supplied with various light sources (UV/sunlight/visible) and the treated solution was checked at different time intervals to know the kinetics and rate constants. To examine the catalytic activity, the post-treatment solution of MET was withdrawn, filtered and the value was checked at its λ_{max} ~320 nm.[11] The optimum experimental parameters were aimed to inspect by varying the photocatalyst dose, pH of the solution, time, light sources, and kinetics. The intensities of visible (45 W CFL lamp), UV (100 W Hg lamp), and sunlight sources were ~100 W/m^2, 46-48 W/m^2, and 600 W/m^2 respectively. To know the responsible species for pollutant degradation the scavenging experiment was also carried out. About 10^{-3} M scavenger solutions were prepared for scavenger study. The experimental studies were performed in triplicates for accuracy.

The kinetic analysis of the as-prepared ratios of CDZ composites was investigated and their rate constants were calculated. **Figure 7.5a** depicts the catalytic activities of all the composites (1:1, 1:3, 1:5, 5:1, and 1:7) along with bulk zeolite powder and C-dots for 150 min UV light irradiations. The rate constants on different catalysts were determined from the intercept of the graph, $\ln(C/C_0)$ versus time, and shown in **Figure 7.5b**. The 'k' values for zeolite, C-dots, CDZ (1:1, 1:3, 1:5, 5:1, and 1:7) are 8.5 x 10^{-6}, 3.31 x 10^{-4}, 0.0033, 0.0042, 0.0051, 0.00243 and 0.00524 min^{-1}, respectively. The 1:5 CDZ composite was found to have the maximum rate constant and % degradation (64.85%) due to its high surface area, pore-volume, low recombination rate, and suitable bandgap energy value.

7.3.1 Effect of catalyst dose

From the above data, 1:5 CDZ composite was further investigated for the effect of catalyst dose from 0.05 g/L to 0.25 g/L (**Figure 7.5c**). The increased amount of composite lead to an increase in the photocatalytic efficiency i.e. from 0.05 g/L to 0.2 g/L and then a slight

decrease was observed. This decline of degradation efficiency might be due to the saturation and opacity of the contaminant solution resulting in the blockage of active sites.[8,12]

7.3.2 Effect of pH

The optimum pH for MET degradation (**Figure 7.5d**) and point of zero charge (PZC) was also determined for the 1:5 CDZ composite. The PZC value was evaluated by the salt addition method reported by Bakatula and coworkers.[13] From the graph, ΔpH ($pH_f - pH_i$) versus pH_i, the PZC value of the optimum photocatalyst was found to be ~ pH 3.4 (**Figure 7.5e**). The effect of pH was investigated from pH 1-11 and the % degradation was found to be the best in the acidic environment i.e. nearby pH 4. This is because the catalyst's surface becomes positively charged when pH is greater than PZC and attracts the negatively charged MET contaminant.[2,14] The efficiency of catalyst decreases in the alkaline medium due to excess of OH^- species available on the catalyst surface making it negatively charged due to which deactivation of active sites occurs.[15]

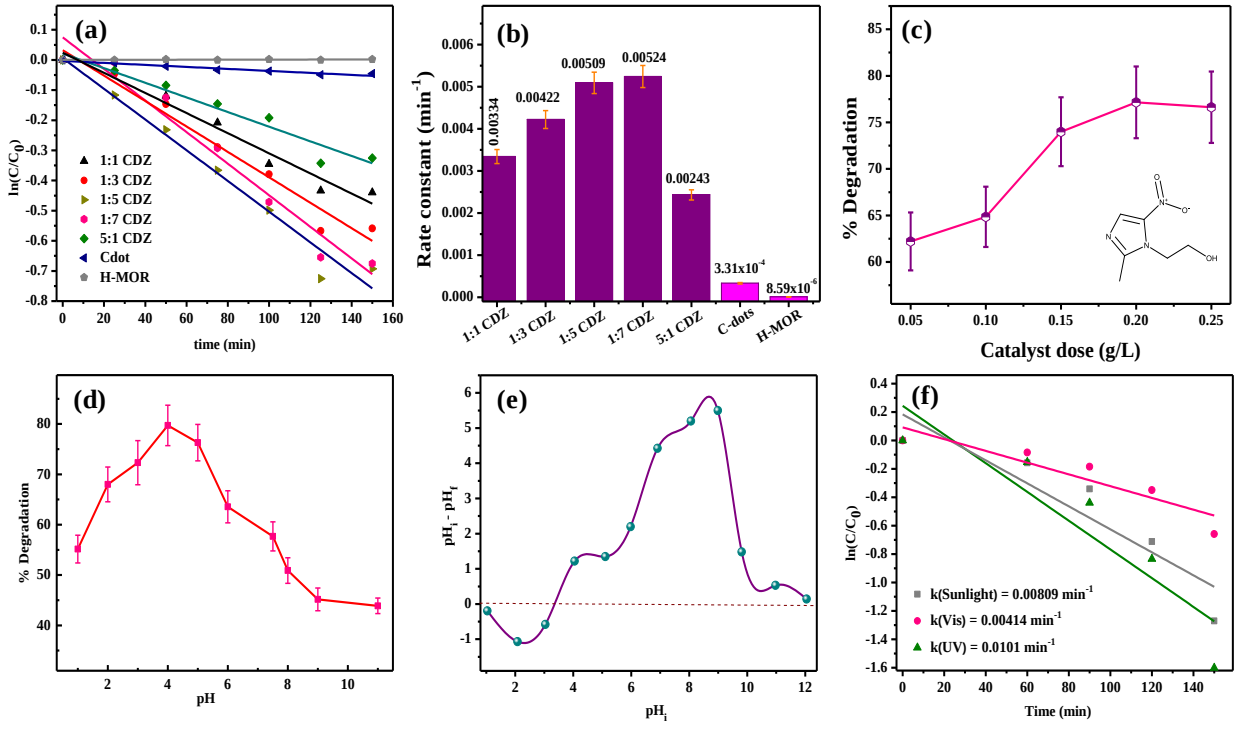

Figure 7.5: Plots of (a) time study, (b) rate constant for the photo-degradation of MET by zeolite, C-dots, CDZ (1:1, 1:3, 1:5, 5:1, and 1:7) composites; effects of (c) catalyst dose, (d) pH, (e) PZC, (f) different light sources with 1:5 CDZ composite.

7.3.3 Effect of different light sources and illuminating area

For comparison, different light sources (UV, sunlight, and visible) were used to find the degradation efficiency of the specific pollutants. **Figure 7.5f** illustrates the kinetic analysis and rate constant of MET under various light sources. The photocatalysis followed the pseudo-first-order kinetics and their 'k' values were found in the order, UV > sunlight > visible and the values are tabulated in **Table 7.2**. The significance of the illuminating area was also explored by taking equal amounts of MET pollutant in 4 containers of different diameters. The exposed surface areas of the pollutant were calculated to be 2.5, 5, 10, 15 cm^2 (constant distance was maintained for the pollutant's upper layer to the light source in each container). The % degradation was observed to increase with an increase in surface area (**Figure 7.6a**).[16]

Table 7.2: Rate constants for MET degradation under different light sources by 1:5 CDZ composite.

Light sources	Rate constants (min^{-1})
Sunlight	0.0081
Visible	0.0041
UV	0.0101

7.3.4 COD and TOC analysis

The real industrial wastewater degradation was tested with 1:5 CDZ composite for its photo-activity. The COD (Chemical Oxygen Demand) and TOC (Total Organic Carbon) analyses were done to quantify the organic pollutants of the wastewater. The removal percentage of COD and TOC were calculated by using the formulas: % COD = $[(COD_i - COD_f)/COD_f] \times 100\%$; and %TOC = $[(TOC_i - TOC_f)/TOC_f] \times 100\%$, respectively; where COD_i and TOC_i are the initial COD and TOC, while COD_f and TOC_f are the final COD and TOC of raw wastewater. The % TOC and % COD removal data were recorded at 60, 120, 180, and 240 min time intervals (**Figure 7.6b**) by treating the 50 ml of raw wastewater with 0.4 g/L of the catalyst. The total time of degradation was increased for TOC and COD analysis to check the photo-activity of CDZ composite towards the real wastewater. The maximum % COD removal of ~67.8% and % TOC removal of 62.2% was achieved, indicating enhanced mineralization of organic matter present in wastewater.

7.4 RhB dye degradation

RhB dye was also degraded with 1:5 CDZ nanocomposite for comparison of the photocatalytic efficiency of the catalyst. The RhB dye solution (5 ppm) was prepared and its absorbance value was recorded at maximum wavelength, λ_{max} 554 nm.[17,18] The effect of catalyst dose of 1:5 CDZ composite was investigated in the concentration range of 0.1-0.5 g/L (**Figure 7.6c**). The catalyst was taken into a beaker containing a specific volume of the dye solution and stirred for 40 minutes in the dark to bring adsorption in equilibrium, and then degradation activity was analyzed under UV light for another 120 minutes. The maximum degradation efficiency of ~90% was achieved at 0.4 g/L of catalyst dose which indicates that the 1:5 CDZ composite was also applicable for the degradation of RhB industrial dye.[17] The experimental studies were performed in triplicates for accuracy.

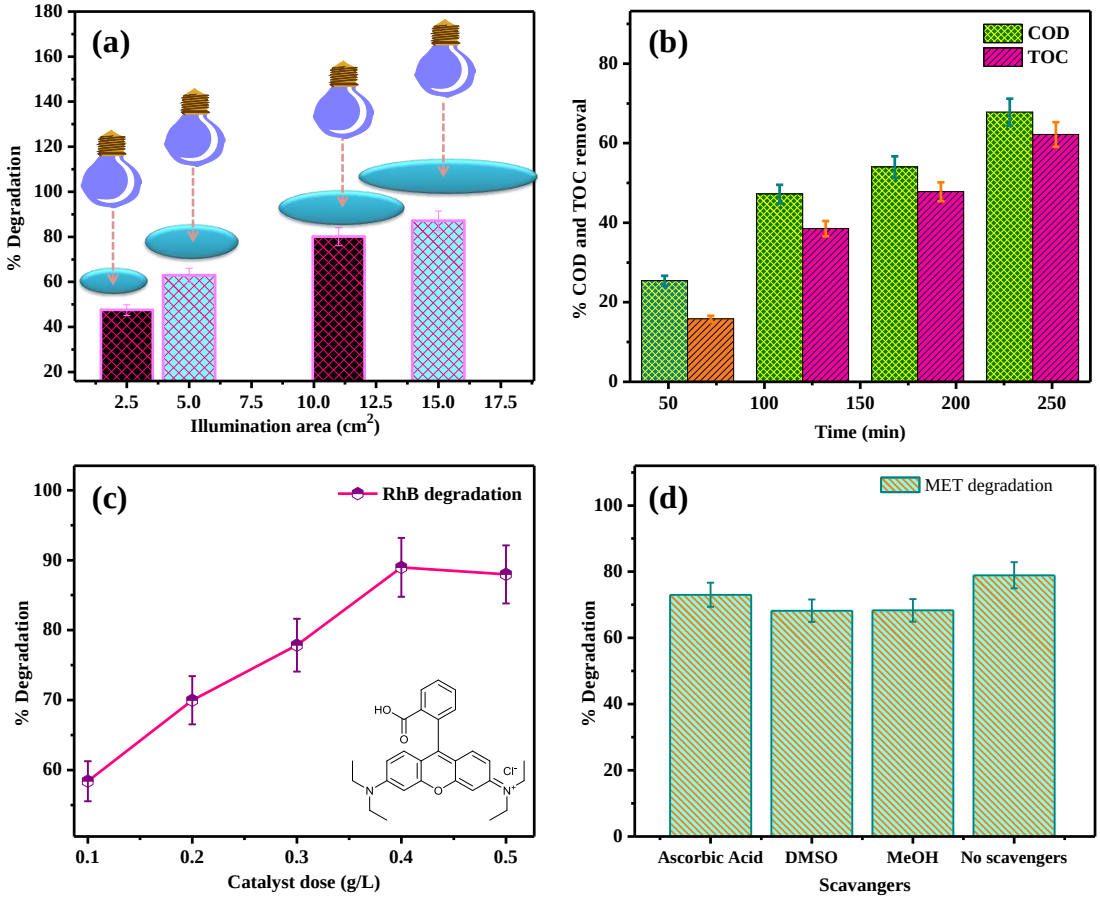

Figure 7.6: (a) Effect of illuminating area, (b) % COD and % TOC removal of raw wastewater, (c) catalyst dose on RhB degradation (inset: RhB structure), and (d) scavengers effect on MET degradation by 1:5 CDZ composite.

7.5 Reusability study

The stability of the CDZ composite has significance for its practical applicability. The regenerability of the composite was investigated for few cycles by simple washing with distilled water and dried at 60 °C temperature. **Figure 7.7a** indicates the data of reusability of 1:5CDZ photocatalyst up to 4 cycles, and a slight decrease in the % degradation (up to 10-15%) was observed. This study reports the higher stability of CDZ materials which is a promising photoactive material with its relevancy for the pollutants elimination from the environment.

To ensure the original properties of the CDZ composite, characterizations like XRD, BET, BJH, and SEM after the photocatalysis treatment were done. The after-treatment XRD spectrum of 1:5 composite possesses the actual peaks with a slight decrease in the intensity, indicating that the crystallinity and planes of the composite were not disturbed even after the photocatalytic reaction and depicted in **Figure 7.7b**. The after-treatment surface area was measured by N_2 adsorption-desorption isotherm which shows the minor decrease in the surface area from 187 to 163 m^2/g and pore volume from 0.244 to 0.229 cm^3/g. The after-treatment BET analysis (**Figure 7.7c**) confirmed that the type-IV isotherm was also maintained. While the presence of micro and macropores in 1:5 CDZ composite after the treatment were analyzed from BJH analysis (**Figure 7.7d**). The surface morphology was also verified from SEM analysis, indicating that the particles remain intact even after the photocatalysis reaction as depicted in **Figure 7.7e,f**. This substantiates that, the CDZ composite is highly regenerable and can be applied to large-scale reactions.

7.6 Photocatalytic degradation mechanism

The role of scavengers has been studied to know the active species responsible for the degradation of MET contaminant and the degradation mechanism was also explored. In scavengers study, the various active compounds, like ascorbic acid (AA), methanol (MeOH), and DMSO have been used to trap superoxide radicals, holes, and hydroxyl radicals,[12,17,19] respectively. **Figure 7.6d** indicates that electrons are the responsible species for the degradation of MET as the % degradation of DMSO obtained is much lesser than that of other scavengers and even no-scavenger.

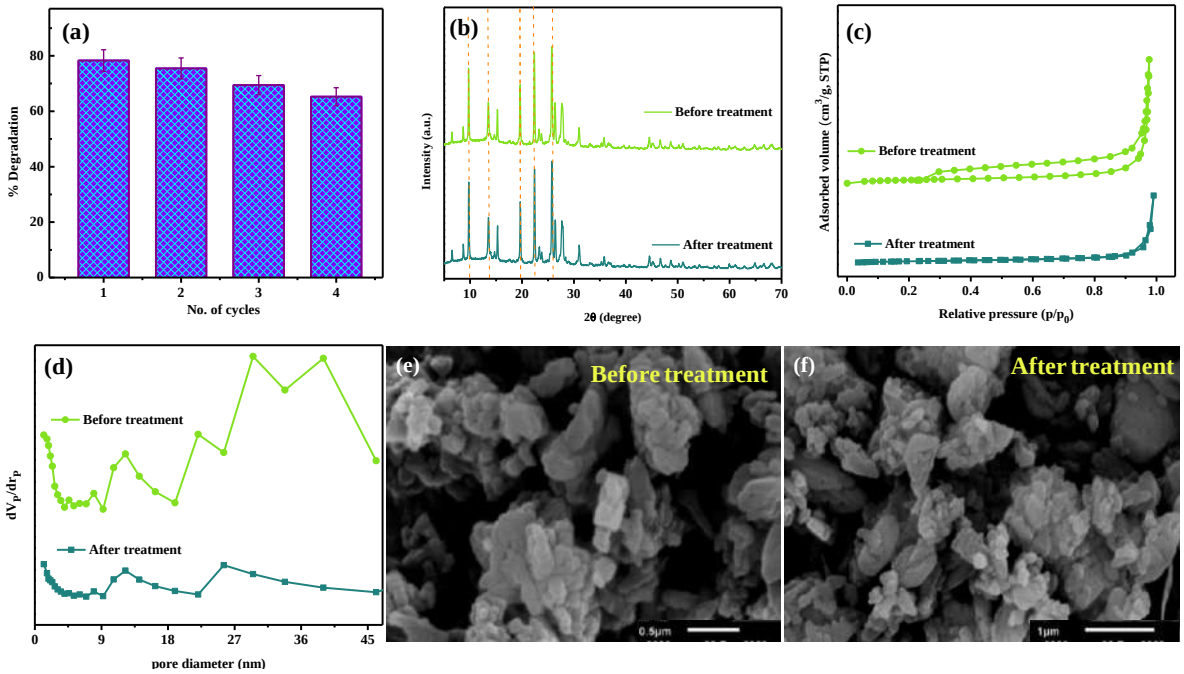

Figure 7.7: (a) Reusability analysis, (b) XRD, (c) BET, (d) BJH, and (e-f) SEM analyses of 1:5 CDZ nanocomposite before and after the photocatalysis treatment.

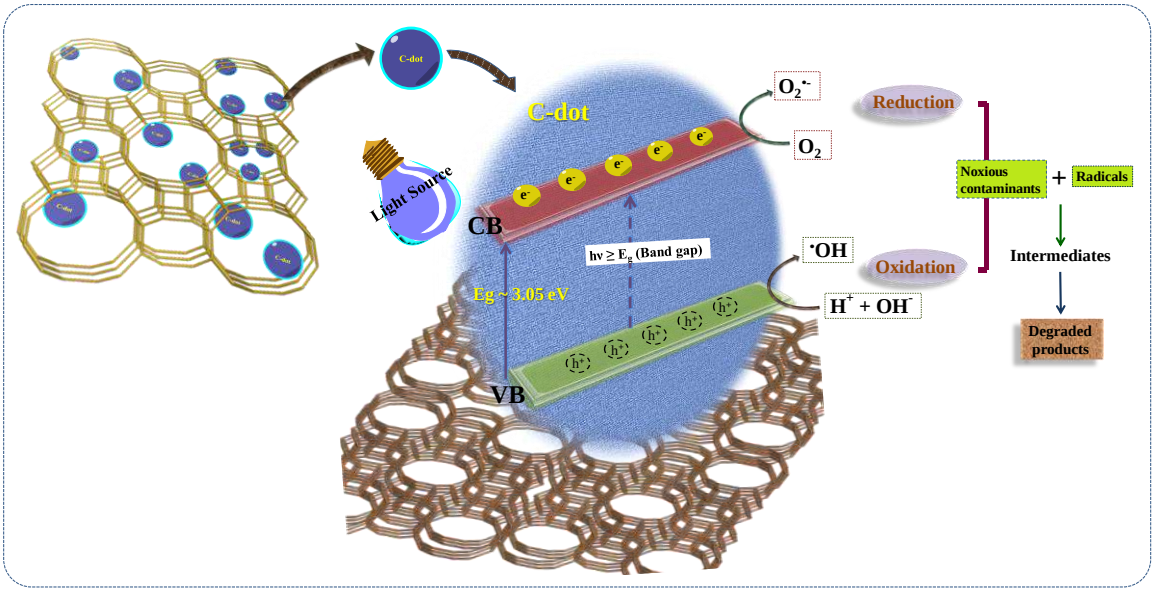

Scheme 7.2: Plausible degradation mechanism by CDZ composites.

The surface of the CDZ composite absorbs light, greater than its band-gap energy value which makes an excitation from VB (valence band) to CB (conduction band). The photo-generated electrons got excited to VB leaving holes (h^+) behind. The generated h^+ reacted with OH^- to form $^{\bullet}OH$ species and e^- reacted with O_2 to form $O_2^{\bullet-}$ radical species.[20] These degradation reactions were written below in **Equation (7.2-7.6):**

$$\text{CDZ composite} \xrightarrow{h\nu} e^-_{(CB)} + h^+_{(VB)} \quad (7.2)$$

$$e^-_{(CB)} + O_2 \xrightarrow{h\nu} O_2^{\bullet-} \quad (7.3)$$

$$h^+_{(VB)} + H_2O \rightarrow H_2O^+ \rightarrow OH^- + H^+ \quad (7.4)$$

$$h^+_{(VB)} + OH^- \rightarrow {}^{\bullet}OH \quad (7.5)$$

$$^{\bullet}OH + O_2^{\bullet-} + MET \rightarrow \text{photo-degraded intermediates or mineralized products} \quad (7.6)$$

The schematic representation of the photodegradation mechanism is displaced in **Scheme 7.2**.

7.7 GC-MS analysis

The degraded intermediate products of MET were analyzed with GC-MS spectrum by m/z ratios. The organic intermediates were extracted by organic solvent methanol, filtered, and then used for the GC-MS analysis. The GC-MS spectrum in **Figure 7.8** was analyzed and the plausible pathway for MET degradation was proposed (**Figure 7.9**) by attacking e^-/h^+ pairs or hydroxyl species in the photodegradation phenomenon.[21–23] The drawn plausible pathway was similar to that of the previous work, suggesting the hydroxyethyl cleavage takes place along with nitro-reduction, de-methylation, and de-nitration steps.[23–25] The MET molecules get converted into 2-methyl-5-nitro-1H-imidazole (m/z = 126.03) by hydroxyethyl cleavage which upon de-nitration forms 2-methyl-1H-imidazole (m/z = 82.05). The 2-methyl-5-nitro-1H-imidazole leads to the formation of 1H-imidazol-5-amine (m/z = 85.05) through nitro-reduction and attacked by $^{\bullet}OH$ radicals to form 2-methyl-1H-imidazole-4,5-dione (m/z = 112.03).

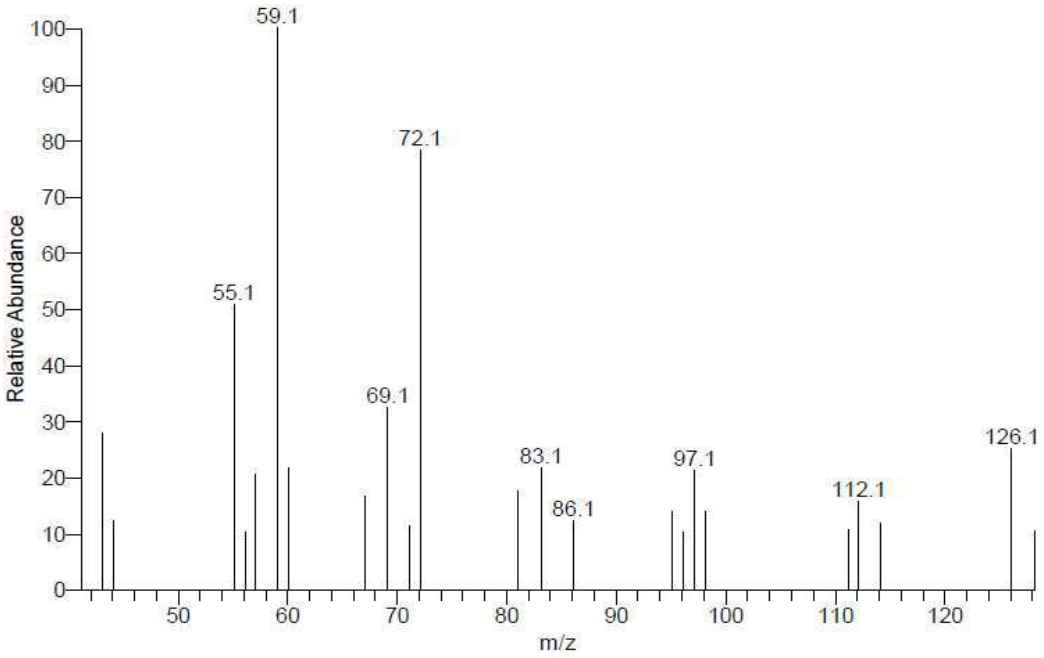

Figure 7.8: GC-MS spectrum of MET having m/z values at retention time 29.98.

The 2-methyl-1H-imidazole-4,5-dione undergoes fragmentation to form N-ethylidene formamide (m/z = 71.04) and is also attacked by •OH radicals to give rise to simpler hydrocarbons after several steps.[7] The 2-methyl-5-nitro-1H-imidazole also undergoes de-methylation and de-nitration to produce 1H-imidazole (m/z = 68.04) and then after several hydroxyl attacks 2-aminoacetonitrile (m/z = 56.02), 2-hydroxyacetonitrile (m/z = 57.02), acetic acid were formed. On the other hand, the MET molecules directly undergo de-nitration to form 2-(2-methyl-1H-imidazol-1-yl)ethan-1-ol (m/z = 126.08) which upon de-methylation forms 2-(1H-imidazol-1-yl)ethan-1-ol (m/z = 112.06). After the ring opening of 2-(1H-imidazol-1-yl)ethan-1-ol, few intermediates like, 1-ethyl-1H-imidazole (m/z = 96.07), acetamide (m/z = 59.04) were formed and mineralized to simpler hydrocarbons. The several intermediate products can undergo an oxidation process by hydroxyl attack, give rise to carboxylic acids that are ultimately mineralized into simpler hydrocarbons, CO_2, NO_2, NH_3, and water.[26–29] These formed intermediates were in agreement with reported literature. The intermediates formed at a retention time (RT) of 29.98 were analyzed by m/z values (**Figure 7.8**) and drawn in the form of a scheme shown in **Figure 7.9**.

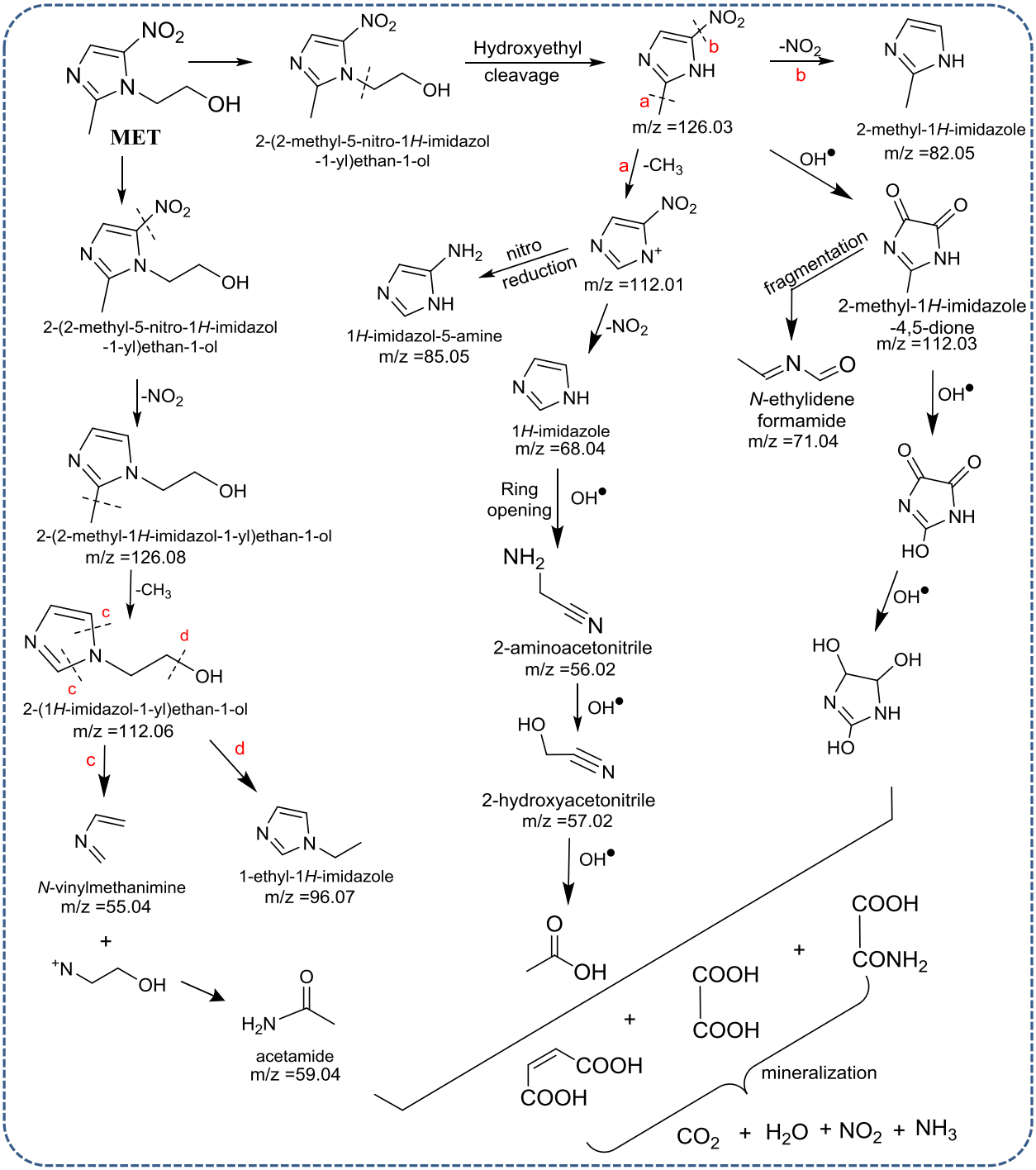

Figure 7.9: The degradation pathway of MET by 1:5 CDZ nanocomposite.

The degraded intermediate products of RhB dye were analyzed with GC-MS spectrum by m/z ratios. The organic intermediates were extracted by organic solvent methanol, after filteration it was used for the GC-MS analysis. The GC-MS spectrum of RhB was analyzed and degraded intermediate products of RhB dye were identified and tabularized in Table 7.3 with product name, retention time, formula and m/z values.[30–32]

Table 7.3: Various degraded products formed in GC-MS analysis of RhB dye.

S. No.	Degraded Product name	Retention time	Formula	m/z value
1.	Pyrazine, methyl-	27.89	$C_5H_6N_2$	95 [M+1]
2.	Tromethamin	8.74	$C_4H_{11}NO_3$	121.1 [M]
3.	Oleanitrile	32.54	$C_{18}H_{33}N$	263 [M+1]
4.	9-Octadecenamide, (Z)-	28.47	$C_{18}H_{35}NO$	281 [M]
5.	Phthalic acid	28.47	$C_8H_6O_4$	166 [M]
6.	2-vinylbenzoic acid	4.38	$C_9H_8O_2$	148 [M+1]
7.	hydroquinone	28.47	$C_6H_6O_2$	111 [M+1]

7.9 Conclusions

The C-dots were successfully fabricated on the zeolite framework via a hydrothermal method and were exploited for recalcitrant MET and RhB degradation. The facile method of fabricated CDZ composite provides the formation of 5 CDZ composites of different ratios (1:1, 1:3, 1:5, 5:1, 1:7) with fascinating photo-activity and sufficient surface area for adsorption and photodegradation of noxious contaminants. The 1:5 CDZ composite gave maximum photodegradation efficiency due to its high surface area, pore-volume, low recombination rate, and suitable bandgap energy value. The pH results were well justified with the PZC point which was determined by the salt addition method. The rate constants or % degradation data of MET under different light sources conclude that the maximum elimination was achieved in UV light. The scavenger study reveals that the hydroxyl radicals were majorly responsible for the photodegradation of pollutants. The GC-MS analysis was done for the identification of the intermediates and the scheme for a plausible degradation pathway was drawn. This work gives a new route to synthesize an efficient zeolite-based photoactive composite for MET elimination from wastewater effluent and can be very beneficial to eradicate the pharmaceuticals from water bodies.

References

(1) Yang, D.; Qu, D.; An, L.; Zong, X.; Sun, Z. A Metal-Free Carbon Dots for Wastewater

Treatment by Visible Light Active Photo-Fenton-like Reaction in the Broad PH Range. *Chinese Chem. Lett.* **2021**. https://doi.org/10.1016/j.cclet.2021.02.005.

(2) Rathi, A.; Basu, S.; Barman, S. Structural Framework Effect of Various CeO_2-Loaded Zeolites on the Adsorptive Removal of Fipronil. *J. Environ. Chem. Eng.* **2021**, *9* (2), 105167. https://doi.org/10.1016/j.jece.2021.105167.

(3) Liu, J.; Zhang, H.; Wang, N.; Yu, Y.; Cui, Y.; Li, J.; Yu, J. Template-Modulated Afterglow of Carbon Dots in Zeolites: Room-Temperature Phosphorescence and Thermally Activated Delayed Fluorescence. *ACS Mater. Lett.* **2019**, *1* (1), 58–63. https://doi.org/10.1021/acsmaterialslett.9b00073.

(4) Liu, J.; Wang, N.; Yu, Y.; Yan, Y.; Zhang, H.; Li, J.; Yu, J. Carbon Dots in Zeolites: A New Class of Thermally Activated Delayed Fluorescence Materials with Ultralong Lifetimes. *Sci. Adv.* **2017**, *3* (5), e1603171. https://doi.org/10.1126/sciadv.1603171.

(5) Nocuń, M.; Kwaśny, S. Preparation and Characterization of V_2O_5 Doped SiO_2-TiO_2 Thin Films. *Cent. Eur. J. Eng.* **2012**, *2*, 123–128. https://doi.org/10.2478/s13531-011-0041-6.

(6) Fang, R.-C.; Sun, Q.-Q.; Zhou, P.; Yang, W.; Wang, P.-F.; Zhang, D. W. High-Performance Bilayer Flexible Resistive Random Access Memory Based on Low-Temperature Thermal Atomic Layer Deposition. *Nanoscale Res. Lett.* **2013**, *8* (1), 92. https://doi.org/10.1186/1556-276x-8-92.

(7) Sharma, S.; Basu, S. Visible-Light-Driven Efficient Photocatalytic Abatement of Recalcitrant Pollutants by Centimeter-Length MoO_3/SiO_2 Monoliths with Long Service Life. *Appl. Mater. Today* **2021**, *23*, 101033. https://doi.org/10.1016/j.apmt.2021.101033.

(8) Kundu, A.; Sharma, S.; Basu, S. Modulated BiOCl Nanoplates with Porous g-C_3N_4 Nanosheets for Photocatalytic Degradation of Color/Colorless Pollutants in Natural Sunlight. *J. Phys. Chem. Solids* **2021**, *154*, 110064. https://doi.org/10.1016/j.jpcs.2021.110064.

(9) Monga, D.; Basu, S. Tuning the Photocatalytic/Electrocatalytic Properties of MoS_2 /$MoSe_2$ Heterostructures by Varying the Weight Ratios for Enhanced Wastewater Treatment and Hydrogen Production . *RSC Adv.* **2021**, *11* (37), 22585–22597. https://doi.org/10.1039/d1ra01760h.

(10) You-ji, L.; Wei, C. Photocatalytic Degradation of Rhodamine B Using Nanocrystalline TiO_2–Zeolite Surface Composite Catalysts: Effects of Photocatalytic Condition on Degradation Efficiency. *Catal. Sci. Technol.* **2011**, *1* (5), 802. https://doi.org/10.1039/c1cy00012h.

(11) Nasseh, N.; Arghavan, F. S.; Rodriguez-Couto, S.; Hossein Panahi, A.; Esmati, M.; A-Musawi, T. J. Preparation of Activated Carbon@ZnO Composite and Its Application as a Novel Catalyst in Catalytic Ozonation Process for Metronidazole Degradation. *Adv. Powder Technol.* **2020**, *31* (2), 875–885. https://doi.org/10.1016/j.apt.2019.12.006.

(12) Monga, D.; Ilager, D.; Shetti, N. P.; Basu, S.; Aminabhavi, T. M. 2D/2d Heterojunction of

MoS_2/g-C_3N_4 Nanoflowers for Enhanced Visible-Light-Driven Photocatalytic and Electrochemical Degradation of Organic Pollutants. *J. Environ. Manage.* **2020**, *274*, 111208. https://doi.org/10.1016/j.jenvman.2020.111208.

(13) Bakatula, E. N.; Richard, D.; Neculita, C. M.; Zagury, G. J. Determination of Point of Zero Charge of Natural Organic Materials. *Environ. Sci. Pollut. Res.* **2018**, *25* (8), 7823–7833. https://doi.org/10.1007/s11356-017-1115-7.

(14) Nasseh, N.; Arghavan, F. S.; Rodriguez-Couto, S.; Hossein Panahi, A.; Esmati, M.; A-Musawi, T. J. Preparation of Activated Carbon@ZnO Composite and Its Application as a Novel Catalyst in Catalytic Ozonation Process for Metronidazole Degradation. *Adv. Powder Technol.* **2020**, *31* (2), 875–885. https://doi.org/10.1016/j.apt.2019.12.006.

(15) Sharma, S.; Basu, S. Highly Reusable Visible Light Active Hierarchical Porous WO_3/SiO_2 Monolith in Centimeter Length Scale for Enhanced Photocatalytic Degradation of Toxic Pollutants. *Sep. Purif. Technol.* **2020**, *231*, 115916. https://doi.org/10.1016/j.seppur.2019.115916.

(16) Aanchal; Barman, S.; Basu, S. Complete Removal of Endocrine Disrupting Compound and Toxic Dye by Visible Light Active Porous g-C_3N_4/H-ZSM-5 Nanocomposite. *Chemosphere* **2020**, *241*, 124981. https://doi.org/10.1016/j.chemosphere.2019.124981.

(17) Monga, D.; Basu, S. Enhanced Photocatalytic Degradation of Industrial Dye by g-C_3N_4/TiO_2 Nanocomposite: Role of Shape of TiO2. *Adv. Powder Technol.* **2019**, *30* (5), 1089–1098. https://doi.org/10.1016/j.apt.2019.03.004.

(18) Wang, Y.; Liu, X.; Guo, L.; Shang, L.; Ge, S.; Song, G.; Naik, N.; Shao, Q.; Lin, J.; Guo, Z. Metal Organic Framework-Derived C-Doped ZnO/TiO_2 Nanocomposite Catalysts for Enhanced Photodegradation of Rhodamine B. *J. Colloid Interface Sci.* **2021**, *599*, 566–576. https://doi.org/10.1016/j.jcis.2021.03.167.

(19) Rosenblum, W. I.; El-Sabban, F. Dimethyl Sulfoxide (Dmso) and Glycerol, Hydroxyl Radical Scavengers, Impair Platelet Aggregation within and Eliminate the Accompanying Vasodilation of, Injured Mouse Pial Arterioles. *Stroke* **1982**, *13* (1), 35–39. https://doi.org/10.1161/01.STR.13.1.35.

(20) Nagar, A.; Basu, S. Ternary g-C_3N_4/Ag/$BiVO_4$ Nanocomposite: Fabrication and Implementation to Remove Organic Pollutants . *Environ. Technol. Innov.* **2021**, *23*, 101646. https://doi.org/10.1016/j.eti.2021.101646.

(21) Xia, Y.; Zhang, Q.; Li, G.; Tu, X.; Zhou, Y.; Hu, X. Biodegradability Enhancement of Real Antibiotic Metronidazole Wastewater by a Modified Electrochemical Fenton. *J. Taiwan Inst. Chem. Eng.* **2019**, *96*, 256–263. https://doi.org/10.1016/j.jtice.2018.11.019.

(22) Martins, P. M.; Salazar, H.; Aoudjit, L.; Gonçalves, R.; Zioui, D.; Fidalgo-Marijuan, A.; Costa, C. M.; Ferdov, S.; Lanceros-Mendez, S. Crystal Morphology Control of Synthetic Giniite for Enhanced Photo-Fenton Activity against the Emerging Pollutant Metronidazole. *Chemosphere* **2021**, *262*, 128300. https://doi.org/10.1016/j.chemosphere.2020.128300.

(23) Dai, Q.; Zhou, J.; Weng, M.; Luo, X.; Feng, D.; Chen, J. Electrochemical Oxidation Metronidazole with Co Modified PbO_2 Electrode: Degradation and Mechanism. *Sep. Purif. Technol.* **2016**, *166*, 109–116. https://doi.org/10.1016/j.seppur.2016.04.028.

(24) Xu, L.; Yang, Y.; Li, W.; Tao, Y.; Sui, Z.; Song, S.; Yang, J. Three-Dimensional Macroporous Graphene-Wrapped Zero-Valent Copper Nanoparticles as Efficient Micro-Electrolysis-Promoted Fenton-like Catalysts for Metronidazole Removal. *Sci. Total Environ.* **2019**, *658*, 219–233. https://doi.org/10.1016/j.scitotenv.2018.12.040.

(25) El Bouraie, M. M.; Ibrahim, S. S. Comparative Study Between Metronidazole Residues Disposal by Using Adsorption and Photodegradation Processes onto MgO Nanoparticles. *J. Inorg. Organomet. Polym. Mater.* **2021**, *31* (1), 344–364. https://doi.org/10.1007/s10904-020-01711-6.

(26) Chiarinelli, J.; Casavola, A. R.; Castrovilli, M. C.; Bolognesi, P.; Cartoni, A.; Wang, F.; Richter, R.; Catone, D.; Tosic, S.; Marinkovic, B. P.; Avaldi, L. Radiation Damage Mechanisms of Chemotherapeutically Active Nitroimidazole Derived Compounds. *Front. Chem.* **2019**, *7* (MAY). https://doi.org/10.3389/fchem.2019.00329.

(27) Pan, Y.; Li, X.; Fu, K.; Deng, H.; Shi, J. Degradation of Metronidazole by UV/Chlorine Treatment: Efficiency, Mechanism, Pathways and DBPs Formation. *Chemosphere* **2019**, *224*, 228–236. https://doi.org/10.1016/j.chemosphere.2019.02.081.

(28) Asgharzadeh, F.; Gholami, M.; Jafari, A. J.; Kermani, M.; Asgharnia, H.; Kalantary, R. R. Heterogeneous Photocatalytic Degradation of Metronidazole from Aqueous Solutions Using Fe_3O_4/TiO_2 Supported on Biochar. *Desalin. Water Treat.* **2020**, *175*, 304–315. https://doi.org/10.5004/dwt.2020.24789.

(29) Ammar, H. B.; Brahim, M. Ben; Abdelhédi, R.; Samet, Y. Green Electrochemical Process for Metronidazole Degradation at BDD Anode in Aqueous Solutions via Direct and Indirect Oxidation. *Sep. Purif. Technol.* **2016**, *157*, 9–16. https://doi.org/10.1016/j.seppur.2015.11.027.

(30) Baldev, E.; MubarakAli, D.; Ilavarasi, A.; Pandiaraj, D.; Ishack, K. A. S. S.; Thajuddin, N. Degradation of Synthetic Dye, Rhodamine B to Environmentally Non-Toxic Products Using Microalgae. *Colloids Surfaces B Biointerfaces* **2013**, *105*, 207–214. https://doi.org/10.1016/j.colsurfb.2013.01.008.

(31) Sharma, G.; Dionysiou, D. D.; Sharma, S.; Kumar, A.; Al-Muhtaseb, A. H.; Naushad, M.; Stadler, F. J. Highly Efficient Sr/Ce/Activated Carbon Bimetallic Nanocomposite for Photoinduced Degradation of Rhodamine B. *Catal. Today* **2019**, *335*, 437–451. https://doi.org/10.1016/j.cattod.2019.03.063.

(32) Liu, Y.; Guo, H.; Zhang, Y.; Cheng, X.; Zhou, P.; Zhang, G.; Wang, J.; Tang, P.; Ke, T.; Li, W. Heterogeneous Activation of Persulfate for Rhodamine B Degradation with 3D Flower Sphere-like $BiOI/Fe_3O_4$ Microspheres under Visible Light Irradiation. *Sep. Purif. Technol.* **2018**, *192*, 88–98. https://doi.org/10.1016/j.seppur.2017.09.045.

Chapter 8: Conclusions and future perspective

8.1 Introduction

In the present investigation, research was carried out for the preparation, modification, and characterization of zeolite adsorbent for removal of Fipronil pesticide from its aqueous solutions and photocatalytic degradation of MET and RhB from its aqueous solution.

8.2 Conclusions from research work

In **Chapter 4**, the H-ZSM-5 zeolite was modified with cerium salt of different concentrations ranging from 5-30% (w/v%). by a simple ion-exchange method for the removal of FIP pesticide from the aqueous solution. The H-ZSM-5 was treated with 25% cerium nitrate solution (Ce_{25}ZSM-5) and was found to remove a maximum of 90% Fipronil from its aqueous solution. The various parameters such as time, pH, adsorbent dose, pesticide concentration, temperature, and stirring speed were optimized by carrying out batch adsorption experiments. The XRD spectrum indicates the planes of cerium oxide that match with JCPDS No. 34-0394, while the HR-TEM images indicate the presence of cerium oxide particles over the zeolite structure. The BET analysis indicates a surface area 192 m^2/g for Ce_{25}ZSM-5 adsorbent. The super adsorptive performance of the Ce_{25}ZSM-5 is due to ionic interactions between the adsorbate and adsorbent. The Langmuir adsorption isotherm and pseudo-second-order model were best fitted with adsorption data, indicating monolayer adsorption and fast adsorption rate. The thermodynamic studies reveal that the adsorption process was spontaneous and exothermic.

In **Chapter 5**, the g-C_3N_4/H-ZSM-5 composite was successfully synthesized by facile calcination and used for the photocatalytic degradation of MB and FIP. The g-C_3N_4/H-ZSM-5 composite was characterized by XRD, BET, HRTEM, FESEM, EDS, and XPS analysis to determine the structural and morphological properties. The surface analysis concludes that the surface of the composite is highly porous, rough with a surface area of 172 m^2/g. The amount% calculated was 71.10% and 28.29% for species Ce(IV) and Ce(III) respectively. The bandgap of the composite was calculated by Tauc's plot which lies in the visible range of the solar spectrum. The surface area of the composite is greater than the pure pristine g-C_3N_4 which leads to better degradation of the pollutants. Under visible light and sunlight irradiation, the photodegradation of

MB and FIP by g-C_3N_4/H-ZSM-5 composite was greater than that of g-C_3N_4 alone. The degradation mechanism was proposed and discussed in detail with the role of radicals.

In **Chapter 6**, ammonium forms of different zeolites (H-BETA, H-MOR, H-13X) were modified with cerium by the ion-exchange method to eliminate FIP pesticides from an aqueous solution. The cerium-modified zeolites have shown much higher adsorption capacities than ammonium-form zeolites. The comparative studies were carried out among all three Ce modified adsorbents. Ce-BETA zeolite was found to be the best (~94% removal) for adsorption of FIP because of its high active sites, high surface area, and high Si/Al ratio which leads to high adsorptive performances. Ce-MOR also has ~90% removal of FIP due to its high Si/Al ratio that promotes more metal loading which finally facilitates the adsorption process. Langmuir isotherm and pseudo-second-order model signifying monolayer adsorption with a faster adsorption rate. The negative ΔG° value confirms that the FIP adsorption was spontaneous and exothermic. The high adsorption that occurred may be due to electrostatic or chemical interaction. Moreover, the comparison studies of modified and unmodified zeolites were done which proves the need for modification of adsorbents for better FIP removal. The inactive cations of zeolites have been exchanged with cerium to increase the interaction of the noxious contaminants for making the surface more active for adsorptive removal. The zeolites with high Si/Al ratios provide stability in the acidic medium and also in the water medium. These features lead the zeolite to wider applicability on a large scale.

In **Chapter 7**, the C-dots and zeolite composites were synthesized via a hydrothermal method and were exploited for recalcitrant MET and RhB degradation. CDZ composites of different ratios (1:1, 1:3, 1:5, 5:1, 1:7) were fabricated by facile method for enhanced photo-activity. The 1:5 CDZ composite contributed to maximum photodegradation due to its high surface area, pore-volume, low recombination rate, and suitable bandgap energy value. The pH values were well justified with the PZC point which was determined by the salt addition method. The rate constants or % degradation data of MET under different light sources conclude that the maximum elimination was achieved in UV light. The scavenger study was done to reveal the plausible degradation mechanism. The GC-MS analysis for the identification of the intermediates was carried out and the scheme for a plausible degradation pathway was drawn. This work may lead to a new route for the synthesis of an efficient zeolite-based photoactive composite for MET

elimination from wastewater effluent and can be very beneficial to eradicate the toxic pharmaceuticals from water bodies.

Direct implementation of only photoactive materials like g-C_3N_4 and C-dots doesn't provide the efficient removal of insecticide (FIP) and recalcitrant contaminant (metronidazole) due to their less surface area and high recombination rate. Therefore, a support material like zeolite has been utilized which provides better degradation efficiencies of these photoactive materials. The zeolite provides a high surface area for the adsorption of pollutants and also helps in reducing the recombination rate of the photocatalysts.

Table 8.1: Major findings on removal of pollutants by zeolite based materials.

Pollutants	Adsorbent/photocatalysts	% Removal
FIP	Ce_{25}ZSM-5	91.8
FIP	Ce-13X	86.21
FIP	Ce-MOR	89.44
FIP	Ce-BETA	93.54
FIP	g-C_3N_4/H-ZSM-5 composite	84.01
MB	g-C_3N_4/H-ZSM-5 composite	92.0
MET	1:5 CDZ composite	78.9
RhB	1:5 CDZ composite	90.0

In summary, the current research work is a comprehensive study of extending the zeolite applications by fabrication of metal oxides or carbon-based photoactive materials by ion-exchange and facile calcination techniques respectively, and performance evaluation under different conditions along with kinetics, isotherm, and thermodynamics analysis.

8.3 Future perspective

- Pilot-scale experiments using cerium modified zeolite as the adsorbent can be carried out for the removal of FIP from wastewater.
- CDZ composite can be applied to the industry for large-scale MET and RhB degradation from wastewater.

- The adsorptive activity and photocatalytic performance of metal-modified zeolites (e.g CeO_2) can be tested at high temperature and pressure conditions.
- Cerium-modified zeolite with a high surface area can be applied for gaseous adsorption processes on large scale.
- The CeO_2-zeolites modified to heterostructures can be explored for their chemical and biological applications like antiviral, antifungal, or photocatalysis.
- Zeolite frameworks can be fabricated with different C-dots for applications of sensing pesticides, metal ions, etc.